PHENOMOLOGY STUDY OF THE LINEAR CHIRP DERIVED HIGH-RANGE RESOLUTION SIGNATURE

Thesis

Submitted to

The School of Engineering

UNIVERSITY OF DAYTON

In Partial Fulfillment of the Requirements for

The Degree

Master of Science in Electrical Engineering

By

James Paul Browning

UNIVERSITY OF DAYTON

Dayton, Ohio

December, 2007

PHENOMOLOGY STUDY OF THE LINEAR CHIRP DERIVED HIGH-RANGE RESOLUTION SIGNATURE

APPROVED BY:

Krishna Pasala, Ph.D.
Advisory Committee Chairman
Professor, Electrical and Computer Engineering Department

Guru Subramanyam, Ph.D.
Committee Member
Associate Professor, Electrical and Computer Engineering Department

John Malas, Ph.D.
Committee Member
Senior Scientist, Air Force Research Laboratory

Malcolm W. Daniels, Ph.D.
Associate Dean, School of Engineering

Joseph E. Saliba, Ph.D., P.E.
Dean, School of Engineering

ABSTRACT

INTERFERENCE PHENOMOLOGY UTILIZING THE LINEAR CHIRP DERIVED HIGH-RANGE RESOLUTION SIGNATURE

Name: Browning, James Paul
University of Dayton

Advisor: Krishna Pasala, Ph.D.

An investigation into the LFM derived HRR signature of an idealized planar target structure is undertaken with respect to target discretes exhibiting angular and frequency selective reflectivity profiles. Results are most noticeable for the objective signal subspace investigation. A subjective study is undertaken to visually show what effects point target angular and frequency selectivity have on the LFM derived HRR signature. The conclusions of the phenomenology study give meaning to the LFM derived HRR signature in regards to the salient feature sets and the HRR signature interference phenomena.

ACKNOWLEDGEMENTS

I wish to thank my graduate advisor, Dr. Krishna Pasala, for giving me the opportunity to pursue this research interest. His patient guidance, insightful discussions, and countless research reviews have been instrumental in my successful completion of this work. Through our many meetings and talks, the subject of this thesis has become both clear and germane. I have been most fortunate, indeed, to be able to work with an advisor possessing both the depth and breadth of knowledge that this particular subject area demands.

I wish to thank the members of my thesis committee for taking time to mentor me throughout my graduate career. Dr. Guru Subramanyam and Dr. John Malas have been instrumental in my graduate and professional development.

I also thank the Air Force Research Laboratory for sponsoring this thesis and my graduate coursework through a contract with the University of Dayton Department of Electrical and Computer Engineering.

Finally, I thank Hilary Ross for her love, encouragement, and unwavering patience as I pursued this research. This thesis is dedicated to my parents, who have always been there to support and encourage me in my many endeavors.

TABLE OF CONTENTS

LIST OF FIGURES

CHAPTER 1

INTRODUCTION, MOTIVATION AND OVERVIEW

Section 1.1-Introduction

This work will detail the development of the linear-frequency modulated (LFM) high-range resolution (HRR) profile through the framework of radar imaging theory. Central to the understanding of the HRR signature is the creation of the HRR profile, the fundamental element comprising a given target signature. Following transmission of a waveform by the airborne radar sensor platform, the signal impacts a given target structure-usually the size of the target is much greater than the wavelength of the transmitted waveform-and is modulated by the reflectivity of the target structure. The modulated waveform is captured by the radar sensor and processed to determine the information about the target. The output of the matched filter is the HRR profile and is a collection of samples representing reflectivity of the given target structure as a function of down range The reflectivity is highly dependent upon the scattering mechanisms that are inherent within the extended target structure. The HRR signature process is formed by the collection of a series of HRR profiles corresponding to various look angles about a nominal target angle. A collection of look angles

forms the look window for a given scenario. Hence, the HRR signature process is a collection of one-dimensional images comprised of individual HRR profile images corresponding to a given look angle within the look.

The underlying physical process and how they affect the "features" of the HRR signature are the subject matter of this work. To this end, the investigation will focus on scattering phenomenology and signal processing schema that, coupled with scattering mechanisms, are responsible for salient feature sets viewable within the HRR signature.

1.2-Motivation

Examples of salient feature sets are unique identifying peaks within the HRR signature that are persistent over a range of viewing angles. In conjunction with the HRR sensor and associated signal processing subsystems, there are a multitude of steps from transmit to receive that alter the information content of the target range space. This is most evident when viewed from a dimensionality standpoint; the HRR profile is a one-dimensional representation of a three-dimensional target. The dimensionality reduction compresses a great deal of information into, essentially, a plot of the signal returns. Associated with the dimensionality reduction, are a range of effects critical to the understanding of the HRR profile creation; of these effects, the topic of interference is paramount. Interference will be discussed in detail as a consequence of both the target reflectivity profile and signal processing operations.

Section 1.3-History HRR ATR

Interest in using the HRR signature for purposes of automatic-target recognition (ATR) has gained interest as a means for, or basis of, a machine classification of illuminated targets. ATR can be achieved through either active sensing, as in the case of this work, or passive sensing, where the target emits electromagnetic radiation pursuant with detection. The HRR signature is not without disadvantages for use in ATR algorithms. A small sample of the available HRR-ATR literature is briefly reviewed to introduce these challenges for the benefit of problem saliency.

Cheung, et al. [5] introduces a new methodology for target identification based on using radar range profiles and the generalized maximum likelihood ratio test. This approach accommodates the intra-bin dependence of interference due to the high sampling-rates of modern radar and maximizes the probability of target identification. This identification is at the prespecified Type I error, in dependent complex Gaussian processes. All system parameters are estimated with no *a priori* knowledge information necessary about the statistical properties of the measured data. The performance of this approach is dependent upon quality of the training data, and achieves low probability of identification for certain cases of poor or small training data sets.

Ulug, et. Al [22] propose an approach to HRR ATR database creation based on target-signature ontology. This approach is an investigative initial effort

into the creation of a notional database using compression o target-signatures. A case considered is that of HRR signature compression based upon reduction of the number of signatures, or reduction of special dimensionality through feature extraction. Features correspond to target scattering mechanisms that are viewable over a range of look angles for a given target pose angle, hence persistent features. Feature extraction seeks to map these HRR signature magnitude peaks for use in ATR algorithms, such as template matching. For ATR database creation through compression, these features become a codeword in the ontology, which is then used as a basis for ATR algorithms. Fundamental issues discussed are scenario variations: ATR system required to perform regardless of target or platform orientation, line-of-sight distances, weather effects, obstruction by terrain, etc.; ATR systems must perform in environments containing a multitude of target and target types; and modern radar systems have the ability to create high-dimensional data with results in larger target-signatures, increasing computational overhead.

Williams, et. al. [24] discuss the use of HRR template-based ATR algorithm for use in modern radar systems to compliment existing radar modes of MTI/SAR. This template-based ATR algorithm would rely on HRR profiles over a given number of look angles for target identification. Additionally, this is expected to outperform traditional SAR-ATR since moving targets are oft blurred in SAR imagery. A challenge considered in the conclusion of this paper is the rapid decorrelation of HRR signatures as a function of angle, though this was

expected. This decorrelation demonstrates the importance of target-to-clutter ratios on classification performance. One suggestion to increase the effectiveness of the HRR-ATR algorithm is to focus on radar clutter mitigation when considering this approach for moving targets.

Jacobs [9,10] approach the decorrelation issue of the HRR signature through the use of a likelihood-based framework and a sequence of HRR profiles. Thus, given a series of range-profiles, this approach jointly estimates the target type and the sequence of target orientations at the observation times. Candidate deterministic and stochastic models were developed, and the resulting likelihood functions were compared using synthetic data. The recognition performance under this framework is highly dependent upon choosing the appropriate model for the range-profile data. Initial work focused on evaluation of the proposed technique under the deterministic and stochastic development models when target orientation is not known *a priori*. Later work focused on target orientation estimation to increase the performance of target recognition using sequence of HRR profiles.

Mitchell [14] introduces the primary difficulty with HRR-ATR by analyzing the underlying principles of the range-profile creation; namely that the HRR profile is a one-dimensional representation of a three-dimensional target structure formed by the summation of complex exponentials whose phases add constructively and destructively in a given range bin resulting in, potentially, large variations in the HRR profile peaks over a look window. This leads to the

statistical feature based identification using HRR-ATR, where the features are not extracted prior to ATR, but are rather treated as a statistical patter recognition problem. Instead of using a traditional feature vector, which relies on the assumption only the range bin amplitude is a salient feature, the feature vector is treated as a random component. The statistical feature based ATR schema chooses features on dynamically and assumes them to be random variables. Additionally, the feature locations are random variables and the feature amplitudes are treated as conditional random variables, with uncertainty being incorporated into the decision process. The remainder of the paper discusses methods in which this information is used for target-signature identification.

Evident from the sample of available HRR-ATR literature, the range-profile of a target structure is known to exhibit decorrelation when viewed over a range of look angles. Different methodologies were formulated to use the collected range-amplitude data for target identification. While the formation of the HRR profile is understood, the existence of features and physical processes that give rise to processes within the range-profile is the subject of this work. Through the first-principles approach, the signal model used for the HRR profile formation is introduced and analyzed. Specifically, the use of the linear-frequency modulated, or chirp, waveform serves as the signal model for investigation of the HRR phenomenology problem.

Section 1.4-Thesis Outline

Key structural elements of this thesis are detailed presently. Chapter 2 introduces theoretical concepts necessary for the fundamental understanding of the HRR profile through the concepts-based imaging theory framework. The derivation of the LFM waveform from transmit-to-impact-to-receive is presented. Chapter 2 concludes with the HRR algorithm derivation and verification utilizing simple point targets to demonstrate theory. Chapter 3 covers the topic of interference phenomena in the context of the point-spread function and the phenomenology study testing methodology. Chapter 4 begins with a discussion of the target signature, followed by verification utilizing the Russian BMP-2 tank model and the X-Patch derived BMP-2 target signature. Following verification, the notion of range bin statistics is derived and the use of the Kolmogorov-Smirnov goodness-of-fit test to validate the range bin statistics is presented. Next, the idealized planar target model utilized for the remainder of the phenomenology study is shown, along with the corresponding HRR signature. Phenomenology studies of targets exhibiting uniform, angular and frequency selectivity are then discussed and investigated in depth. The framework of this testing regime focuses on subjective and objective methodologies in order to elucidate characteristics of the HRR signature known as salient feature sets. Finally, chapter 5 summarizes the findings of the phenomenology study and expounds upon the results of chapter 4.

Section 1.5-Summary Remarks

In this chapter, the concept of high-range resolution (HRR) formed by range space illumination of a LFM waveform was introduced. The motivation and saliency of the HRR interference phenomenology study was discussed. Finally, an outline of the thesis detailed the remainder of the theory and testing methodology that is covered in subsequent chapters.

CHAPTER 2

INTRODUCTION TO ESSENTIAL BACKGROUND THEORY

Section 2.1-Introduction

The HRR signature is generated by the radar signal processing subsystem and creates an image of the reflectivity profile of the target. This is accomplished through careful selection of an illuminating waveform given some *a priori* knowledge of the target structure of interest. Of note, the HRR profile is a one-dimensional representation of a three-dimensional reflectivity profile. This dimensional collapse is achieved through the projection of the three-dimensional reflectivity profile along the one-dimensional range domain. The range reflectivity profile is represented by one of two equations: either discrete or continuous, in which the corresponding representation is f[n] or f(x), respectively. The reflectivity profile for continuous and discrete cases can be expressed as,

$$f(x) = \sum_{x_c - x_0}^{x_c + x_0} f(x)\delta(x-\xi)d\xi, \quad (x_c - x_0) \le \xi \le (x_c + x_0) \tag{2.1}$$

where the subscripts of the variable *x* denote range swath center, *c*, and range swath extent, *0*. In order to better understand the HRR profile, the reflectivity profile for a single impulse of the n^{th} target scatterer may be said to characterize the image function capabilities of the radar system,

$$f(x)=\delta(x-x_n).\quad (x_c-x_0)\le x_n\le (x_c+x_0) \tag{2.2}$$

Accounting for the radar cross section and, again, extending to the case of a sum of shifted and weighted impulse functions, we have,

$$f(x)=\sum_{n=1}^{N}\sigma_n\delta(x-x_n).\quad (x_c-x_0)\le x_n\le (x_c+x_0) \tag{2.3}$$

Where,

$$x_n=\frac{ct_n}{2}, \tag{2.4}$$

and, t_n, denotes the round-trip time delay to the n^{th} target. Equation 2.4 also serves as the transformation between the time and range domains. When the reflectivity profile of 2.3 is illuminated by a radar waveform, s(t), the signal received will be weighted and shifted as given by the target reflectivity profile, as given by,

$$s_\eta(t)=\sum_{n=1}^{N}\sigma_n s(t-t_n)=\left[\sum_{n=1}^{N}\sigma_n\delta(x-x_n)\right]*s(t)$$

$$s_\eta(t)=f(t)*s(t), \tag{2.5}$$

where the asterisk denotes time-domain convolution. For the case of a continuum of target scatterers whose corresponding reflectivity profile is given by the expression, f(x), the resulting received signal at the radar after application of 2.4 is,

$$s_r(t)=f\left(\frac{ct}{2}\right)*s(t). \tag{2.6}$$

A well-known and often used property to simplify the convolution operation of 2.6, is to use the Fourier transform to switch from the time-domain to the frequency-domain. The advantage of doing so is that the convolution operation becomes multiplicative, thereby reducing 2.6 to,

$$F[s_r(t)] = F\left[f\left(\frac{ct}{2}\right)\right]F[s(t)], \tag{2.7}$$

which is further reduced to,

$$S_r(\omega) = F\left[f\left(\frac{ct}{2}\right)\right]. \tag{2.8}$$

Using the frequency-domain property,

$$F[x(at)] = \frac{1}{a}x\frac{\omega}{a}, \tag{2.9}$$

and applying to equation 2.8 yields,

$$S_r(\omega) = \frac{1}{a}F\left[\frac{\omega}{a}\right]S(\omega), \tag{2.10}$$

where, $a = \frac{c}{2}$. The received signal in the time and frequency domains are given as the pair of equations,

$$s_r(t) = f\left(\frac{ct}{2}\right) * s(t), \tag{2.11}$$

$$S_r(\omega) = \left|\frac{2}{c}\right|F\left[\frac{2\omega}{c}\right]S(\omega). \tag{2.13}$$

Thus, having found the received signal after illumination of the target, we need now to extract the reflectivity profile for HRR imaging. One method for estimating the reflectivity profile, f(x), is to use the following steps:

1. Matched filtering
2. Inverse Fourier transform

Section 2.2.1-Matched Filtering

The matched filtering operation may be interpreted as a correlator and is the optimum detector for a known signal in white-gaussian noise [11]. This can be done via convolution with a time-reversed version of the known signal [19]. The output of the matched filter is given by,

$$s_{out}(t) = s_r(t) * s^*(-t), \tag{2.13}$$

where the superscript asterisk denotes the complex conjugate. In the frequency domain 2.13 would be,

$$S_{out}(\omega) = S_r(\omega) S^*(\omega). \tag{2.14}$$

Substituting 2.10 into 2.14 gives,

$$S_{out}(\omega) = \frac{2}{c} F\left[\frac{2\omega}{c}\right] S(\omega) S^*(\omega), \tag{2.15}$$

$$S_{out}(\omega) = \frac{2}{c} F\left[\frac{2\omega}{c}\right] |S(\omega)|^2 \tag{2.16}$$

Thus, knowledge of $S_{out}(\omega)$, which is measured and $S(\omega)$ which is known, $F\left[\frac{2\omega}{c}\right]$ can be determined from which the reflectivity profile may be estimated via the Fourier transform. Taking the case of discrete target reflectivity profile and ignoring the coefficient, consider,

$$F\left[\frac{2\omega}{c}\right] = F\left[\sum_{n}^{N} \sigma_n \delta(x - x_n)\right], \tag{2.17}$$

$$F\left[\frac{2\omega}{c}\right] = \sum_{n}^{N} \sigma_n e^{j\frac{2\omega}{c}x_n}. \tag{2.18}$$

Let,

$$k_x = \frac{2\omega}{c}, \tag{2.19}$$

denote the transformation to spatial frequency. Substitution of 2.19 and 2.18 into 2.16 yields,

$$S_{out}(\omega) = \sum_{n}^{N} \sigma_n e^{-jk_x x_n} |S(\omega)|^2 . \tag{2.20}$$

Equation 2.20 is the expression for the matched filter output of the discrete reflectivity profile in the spatial frequency domain.

Section 2.2.2-Inverse Fourier Transform

In order to create the high-range resolution (HRR) profile-or more succinctly, to determine the reflectivity profile-the locations and reflectivities of the discrete "point targets" must be determined. First, let us review 2.20. This equation is the output of the matched filter and, as such, contains the information on the location and reflectivity variables, but only in the spatial frequency domain. The HRR profile is a one-dimensional range mapping of the three-dimensional reflectivity profile. Therefore, in order to map the frequency domain representation of the output of the matched filter into the range domain required for the HRR profile,

the inverse Fourier transform is used. Let us consider for a moment, the inverse Fourier transform of 2.20,

$$F^{-1}\left[S_{out}(\omega)\right]=\sum_{n}^{N}\sigma_{n}F^{-1}\left[e^{-jk_{x}x_{n}}\left|S(\omega)\right|^{2}\right], \tag{2.21}$$

$$F^{-1}\left[S_{out}(\omega)\right]=\sum_{n}^{N}\sigma_{n}F^{-1}\left[\left|S(\omega)\right|^{2}\right]\Big|_{t\to t-\frac{2x_{n}}{c}}. \tag{2.22}$$

Now denote,

$$F^{-1}\left[\left|S(\omega)\right|^{2}\right]=\hat{p}(t). \tag{2.23}$$

The above function is called the point spread function. Substituting the expression for the point spread function (PSF) into 2.22 gives,

$$F^{-1}\left[S_{out}(\omega)\right]=\sum_{n}^{N}\sigma_{n}\hat{p}\left(t-\frac{2x_{n}}{c}\right). \tag{2.24}$$

Ideally, the PSF will be a Dirac's delta function, giving both the scaling-radar cross section-and location of the discrete target reflectivity profile. However, this brings forth another oft quoted property of time-frequency transforms: namely for the time-domain representation of the frequency-domain function to be highly localized, the frequency-domain expression must be wideband in nature. The converse is true also, meaning that for a waveform of infinite bandwidth, the Dirac's delta assumption is valid. For most realized radar systems, this is not the case. In general,

$$BW \ll f_{c}, \tag{2.25}$$

where, BW, is the bandwidth of the waveform and, f_c, is the carrier frequency. The PSF can also be expressed in the spatial frequency domain by application of,

$$t = \frac{2x}{c}. \tag{2.26}$$

Thus,

$$\hat{p}_x(x) = \hat{p}_t\left(t - \frac{2x}{c}\right) = \hat{p}_t\left(\frac{2}{c}(x - x_n)\right), \tag{2.27}$$

where the subscripts *x* and *t* denote the spatial and time-domains, respectively. Using the result of 2.27, the spatial-domain point spread function can be shown as,

$$\hat{f}(x) = \sum_n^N \sigma_n \hat{p}_x(x - x_n). \tag{2.28}$$

Equation 2.19 is the spatial frequency corresponding to 2.3. Therefore, consider the time-domain expression for the point spread function,

$$\hat{p}(t) = F^{-1}\left[|S(\omega)|^2\right] \tag{2.29}$$

$$\hat{p}(t) = \int_{-\infty}^{\infty} |S(\omega)|^2 e^{j\omega t} d\omega \tag{2.30}$$

Substitution of 2.26 into 2.30 will result in,

$$\hat{p}(x) = \int_{-\infty}^{\infty} |S(\omega)|^2 e^{j\frac{2\omega x}{c}} d\omega. \tag{2.31}$$

Application of 2.19 to 2.31 results in,

$$\hat{p}_x(x) = \int_{-\infty}^{\infty} |S(k_x)|^2 e^{jk_x x} dk_x, \tag{2.32}$$

where the scaling factor has been ignored. An important note is that the scaling between the time and range domains is specified by,

$$x = \frac{ct}{2} \tag{2.33}$$

$$k_x = \frac{2\omega}{c}. \tag{2.34}$$

Thus, the output of the matched filtering operation can be expressed in either the time or range domain directly by,

$$s_{out}(t) = \left[f\left(\frac{ct}{2}\right) * s(t) \right] * s^*(-t). \tag{2.35}$$

After application of the communicative property of convolution, 2.35 becomes,

$$s_{out}(t) = f\left(\frac{ct}{2}\right) * \left[s(t) * s^*(-t) \right], \tag{2.36}$$

which then yields,

$$s_{out}(t) = f\left(\frac{ct}{2}\right) * p_t(t), \tag{2.37}$$

where,

$$p_t(t) = s(t) * s^*(-t) \tag{2.38}$$

$$p_x(x) = p_t\left(\frac{2x}{c}\right). \tag{2.39}$$

Section 2.3-HRR Algorithms, an Introduction

As stated previously, the role of the high-range resolution (HRR) profile is to graphically display the target reflectivity profile arising from illumination with a transmit waveform. The reflectivity profile carries important information concerning the target. To this end, there has been an abundance of research into analyzing methods for target identification via the HRR profile [5,9,10,14,22,24]. In order to better understand how a three-dimensional range-space can be collapsed into a one-dimensional range-domain representation, a modeling and simulation package was created in Matlab. The package creates a transmit linear-frequency modulated (LFM) waveform and a target in a modified spherical coordinate space. Vector operations are used to determine the resultant received signal after target impact, and a variation of the HRR reconstruction algorithm by Soumekh [19] is used to transform the received signal into the HRR profile.

Section 2.4-Coordinate-Space Considerations

Before undertaking the explanation of the two HRR algorithms, the three-dimensional space the platform and target(s) occupy is introduced. The most important aspect of developing a working radar simulation package is the determination of the line-of-sight vectors. These vectors house the critical range information that will be used in creating the received signal after target impact. Additionally, the range will tell us the exact distance to target along the line-of-

sight and the relative motion and/or direction of travel, if applicable. The following model will not take into account the refractive index gradation as a function of altitude height, thereby decreasing the accuracy of the range data. However, this assumption will simplify calculation, as the refractive index of the atmosphere is highly dependent upon weather conditions, as well as, platform height. The flat earth model is utilized as a basis for modeling the coordinate space the ground target occupies. Finally, there will be an investigation into the effects of frequency-dependent target structures on the accompanied HRR signature.

The spherical coordinate system in conjunction with the Cartesian coordinate system will be used as the Global coordinate system. In the spherical coordinate system, any arbitrary point is located using three coordinates (r,θ,ϕ) as shown in figure 1. Figure 2 shows the geometry of an airborne radar and a target on the ground. In the airborne radar literature, the definition of 'elevation angle' of the radar, θ, is defined as shown in figure 2 and is not to be confused with the conventional definition of the elevation angle used in the spherical coordinate system.

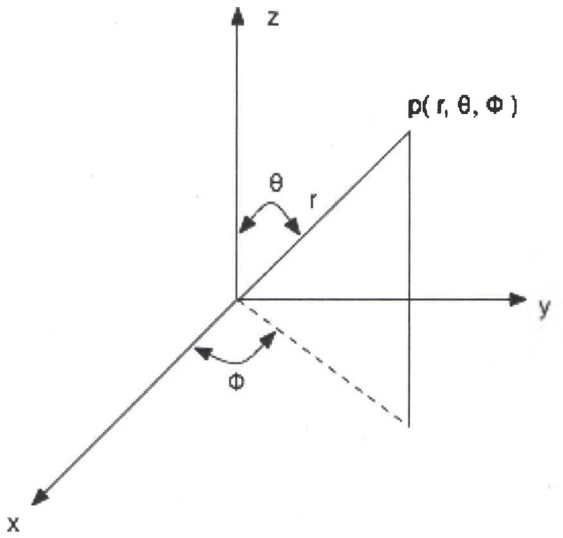

Figure 1: Spherical Coordinate System

With some minor modification, the spherical coordinate system will then describe a generic Post-Detection-Tracking (PDT) arrangement, as shown in figure 2. PDT is the assumption that the target has already been detected and there is no reason to go through a search scan mode in the radar simulation in order to acquire the target in the range swath of interest.

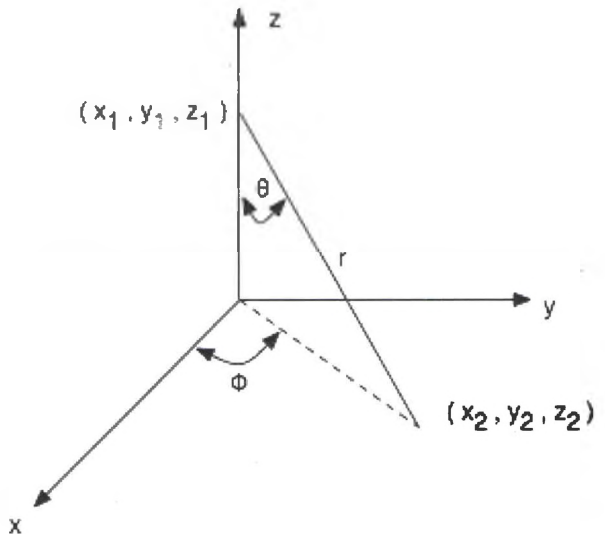

Figure 2: Global Coordinate System

From figure 2, phi is the angle of the radar with respect to the x-axis and is commonly referred to as the azimuth angle. Theta is the angle with respect to the z-axis and is known as the elevation angle. The points representing the target and radar platform location are specified using Cartesian coordinates. Including the information for target and radar platform will transform the above figure into that of figure below.

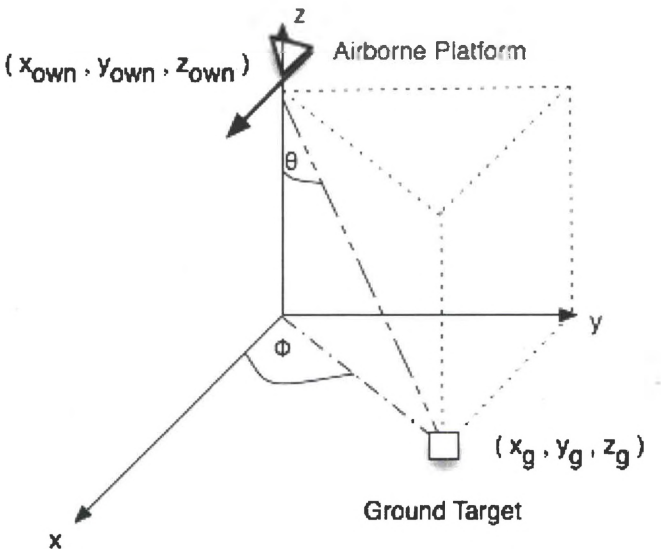

Figure 3: Platform and Target Geometrical Relationship

Next, motion vectors are added to show the direction of relative motion, see figure 4. The velocity vectors can be separated into their respective constituent components via the dot product operation. Using figure 4, the unit vector of the

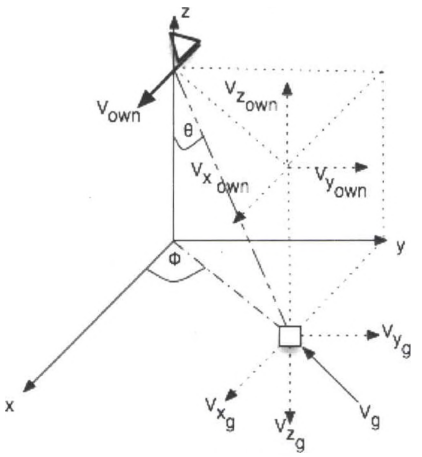

Figure 4: Platform and Target Motion Vectors

One way that the velocity vector components of both the ground target and airborne platform can be found is by using the following diagram and using 2.44 through 2.50.

Determination of the slant range from the target to the platform will be derived with the aid of figure 5, shown below.

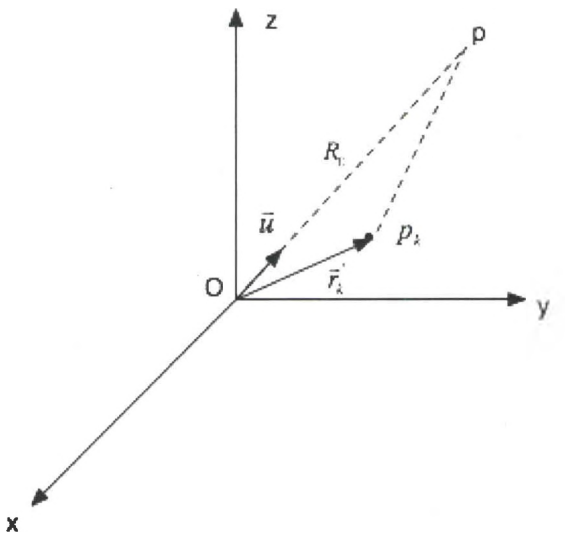

Figure 5: General Slant Range Spatial Relationship

Initially, we will consider the slant range of an arbitrary point, $\vec{p}_k$, with the coordinates, $\left(x_k^{'}, y_k^{'}, z_k^{'}\right)$. The first step is to solve for the vector from the arbitrary point, $\vec{p}_k$, to the location of the generic platform point, p,

$$\overrightarrow{p_k^{'}p} = \overrightarrow{p_k^{'}o} + \overrightarrow{op}\,. \tag{2.44}$$

Equation 2.44 can also be represented by,

$$\overrightarrow{p_k^{'}p} = -\vec{r}_k^{'} + R_o\vec{u}\,. \tag{2.45}$$

The modulus of 2.45 is,

$$\left|\overrightarrow{p_k'p}\right| = \left[\left(R_o\vec{u} - \vec{r}_k'\right)\bullet\left(-\vec{r}_k' + R_o\vec{u}\right)\right]^{1/2}. \tag{2.46}$$

Expanding the dot product,

$$\left|\overrightarrow{p_k'p}\right| = \left[R_o^2 + \vec{r}_k'^2 - 2\vec{r}_k'\bullet R_o\vec{u}\right]^{1/2}. \tag{2.47}$$

By approximation the quadratic term, $\vec{r}_k'^2$, representing the vector to the target point, p_k', as extremely small, 2.47 becomes,

$$\left|\overrightarrow{p_k'p}\right| = \left[R_o^2 - 2\vec{r}_k'\bullet R_o\vec{u}\right]^{1/2}. \tag{2.48}$$

Removing the remaining quadratic term from 2.48 yields,

$$\left|\overrightarrow{p_k'p}\right| = R_o\left[1 - \frac{2\vec{r}_k'\bullet\vec{u}}{R_o}\right]^{1/2}. \tag{2.49}$$

By application of the binomial theorem, 2.49 can be approximated by,

$$\left|\overrightarrow{p_k'p}\right| = R_o\left[1 - \frac{1}{2}\frac{2\vec{r}_k'\bullet\vec{u}}{R_o}\right]. \tag{2.50}$$

Distributing the coefficient, R_o, 2.50 reaches the final form of,

$$\left|\overrightarrow{p_k'p}\right| = R_o - \vec{r}_k'\bullet\vec{u}\,. \tag{2.51}$$

Equation 2.51 represents the expression for the generalized slant range to an arbitrary k^{th} scatterer point.

A more formal treatment of the generalized line-of-sight (LOS) range to an arbitrary k^{th} point will now be given. For this, figure 6 is a useful reference.

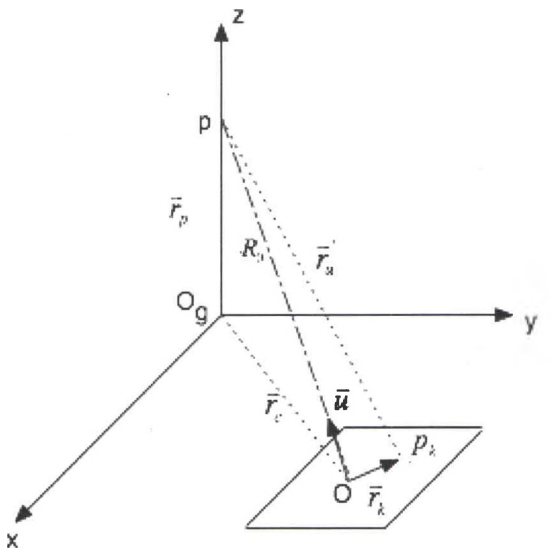

Figure 6: Line-of-Sight Range from Platform to a Point in the Range Swath of Interest

The point, o, refers to the coordinates, (x_c, y_c, z_c), representing the origin of the range swath of interest. Point, o_g, refers to the actual global defined origin at coordinates, (0,0,0). As before, $\vec{u}$, is the unit vector in the direction of the airborne platform from the range swath center. Point, p_k', has coordinates, (x_k', y_k', z_k'). The vector, $\vec{r}_c$, is represented by,

$$\vec{r}_c = \overrightarrow{o_g o}, \tag{2.52}$$

which denotes the vector from the global origin to range swath center. The vector, $\vec{r}_p$, is referenced to the range swath center and points in the direction of the k[th] point, p_k',

$$\vec{r}_p = \overrightarrow{o_g p_k'}. \tag{2.53}$$

The vector from the range swath center to the airborne platform at point, p, is given by,

$$\overrightarrow{op} = \overrightarrow{oo_g} + \overrightarrow{o_g p}\,. \tag{2.54}$$

Substitution of 2.52 and 2.53 into 2.54 yields,

$$\overrightarrow{op} = -\vec{r}_c + \vec{r}_p\,. \tag{2.55}$$

Solving for slant range from range swath center to point, p,

$$R_o = \left[\left(\vec{r}_p - \vec{r}_c\right)\bullet\left(\vec{r}_p - \vec{r}_c\right)\right]^{1/2}, \tag{2.56}$$

which is the modulus of 2.54. In order to solve for the unit vector in the direction of point, p, from range swath center, the following expression is used,

$$\vec{u} = \frac{\vec{r}_p - \vec{r}_c}{R_o}\,. \tag{2.57}$$

Vector, $\vec{r}_u^{'}$, from the k[th] point, $p_k^{'}$, to airborne platform point, p, is given as,

$$\vec{r}_u^{'} = \left(x_k^{'}a_x, y_k^{'}a_y, z_k^{'}a_z\right), \tag{2.58}$$

which is readily found using,

$$\vec{r}_u^{'} = \overrightarrow{oo_g} + \overrightarrow{o_g p_k^{'}}\,. \tag{2.59}$$

Substitution of 2.52 and the vector, $\vec{r}_k^{'}$,

$$\vec{r}_u^{'} = -\vec{r}_c + \vec{r}_k^{'}\,. \tag{2.60}$$

Thus, using the result of equation 2.51, the slant range from an arbitrary k[th] point in a range swath of interest to an airborne platform is,

$$R_{los} = R_0 - \left(\vec{r}_u^{'}\bullet\vec{u}\right). \tag{2.61}$$

Section 2.5-Range-Delay LFM Derivation

Waveform design is a critical aspect of any radar design exercise. The most important considerations that need to be taken into account deal with the underlying physical and phenomenological processes of the radar hardware and target, respectively. Assuming a generic airborne radar platform, attention to the role of the radar is paramount. Is the radar meant to attack, track, or observe? The observation scenario is most pertinent to the formation of the high-range resolution (HRR) profile. Therefore, in order for the radar to glean the maximum information from the target under observation, ambiguities should be nullified by choosing the proper waveform. In relation to the target, *a priori* knowledge would be helpful in determination of the proper waveform for use by the radar platform. The target is assumed to be extended in both range and cross-range. The target is also assumed to have a reflectivity profile that may or may not change as a result of set-on angle, and is linear and time-invariant in nature. This proposition will become increasingly important in section 4.3, when the statistical basis for the HRR signature is introduced.

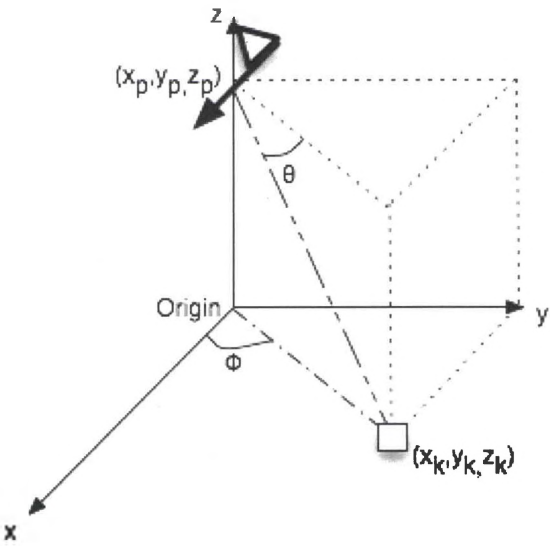

Figure 7: Platform-Target Spatial Relationship

After transmit, the waveform passes through free-space and encounters the target of interest. This waveform-target interaction is called impact. After impact, a portion of the signal reflects off of the target back into free-space. The signal will then be captured by the radar hardware and processed. For the general case of an extended target structure, comprised of many discrete scatterers, individual scatterers will be denoted by the constant *k*. The geometry of a typical scatterer, the k^{th} scatterer is shown in Figure 7, which shows the relationship between the airborne radar platform and the individual point target. The projection of the three-dimensional target on the x-y plane is considered. This will be true regardless of the target range extent.

To mathematically model the received signal after interaction with the k^{th} scatterer, the following assumptions are made:

- Reflectivity changes negligibly pulse-to-pulse
- If the target has no radial velocity, $f_d = 0$ Hz

In order to effectively model the waveform-IPT interaction, the following will need to be taken into consideration:

- Range of target relative to radar
- Velocity of target relative to radar (Doppler)
- Rate of change relative to radar (pulse-to-pulse)
- Scatterer Characteristics

The scatterer characterisitics will account for the scatterer's effective reflectivity with respect to the range and pulse-to-pulse rate of range change relative to the radar platform, and will be denoted by α.

As previously stated, the received signal will rely on a calculation of the effective line-of-sight (LOS) range from platform to target. Thus, we must now consider the mathematical description of the target with respect to, range and target radial velocity. Figure 8 will be a useful legend for the remainder of the mathematical analysis.

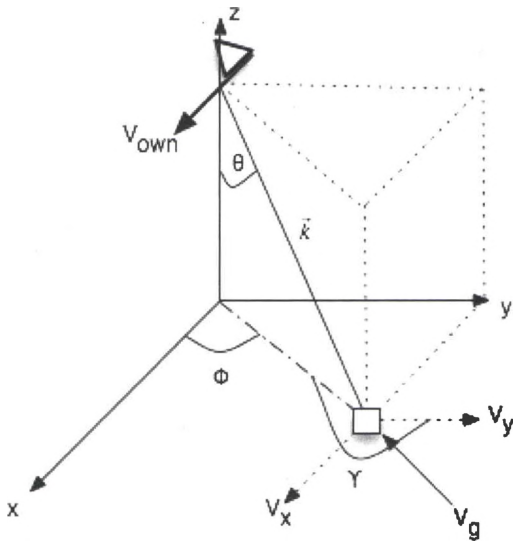

Figure 8: Detailed Platform-Target Coordinate Space Model

Key
θ = Initial target elevation
ϕ = Initial target azimuth
γ = Angle from ground target velocity vector to y-axis in x-y plane, in radians
V_g = Velocity of ground target in x-y plane
V_x = X-component of ground target velocity
V_y = Y-component of ground target velocity
V_{own} = Velocity of aircraft, assumed to be in the x-direction.

First, there must be a uniform definition of the spatial references. Since we are only concerned with a single channel system, all ranges and line-of-sight vectors are referenced to the center of the range swath under illumination by the radar. Using Figure 8 to find the vector describing the combined relative velocity between the aircraft and the ground moving target along the LOS vector, $\vec{k}$, yields,

$$V_{c_{los}} = V_{own}\cos(\phi)\sin(\theta) - \left[V_g \sin(\gamma_g)\cos(\phi) + V_g \cos(\gamma)\sin(\theta)\right]\cos(90^\circ - \theta). \quad (2.62)$$

The above equation is an important component of the return signal captured by the airborne radar platform. An investigation of the effect a target has on the echo signal, is now considered. From the transmit waveform for the LFM signal is represented as,

$$s(t) = a(t)\exp\left[j\left(2\pi f_o t + \gamma t^2\right)\right], \tag{2.63}$$

where $\gamma = \frac{BW}{T_o}$. T_o is the pulse period, f_o is the RF carrier in hertz, and a(t) is the windowing function. The windowing function is rectangular and has unit amplitude for the time period,

$$a(t) = \begin{cases} 1, & |t| \le T_o/2 \\ 0, & \text{else} \end{cases}. \tag{2.64}$$

After impact with a given target, the signal scatters. Some of this scattering reaches the airborne platform radar antenna. The received signal has an amplitude decay and a round-trip time delay. The round-trip delay time arises due to the distance the transmit signal must travel before impact and reflection back to the airborne receiver and is given by, $t_d = \frac{2R}{c}$, with c being the speed of light. The distance between the k^{th} point target and the radar antenna is,

$$R_k(t) = R_k + V_k t, \tag{2.65}$$

where R_k is the initial range to the target, V_k is the ground-target induced relative velocity. In order to account for the relative motion of both the airborne platform and target over a dwell period, the relativistic Doppler equation is used [6],

$$V_k = \frac{\vec{p} - \vec{r}_k'}{1 - \frac{\vec{p} \bullet \vec{r}_k'}{c}}. \tag{2.66}$$

The velocity vectors of the airborne platform and ground-target are denoted by $\vec{p}$ and $\vec{r}_k'$, respectively. Accounting for the distance to range swath center, R_o, equation 2.65 becomes,

$$\tilde{R}_k(t) = R_k - R_o + V_k t. \tag{2.67}$$

For an actual radar system, multiple pulses are transmitted for purposes of increasing the signal-to-noise ration. Let,

$$\tilde{t} = t - lT, \tag{2.68}$$

denote the coherent processing interval (CPI) time variable. The variables T and l are the pulse repetition interval (PRI) and CPI pulse index, respectively. Assuming a zero relative motion Doppler shift, the received signal for the k^{th} point scatterer is given by [23],

$$r_k(t) = a_k(\tilde{t}) \exp\left(j\left[2\pi f_o \left(\tilde{t} - \tau_o - \frac{2\tilde{R}_k(t)}{c} \right) + \gamma \left(\tilde{t} - \tau_o - \frac{2\tilde{R}_k(t)}{c} \right)^2 \right] \right), \tag{2.69}$$

where τ_o is the round-trip time delay references to range swath center and $a_k(\tilde{t})$ denotes a time-varying reflectivity. We note that,

$$\left| \tilde{t} - \tau_o - \frac{2\tilde{R}_k(t)}{c} \right| \leq \frac{T_0}{2}. \tag{2.70}$$

The radar antenna receiver is open for only a short period of time relative to the pulse repetition interval (PRI), assuming multiple transmit pulses were used over the coherent processing interval (CPI).

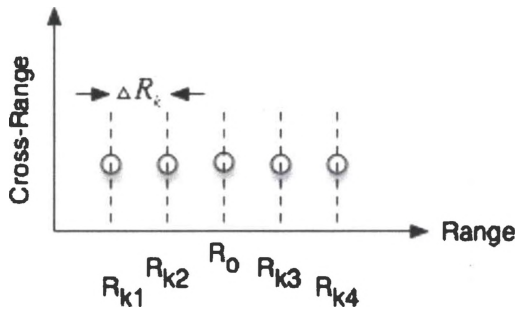

Figure 9: Targets Within Range Swath

Figure 9 shows five targets collinear in range for a given range swath patch. The distance between any of these points is small in comparison with the pulse period,

$$\left(t_{k1} - t_{k2}\right) \ll T_o . \tag{2.71}$$

Equation 2.71 can be rearranged into a range expression from the time expression listed, thus,

$$\Delta R_k \ll \frac{2T_o}{c} . \tag{2.72}$$

As a short example, if the pulse period were four microseconds, the corresponding unambiguous range would be,

$$R_u = 3e8 \frac{m}{s} \frac{4\mu s}{2} = 12km . \tag{2.73}$$

Clearly, for an extended target of realistic size, kilometers would not be an appropriate choice of length measurement. If a generic tank model were used, surely the range swath of interest would be less than ten meters in either range or cross-range. Thus, the assumed discrete scatterers that give rise to the tank

reflectivity profile are even closer together than the size of the entire range swath of interest.

For a general target model comprised of K-scatterers, the radar antenna receiver would be open for the time period of,

$$t_1 \le t_{dk} \le t_K + T_o. \tag{2.74}$$

The receiver would turn on at a time corresponding to the first target scatterer, or the set-on scatterer. The receiver would stay on for a period of time equal to the distance from the last expected target scatterer plus the pulse period. This is necessary as each received signal is a reflected transmit pulse of length, T_o. In order to capture the final target scatterer, the receiver must stay on for a period of time equal to the time-delay to the k^{th} point target plus T_o.

Subsection 2.5.1-Reference Signal

Having introduced the expression for the received signal from the k^{th} point scatterer, the reference signal must be found in order to complete the matched filtering operation necessary for creation of the high-range profile. The reference chirp signal is,

$$s_r(\tilde{t} - \tau_o) = \exp\left(j\left[2\pi f_o(\tilde{t} - \tau_o) + \gamma(\tilde{t} - \tau_o)^2\right]\right), \tag{2.75}$$

with,

$$|\tilde{t} - \tau_o| \le T_o/2 \ . \tag{2.76}$$

Pulse compression will transform the chirp rate into a linear ramping. This allows the pulse compressed signal to be sampled and pre-processed in preparation for

the matched filtering operation. Pulse compression is achieved through hardware mixing in the radar receiver. Mathematically, this operation is modeled as [23],

$$y_k(\tilde{t},l) = r_k(t)s_r^*(\tilde{t}-\tau_o). \tag{2.77}$$

Expanding the received and reference signal notation [23],

$$y_k(\tilde{t},l) = a_k(\tilde{t})\exp\left(j\left(2\pi f_o\left(\tilde{t}-\tau_o-\frac{2\tilde{R}_k(t)}{c}\right)+\gamma\left(\tilde{t}-\tau_o-\frac{2\tilde{R}_k(t)}{c}\right)^2\right)\right)\cdots \\ \exp\left(-j\left(2\pi f_o(\tilde{t}-\tau_o)+\gamma(\tilde{t}-\tau_o)^2\right)\right). \tag{2.78}$$

Appendix 1A includes a complete derivation of the steps involved in reducing 2.78 into,

$$y_k(\tilde{t},l) = a_k(\tilde{t})\exp\left(-j\left(2\pi f_o\frac{2\tilde{R}_k(t)}{c}+\gamma\left((\tilde{t}-\tau_o)\frac{4\tilde{R}_k(t)}{c}-\frac{4\tilde{R}_k^2(t)}{c^2}\right)\right)\right). \tag{2.79}$$

Rearranging the result of 2.79 yields,

$$y_k(\tilde{t},l) = a_k(\tilde{t})\exp\left(j\frac{4\tilde{R}_k^2(t)}{c^2}\right)\exp\left(-j\left(\frac{2\tilde{R}_k(t)}{c}\left(2\pi f_o+2\gamma(\tilde{t}-\tau_o)\right)\right)\right). \tag{2.80}$$

Replacing $\tilde{R}_k(t)$ with $R_k+R_o+V_kt$ for the quadratic term in equation 2.80 gives,

$$\exp\left(j\frac{4\tilde{R}_k^2(t)}{c^2}\right) = \exp\left(j\left(\frac{4\gamma(R_k-R_0)}{c^2}\right)\right)\exp\left(j\left(\frac{8\gamma(R_k-R_0)V_kt}{c^2}\right)\right)\exp\left(j\left(\frac{4\gamma V_k^2t^2}{c^2}\right)\right). \tag{2.81}$$

Appendix 1B addresses the expansion of the quadratic term. An explanation of each of the three terms in equation 2.83 will help to elucidate their meaning [23]:

1. $\exp\left(j\left(\frac{4\gamma(R_k-R_0)}{c^2}\right)\right)$, constant, rolled into the coefficient, $\alpha_k(\tilde{t})$

2. $\exp\left(j\left(\frac{8\gamma(R_k - R_0)V_k t}{c^2}\right)\right)$, significant term, kept for further processing

3. $\exp\left(j\left(\frac{4\gamma V_k^2 t^2}{c^2}\right)\right)$, the phase is quadratic in time, typically very small and hence ignored

Retaining the second term,

$$\exp\left(j\left(\frac{8\gamma(R_k - R_0)V_k t}{c^2}\right)\right), \tag{2.82}$$

and substituting into 2.80 results in,

$$y_k(\tilde{t},l) = a_k(\tilde{t})\exp\left(-j\left(\frac{2(R_k - R_0)}{c}(2\pi f_0 + 2\gamma(\tilde{t} - \tau_0))\right)\right)\ldots$$
$$\exp\left(-j\left(\frac{2V_k(\tilde{t} + lT)}{c}(2\pi f_0 + 2\gamma(\tilde{t} - \tau_0))\right)\right)\exp\left(-j\left(\frac{8\gamma(R_k - R_0)}{c^2}V_k(\tilde{t} + lT)\right)\right), \tag{2.83}$$

see appendix 2C for a complete derivation. The following is a summary of the significance of each term in 2.83 [23]:

1. $\exp\left(-j\left(\frac{2(R_k - R_0)}{c}(2\pi f_0 + 2\gamma(\tilde{t} - \tau_0))\right)\right)$, accounts for effects of the scatterers initial position relative to the reference point. This is the standard form of a return pulse for a stationary point scatterer.

2. $\exp\left(-j\left(\frac{2V_k(\tilde{t} + lT)}{c}(2\pi f_0 + 2\gamma(\tilde{t} - \tau_0))\right)\right)$, accounts for movement of the scatter between for interpulse and intrapulse periods.

3. $\exp\left(-j\left(\frac{8\gamma(R_k - R_0)}{c^2}V_k(\tilde{t}+lT)\right)\right)$, this is the remaining portion of the quadratic term.

Through substitution of $\lambda = c/f_0$ and $\tau_0 = 2R_0/c$ into 2.83, we have [23],

$$y_k(\tilde{t},l) = a_k(\tilde{t})\exp\left(-j\left(\frac{4\gamma(R_k - R_0)\tilde{t}}{c}\right)\right)\exp\left(-j\left(\frac{4\pi V_k\tilde{t}}{\lambda} - \frac{8\gamma R_k V_k\tilde{t}}{c^2}\right)\right)\cdots$$
$$\exp\left(-j\left(\frac{4\gamma V_k\tilde{t}^2}{c}\right)\right)\exp\left(-j\left(\frac{4\gamma V_k\tilde{t}lT}{c}\right)\right)\exp\left(-j\left(\frac{4\pi V_k lT}{\lambda} - \frac{8\gamma R_k lT}{c^2}\right)\right), \quad (2.84)$$

see appendix 2.D for details.

1. $\exp\left(-j\left(\frac{4\gamma(R_k - R_0)\tilde{t}}{c}\right)\right)$, accounts for the frequency offset caused by the scatterer's initial position relative to the range swath center.

2. $\exp\left(-j\left(\frac{4\pi V_k\tilde{t}}{\lambda} - \frac{8\gamma R_k V_k\tilde{t}}{c^2}\right)\right)$, accounts for target movement intrapulse.

3. $\exp\left(-j\left(\frac{4\gamma V_k\tilde{t}^2}{c}\right)\right)\exp\left(-j\left(\frac{4\gamma V_k\tilde{t}lT}{c}\right)\right)$, also accounts for target movement intrapulse. This term, which is quadratic in time, may be approximated by a constant term. This constant term will then be rolled into the $\alpha_k(\tilde{t})$ constant coefficient.

4. $\exp\left(-j\left(\frac{4\gamma V_k\tilde{t}lT}{c}\right)\right)$, represents the frequency change that occurs from pulse-to-pulse as a result of the change in the line-of-sight range to the point target.

5. $\exp\left(-j\left(\frac{4\pi V_k lT}{\lambda}-\frac{8\gamma R_k lT}{c^2}\right)\right)$, accounts for the phase shift that occurs interpulse. This change in phase is responsible for Doppler frequency shift.

Thus, by rolling the quadratic term into the constant coefficient, 2.84 becomes,

$$y_k(\tilde{t},l)=a_k(\tilde{t})\exp\left(-j\left(\frac{4\gamma(R_k-R_0)\tilde{t}}{c}\right)\right)\exp\left(-j\left(\frac{4\pi V_k\tilde{t}}{\lambda}-\frac{8\gamma R_k V_k\tilde{t}}{c^2}\right)\right)\cdots \exp\left(-j\left(\frac{4\gamma V_k\tilde{t}lT}{c}\right)\right)\exp\left(-j\left(\frac{4\pi V_k lT}{\lambda}-\frac{8\gamma R_k lT}{c^2}\right)\right). \quad (2.85)$$

After pulse compression has been accomplished in the radar receiver hardware, the signal needs to be sampled for further processing into the HRR profile. Setting,

$$\tilde{t}=nT_s, \quad (2.86)$$

with *n* being the sample index and T_s the sampling rate, the pulsed compressed signal can be modeled as,

$$y_k(n,l)=\sum_{k=1}^{K}y_k(nT_s,l), \quad (2.87)$$

for the case of all K-scatterers. This result ignores clutter and noise contributions, but will be valid for modeling and simulation purposes, since all processing is assumed to be exoclutter with ideal transmit and receiver hardware.

Section 2.6-HRR Range Reconstruction Algorithm

The following discussion details the implementation of the linear-frequency modulation (LFM) derived high-range resolution profile as discussed in Soumekh [1]. The signal analyzed is the upsweep, or upchirp, (LFM) waveform or chip. The LFM waveform is represented by the function given,

$$s(t) = a(t)\exp\left(j\beta t + j\alpha t^2\right). \tag{2.88}$$

Where a(t) is a windowing function, α alpha is the chirp rate, β is the carrier frequency, and time is $|t| \le T_o/2$. In most cases the windowing function can be represented by a rectangular window,

$$a(t) = \begin{cases} 1, & |t| \le T_o/2 \\ 0, & \text{else} \end{cases}. \tag{2.89}$$

Additionally, a chirp waveform is a form of phase modulation (PM). Solving for the instantaneous bandwidth through derivation of the phase of 2.88, over the valid time period given in 2.89, yields[19],

$$\begin{aligned} \omega_{if} &= \left(\beta t + \alpha t^2\right)\frac{d}{dt}. \\ \omega_{if} &= \beta + 2\alpha t \end{aligned} \tag{2.90}$$

The waveform is centered around the carrier frequency with effective bandwidth given by [19],

$$\begin{aligned} \omega_{if} &= \beta \pm \alpha t \\ \omega_{if} &\in \left[\beta - \alpha t, \beta + \alpha t\right] \end{aligned} \tag{2.91}$$

Thus, the carrier frequency can easily be found to be,

$$\omega_c = \beta . \tag{2.92}$$

This carrier frequency is in the X-Band (8-12.5 GHZ) and specifically 10 GHz. Solving for the baseband chirp signal [19],

$$\pm\omega_{bb} = \pm\alpha T_p , \tag{2.93}$$

with T_p representing the pulse period of the transmit waveform. The echo range delay imposed by a single point target is given by,

$$t_k = \frac{x_k}{2c}. \tag{2.94}$$

For the case of a single point target, the received signal is of the form [19],

$$s(t) = \sigma_k rect(t - t_k)\exp\left[j\beta(t - t_k) + j\alpha(t - t_k)^2 \right], \tag{2.95}$$

with σ_k denoting the reflectivity of the target as a function of the radar-cross section. Substituting 2.94 into 2.95 yields [19],

$$s(t) = \sigma_k rect\left(t - \frac{x_k}{2c} \right)\exp\left[j\beta\left(t - \frac{x_k}{2c} \right) + j\alpha\left(t - \frac{x_k}{2c} \right)^2 \right]. \tag{2.96}$$

Generalizing for the case of K point-target scatterers, the above expression becomes [19],

$$s(t) = \sum_{k=1}^{K} \sigma_k rect\left(t - \frac{x_k}{2c} \right)\exp\left[j\beta\left(t - \frac{x_k}{2c} \right) + j\alpha\left(t - \frac{x_k}{2c} \right)^2 \right], \tag{2.97}$$

and distributing the square in 2.97 gives,

$$s(t) = \sum_{k=1}^{K} \sigma_k rect\left(t - \frac{x_k}{2c} \right)\exp\left[j\beta\left(t - \frac{x_k}{2c} \right) \right]\exp\left[j\left(\alpha t^2 - 2\alpha t_k t + \alpha t_k^2 \right) \right]. \tag{2.98}$$

To form the high-range resolution (HRR) profile for the above received signal, the LFM waveform is pulse-compressed to remove the quadratic frequency modulation term. This step in the reconstruction algorithm is achieved by mixing the received signal with the complex conjugate of the transmitted signal to yield the compressed or deramped chirp signal,

$$s_c(t) = s^*(t)\exp\left(j\beta t + j\alpha t^2\right), \tag{2.99}$$

with supercript * denoting complex conjugation of the transmit waveform. The resultant pulse-compressed received waveform becomes [19],

$$s_c(t) = \sum_{k=1}^{K} a\left(t - \frac{x_k}{2c}\right)\exp\left[j\beta\frac{x_k}{2c} - j\alpha\left(\frac{x_k}{2c}\right)^2\right]\exp\left(j2\alpha t_k t\right), \tag{2.100}$$

where the σ_k is assumed unity for all echo returns. The term,

$$\exp\left(j2\alpha t_k t\right) \tag{2.101}$$

in the above expression is the time shifted sinusoid, where $t_k = \frac{x_k}{2c}$ determines the fundamental frequency of the sinusoid. The residual-video phase (RVP) term, $\exp\left[j\beta\frac{x_k}{2c} - j\alpha\left(\frac{x_k}{2c}\right)^2\right]$, is useful for synthetic aperture radar to eliminate the cross-range of the target reflectivity profile [19], but is not important for construction of the HRR profile. Analysis of the Fourier spectrum 2.101 of the pulse-compressed signal will result in an energy distribution at the frequency denoted by $2\alpha t_k$ [19],

$$S_c(\omega) = F\left[\exp\left(j2\alpha t_k t\right)\right], \tag{2.102}$$

$$S_c(\omega) = psf_\omega\left(\omega - 2\alpha t_k\right). \tag{2.103}$$

The expression, 2.103, above is the point-spread function (PSF) of the pulse-compressed received signal. The remainder of the expression, classified as a phase function, was left unaltered. Inverse Fourier analysis of the PSF will yield a time shifted sinc-like function in the time domain,

$$\frac{\sin(\pi BWt)}{\pi BWt}. \tag{2.104}$$

The figure shown below illustrates 2.104 for the case where the time delay of zero corresponds

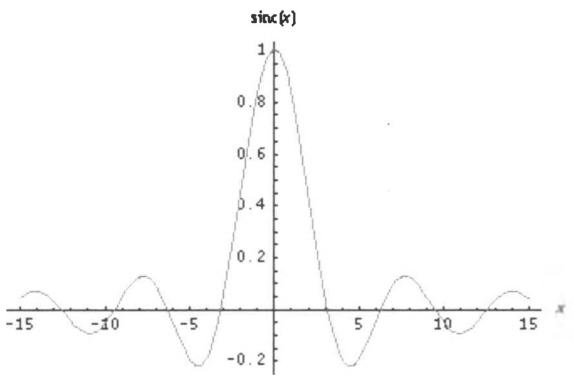

Figure 10: Generalized Sinc Function

to the center of the range swath illuminated by the transmit waveform.

The advantage inherent in the LFM waveform is the increase in range resolution given by the inclusion of a linear-ramp frequency modulation. This is shown by the range resolution equation for a linear chirp pulsed waveform [19],

$$\Delta_x = \frac{\pi c}{2\alpha T_p}, \tag{2.105}$$

where α is the chirp rate and T_p is the pulse period; as the chirp rate is increased, so is the resolution of the waveform. Since the chirp rate can be orders of magnitude higher than the numerator of 2.105, range resolution can be quite high. Practically, due to the limits of analog-to-digital (A/D) converters available, the maximum bandwidth of an LFM waveform is around 1 GHz.

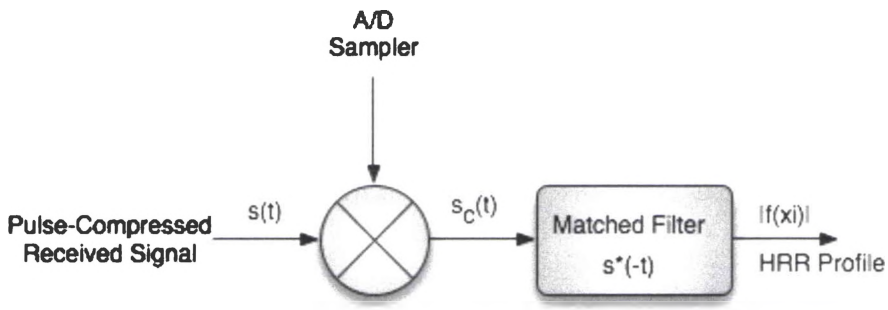

Figure 11: Block Diagram of Sampling and Matched Filtering

Having found the pulse-compressed received signal in 2.100, the signal is then converted to a digital form via an A/D converter. While the general Nyquist sampling criteria should be valid for 2.100, the Nyquist sampling rate is not constant for the time domain and range domain signal cases. To better illustrate this rationale, let the time domain sampling criteria be [19],

$$\Delta_t \leq \frac{\pi}{\omega_0}, \tag{2.106}$$

where,

$$\omega_0 = \alpha T_p . \tag{2.107}$$

Substitution of 2.107 into 2.106 yields [19],

$$\Delta_t \leq \frac{\pi}{\alpha T_p} . \tag{2.108}$$

Now, using the range domain notation, let the value for the range given by,

$$x = \frac{c}{4\alpha}\omega . \tag{2.109}$$

Thus the valid range support band is [19],

$$x \in \left[\frac{4\alpha}{c}(X_c - X_0), \frac{4\alpha}{c}(X_c + X_0) \right]. \tag{2.110}$$

This yields the center carrier,

$$\omega_{cc} = \frac{4\alpha}{c} X_c , \tag{2.111}$$

and the base support band,

$$\omega_{0c} = \frac{4\alpha}{c} X_0 , \tag{2.112}$$

respectively. Rearranging the notation of 2.111,

$$\omega_{0c} = \frac{4\alpha}{c} X_0 , \tag{2.113}$$

and 2.113,

$$\omega_{0c} = \alpha T_x , \tag{2.117}$$

yields the range domain support baseband. Solving for the range swath time delay period [19],

$$T_x = \frac{4X_0}{c} . \tag{2.115}$$

we notice that the Nyquist rate for the temporal and range domains are not equal,

$$\Delta_t \le \frac{\pi}{\alpha T_p} \neq \Delta_{tc} \le \frac{\pi}{\alpha T_x}. \tag{2.116}$$

In order to avoid violation of the Nyquist rate, the received chirp signal should pass through a baseband conversion mixing where the range center carrier is included as a correction factor. Below is listed the corrected pulse-compression scheme for the received LFM waveform [19],

$$s_{cb}(t) = s^*(t)\exp\left(j\beta t + j\alpha t^2 - j\omega_{cc}t\right), \tag{2.117}$$

$$s_{cb}(t) = s^*(t)\exp\left(j\beta t + j\alpha t^2 - j\frac{4\alpha X_c}{c}t\right). \tag{2.118}$$

The corrected baseband signal is then upsampled using the Fast-Fourier Transform (FFT); the FFT function will essentially zero-pad the range baseband compressed signal and using the Inverse Fast-Fourier Transform (IFFT) will produce the properly Nyquist sampled time domain signal. Upsampling is only necessary for the condition where $\Delta_{tc} < \Delta_t$ is true [19]. Having the properly baseband shifted, sampled and upsampled received signal, we must now reconstruct the received signal via pulse decompression. This is accomplished by mixing the conjugate of the sampled range domain baseband compressed signal with the range domain reference phase to decompress the chirp signal [19],

$$s(t_i) = s_{cb}{}^*(t_i)\exp\left(j\beta t_i + j\alpha t_i{}^2 - j\omega_{cc}t_i\right). \tag{2.119}$$

Finally, 2.119 is converted to baseband via mixing with a local oscillator and matched filtered to yield the HRR. The baseband conversion operation using the new sampling rate is [19],

$$s_b(t_i) = s(t_i)\exp(-j\omega_c t_i). \tag{2.120}$$

Thus matched filtering with the reference baseband echo signal [19],

$$s_{0b}(t_i) = \exp\left(j\beta t_i + j\alpha t_i^2\right), \tag{2.121}$$

in the frequency domain gives the matched filtered output [19],

$$S_{Mb}(\omega_i) = f(x_i) = F\left[s_b(t_i - t_k)s_{0b}{}^*(t_i)\right]. \tag{2.122}$$

The magnitude and inverse Fourier transform of 2.122 is known as the HRR profile and is thus [19],

$$|s_{HRR}| = \sqrt{F^{-1}\left[S_{Mb}^2(\omega_i)\right]}. \tag{2.123}$$

The HRR profile is an image of the target reflectivity profile. This image is comprised of a single point-spread function (PSF) for each scattering center within the range swath under illumination. The weighted, coherent sum of these PSF's is called the HRR profile. The PSF is not a single value, but is rather a continuum of values extending to infinity. The coherent sum of the weighted PSF's will result in constructive or destructive interference, giving rise to the final HRR profile. Therefore, the HRR profile is not merely a collection of point-target return signatures, but rather an interference pattern of a number of PSF's. The HRR profile, over a number of individual look angles for a given pose angle, constitutes the HRR signature process. The scattering phenomena underlying a

complex target, which may be useful in identification of the target, are obscured by the interference making the design of automatic-target recognition algorithms difficult.

Section 2.7-Testing for Targets in Range

To better illustrate the effect target range has on the high-range resolution (HRR) profile, the following scenario is considered: one, then multiple targets are distributed in range and processed separately, then together, to show the range dependency on the target reflectivity profile. Assumptions regarding the range swath space and the target reflectivity characteristics are now introduced. In order to eliminate the ambiguity that arises from the echo return emanating from a waveform illuminated range swath, all testing is assumed to be exoclutter, where clutter denotes the reflectivity profile of the ground. While actual radar systems have a single mainlobe and multiple sidelobes that contribute to clutter returns, the echoes resulting from sidelobe returns are assumed null. All targets are assumed to be point target models with equal reflection coefficients. We are using the ideal point target model to isolate the HRR profile contributions to just the location and pose-angle to the radar platform. This allows for a study of the underlying HRR subspace and signal subspace statistics with the only contributing factors being the signal processing and initial platform-target locations.

The waveform used for all testing is the linear frequency modulated (LFM) waveform. Section 2.5 contains detailed information regarding effects the target has on the echoed return signal. For the purpose of simulation, the radar is considered to operate at X-band, have range resolution of approximately one foot and utilize a traveling wave tube with a 5% duty cycle. Radar systems parameters are listed in table 1.

Table 1: Radar Design Parameters

Pulsed Medium-PRF PDT Fire and Control Radar		
Operating Frequency	X-Band (Radar)	10 GHz
TWT DC %	5%	
Peak Power	1 kW	
Pulse Period	4 μs	
Bandwidth	500 MHz	
PRF	12.5 kHz	
Range Resolution	0.3 m	~1 ft
Beamwidth	$\phi_{az} = 1°$	$\phi_{el} = 1°$
Unambiguous Range	12 km	
Unambiguous Velocity	± 93.75 m/s	@ 10 GHz

In a LFM radar system, after impact, some of the reflected signal will reach the airborne antenna. This received signal is then heterodyned, or mixed, with a complex conjugate of the transmitted waveform phase. The resulting complex video signal is obtained as the inphase and quadrature (IQ) components [20]. Commonly, this signal processing technique is referred to as pulse compress on receive. After low pass filtering (LPF) to remove the radio-frequency (RF) components, the pulsed compressed waveform is sampled and either stored or processed further via matched filtering and inverse Fourier transform to create the HRR profile. The pulse compressed received signal corresponding to a

single point target, when plotted versus time, resembles a sinusoid. If the received signal is from the range swath center, the pulsed compressedis a sinusoid of zero-frequency, that is DC. For signals emanating from elsewhere in the range swath, the corresponding sinusoidal frequencies depend upon their distance from the radar range swath center. This distance is best imagined as a time delay, where the corresponding sinusoid is the Doppler related to the time delay. Thus, when referenced to range swath center, the pulse-compressed sinusoid is a higher Doppler if closer to the airborne platform and lower Doppler for targets further away.

A scenario comprising these targets is used to illustrate this concept. This scenario is better illustrated with the figure shown in figure 12. Target T_1 is assumed to be at range swath center. Target T_2 is located several range bins away from range swath center: where a range bin is defined as the range resolution of the transmit waveform. Finally, target T_3 is only one range bin from range swath center. In order to illustrate this concept, the following simulation will serve as a good reference. Targets are distributed in range. The range resolution of this radar is 0.3 m, or approximately one foot. In order to allow for easy discrimination of individual targets, three separate ranges were chosen: range swath center and +/- some distance *x* from range swath center. The response of the radar for each of the targets separately and when all these are present will be shown.

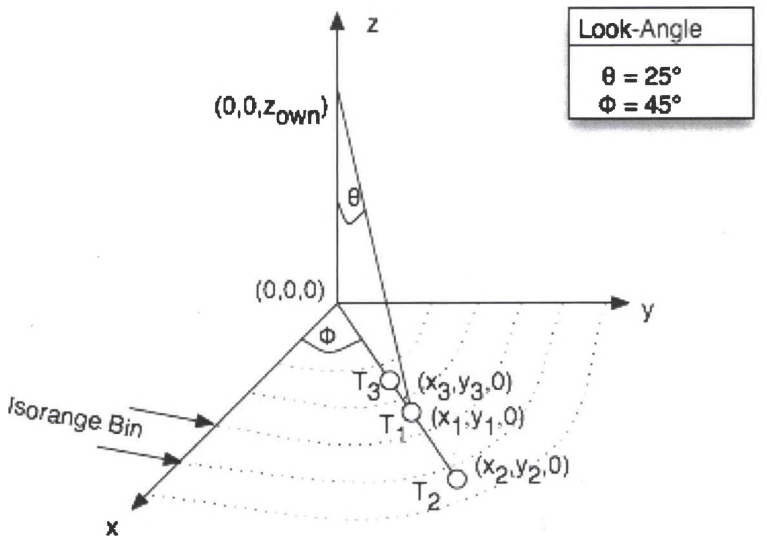

Figure 12: Targets Distributed in Range Only

The echo delay signal consists solely of target T_1 with the azimuth and elevation look-angles being 45° and 25°, respectively. Table 2 contains more information regarding the coordinates and properties of target T1.

Table 2: Target and Platform Coordinate Details

	Platform	Target		
	ϕ=45°, θ=25°	T1	T2	T3
Reflectivity	NA	1	1	1
x-location	0 m	2.1213 km	2.1220 km	2.1211 km
y-location	0 m	2.1213 km	2.1220 km	2.1211 km
z-location	6.4345 km	0 m	0 m	0 m
R_{los}	NA	7.0986 km	7.0990 km	7.0985 km

The signal following pulse compression on receive is plotted versus time and is shown in figure 13.

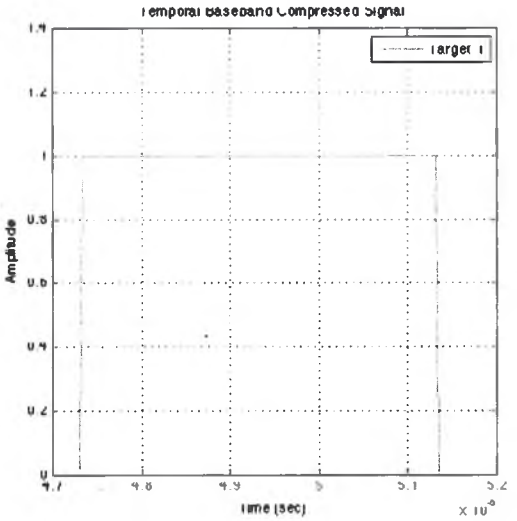

Figure 13: Pulse-Compressed T1 Echo Delay Signal

As expected, this signal after pulse compression is a rect function. After pulse compression, the signal is sampled and quantized for further digital signal processing in the radar hardware. The sampling of figure 13 is shown below:

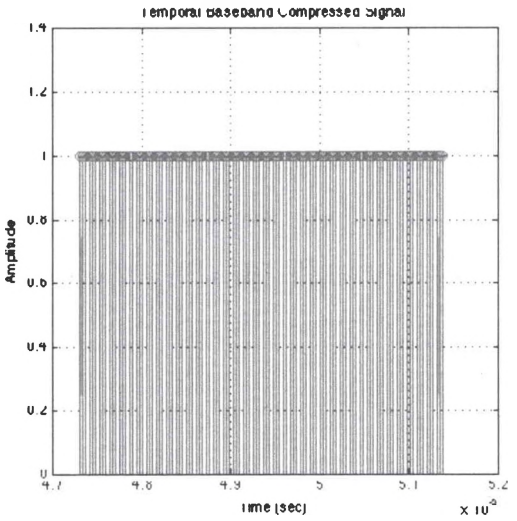

Figure 14: Sampled Pulse Compressed T1 Echo Delay Return

Carrying out matched filtering and displaying the magnitude of the inverse Fourier transform of the result gives the HRR profile:

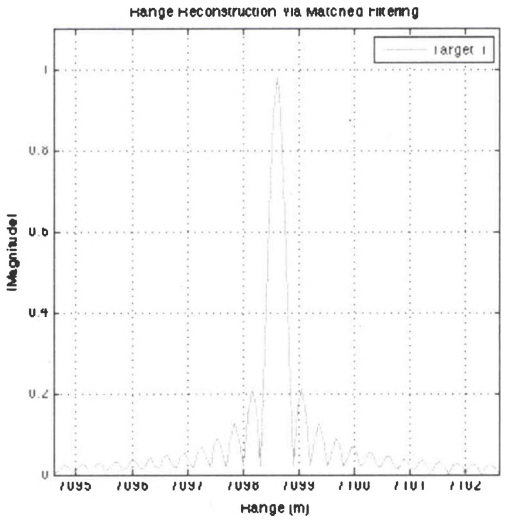

Figure 15: HRR Profile of T1

Without having a formal definition of the HRR algorithm in view, the result of figure 15 is somewhat expected. The Fourier transform of the rect function is the sinc function. The magnitude of the sinc function would be that of figure 15. Overlaying the sample points onto figure 15 and limiting the viewing window to that of range swath center +/- 0.5 m gives figure 16.

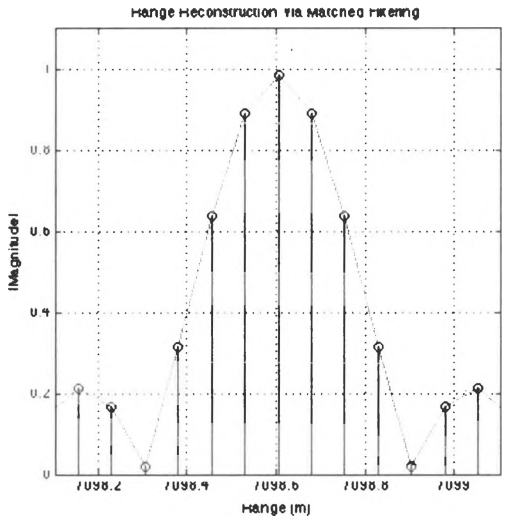

Figure 16: 1 m Cut of Sampled HRR Profile for T1

The HRR profile is a sampled and quantized version of the actual reflectivity profile emanating from an illuminated range swath of interest.

To make the results more interesting, a range position some distance in meters from range swath center is chosen for two other ideal point targets. The first target is located 1 meter further away from the airborne platform, referenced to the range swath center. The resultant sinusoid from pulse compress on receive is shown below:

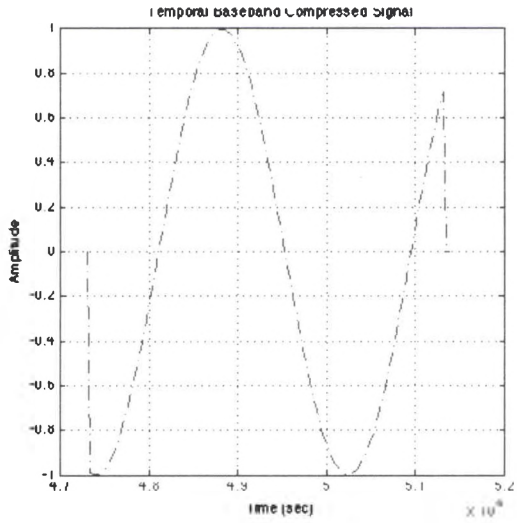

Figure 17: Pulse-Compressed Echo Delay Signal for T2

As alluded to earlier, but plainly visible now, the pulsed compressed signal has a sinusoid of fundamental frequency corresponding to the echo time-delay from the target to the airborne platform. Since the pulse compression is referenced to range swath center (RSC), the Doppler frequency is only dependent upon the +1 meter difference in range location. The HRR profile from this target point is:

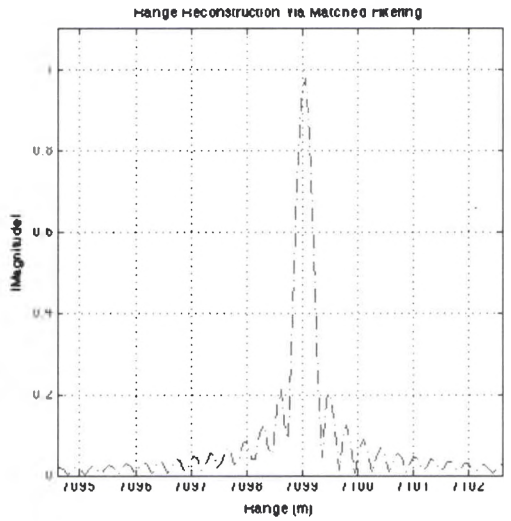

Figure 18: HRR Profile for T2

As expected, the HRR profile is still the magnitude of the *sinc* function, but whose peak is shifted to the appropriate range. Now, a single ideal point scatterer will be placed 0.3 meter from RSC, but this time closer to the airborne platform. In a similar vein to the previous example, a sinusoid corresponding to the echo time-delay is expected. Though the resultant HRR profile should have a peak shifted to the left of the RSC target point.

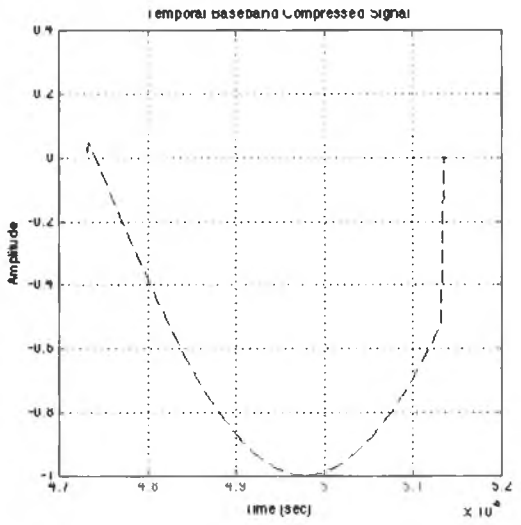

Figure 19: Pulse-Compressed Echo-Delay Signal from T3

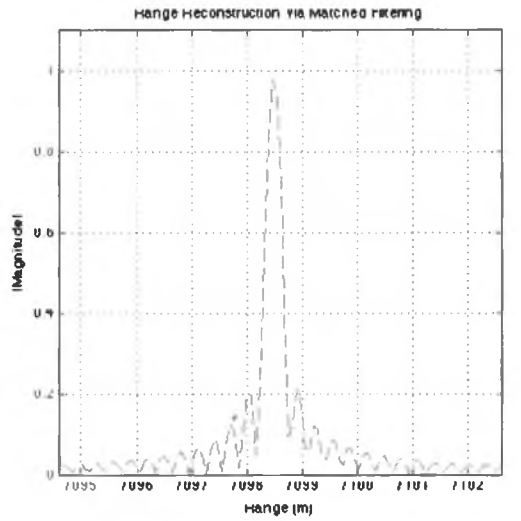

Figure 20: HRR Profile for T3

The assumptions on both the structure of the pulse compressed signal and the HRR profile were valid. One way to put each of these three results into perspective is to display them all on one single plot. To make this more interesting as an exercise, there will be a fourth line plot of the sum of all three individual target scatterers. This fourth line will be denoted by asterisks and

simulates what the radar response would be after pulse compression in an actual scenario.

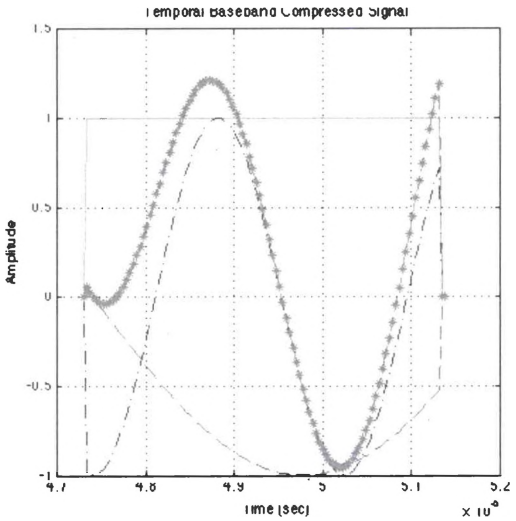

Figure 21: Composite of All Target Pulse-Compressed Echo-Delay Returns

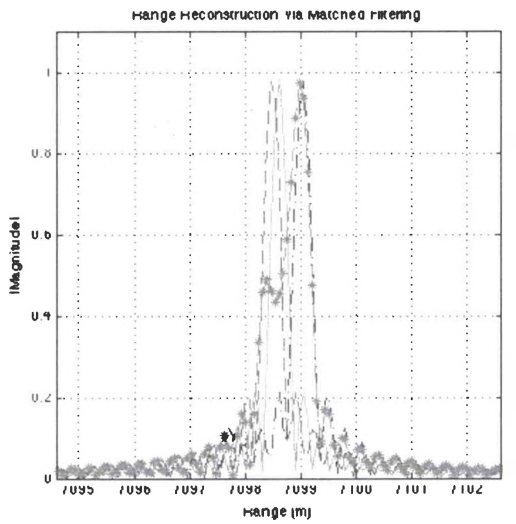

Figure 22: Composite HRR Profile for All Targets

By removing all by the fourth line, representing the sum of all individual target returns, the HRR profile resulting from illumination of a range swath containing three targets is found.

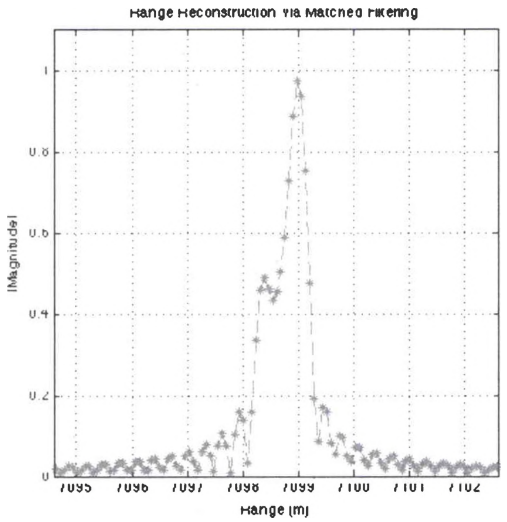

Figure 23: Sum of All Three Target Returns HRR Profile

The HRR profile does have three distinct peaks, but in relation to the scale of the composite plot line, appears to have only one dominant and one minor peak. This is an interesting observation since the point scatterers were placed in three distinct ranges. Figure 8 extends +/- 10 meters from range swath center. The composite plot line, being a summation of each of the three individual contributors, exhibits effects arising the constructive and destructive interference from each echo-delay return. This is mainly due to the location and weighting of the quantized samples of the received signals.

The pulse-compressed signal was introduced along with the corresponding HRR profile for the case of three individual point scatterers distributed in range. Additionally, the sampling space was shown and referenced to the range swath center point target.

Section 2.8-Testing for Targets in Cross-Range

Having examined the case of point targets extended in range, let us consider targets lying in a single range bin, but distributed in cross-range. Just as before, the plots will show the radar response for each of the three point scatters present alone and also when they are simultaneously present. Figure 24 will be a helpful reference for this section.

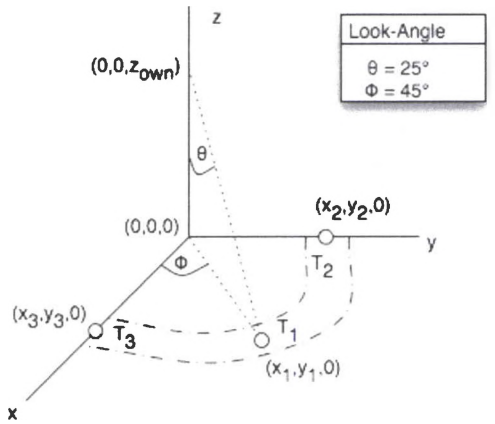

Figure 24: Three Targets in a Single Isorange Annular Ring

This represents the highly unlikely scenario where targets are well separated in the cross-range of the isorange annular range swath. While unrealistic, this aids in visualizing the effect targets have on the HRR profile when colocated in range. Table 3 contains information on each of the three targets in figure 25.

Table 3: Cross-Range Target Information

	Platform	Target		
	ϕ=45°, θ=25°	T1	T2	T3
Reflectivity	NA	1	1	1
x-location	0 m	2.1213 km	0 km	3.000 km
y-location	0 m	2.1213 km	3.000 km	0 km
z-location	6.4345 km	0 m	0 m	0 m
R_{los}	NA	7.0986 km	7.0986 km	7.0986 km

Immediately evident from table 3 is that each of the three targets are the same line-of-sight distance from the airborne platform. Plotting all three target returns, in addition to the summation of all three echo-delay returns gives:

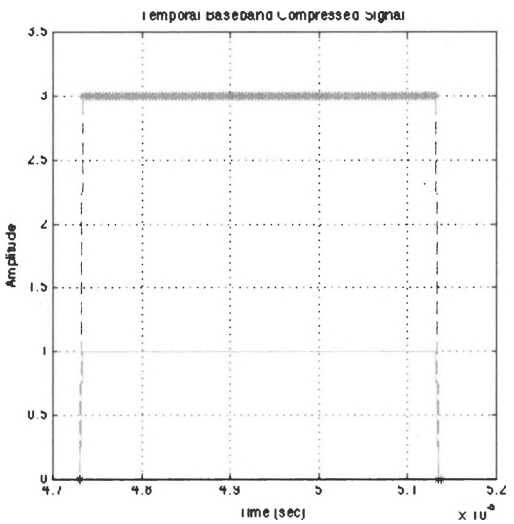

Figure 25: Composite of Pulse-Compressed Echo-Delay Returns for Targets Co-located Cross-Range

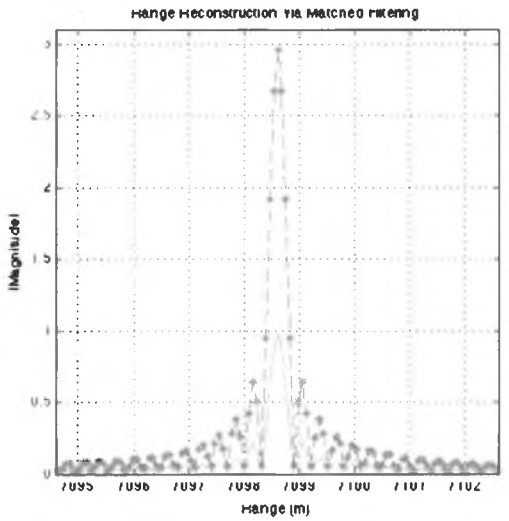

Figure 26: Composite HRR Profile for Targets Co-located in Cross-Range

The results of figure 25 and 26 were expected. Even though their relative locations in the range swath are different, since they are located within a single range bin, all their echo time-delay returns are the same. Thus, the HRR profile is just the matched filter and inverse Fourier transformed reflectivity scaled by the number of point targets located within the isorange space.

Section 2.9-Testing for Extended Targets Uniformly Distributed

Section 2.8 covered the scenarios for targets extended in range and cross-range independently. This section will highlight the scenario where targets are distributed in range and cross-range uniformly: representing the case of an actual extended target in the range swath space. The target points are randomly chosen and exhibit a uniform distribution. For this simulation, target information is given by table 4.

Table 4: Scenario Information for Multiple Uniformly Distributed Targets

	Platform	Ideal Point Targets
Total Number	1	25
Distribution	Fixed	Uniform
Range of Distribution	Fixed	$-5\text{ m} \leq x \leq 5\text{ m}$ $-5\text{ m} \leq y \leq 5\text{ m}$
Reflectivity	NA	1

Section 2.10-Conclusions

In this chapter the high-range resolution (HRR) algorithm was introduced through the use of the linear-frequency modulated (LFM) waveform. More importantly, the concept of the target reflectivity profile frames the creation of the HRR profile as an imaging problem, in which the image is created by the constructive and destructive interference of point-spread functions; the point-spread function being dependent upon the individual point target positions in relation to the airborne radar platform. The coordinate space model utilized for the formation of the own and target model line-of-sight vector synthesis, in addition to, the effects of range and velocity on the LFM waveform were discussed. Finally, the HRR algorithm was explained in conjunction with a zero radial velocity ideal target model; verification of this method under a series of waveform and scenario constraints confirmed the proper formation of the HRR profile in an experimental setting.

CHAPTER 3

HRR INTERFERENCE PHENOMENA

AND

TESTING METHODOLOGY OVERVIEW

Section 3.1-Introduction HRR Interference Phenomena

Critical to the understanding of the HRR profile is the basis for its creation: the target of interest. Target is a general term and can refer to anything from a vehicle or building, to an aircraft or spacecraft. For our purpose, the target is assumed to be a single subject of interest, comprised of multiple scattering centers. Each scattering center is modeled as an ideal point target (IPT), which is to say, a perfect sphere of infinitesimal radius. The IPT, when illuminated by a high range resolution (HRR) sensor waveform reradiates isotropically.

In addition to the reradiated waveform following impact with a given target IPT, there are three other common sources of backscattered energy. Since these sources of energy could possibly mask or obscure the target signature process, they are not considered in this work. The first of these spurious backscattered energy sources is that of clutter; clutter returns result from the transmit waveform impinging on the surface of the earth-ground, forests, water-

and scintillating in all directions. Clutter returns are highly random in nature and difficult to account for in the study of HRR subspace. Therefore, the study will be conducted exoclutter. An actual HRR sensor would not radiate isotropically, but would have an associated directivity to narrow the focus of the transmit, or mainlobe, beam to focus on a finite range swath. By introducing directivity, sidelobes, not associated with the mainlobe beam, are formed [2]. These sidelobes radiate in many directions and give rise to returns of their own. A great deal of effort goes into reduction or mitigation of sidelobes in the preliminary radar design phase. Since they are troublesome to model and account for, sidelobe effects are ignored. Lastly, in terms of the HRR sensor, thermal and hardware phenomena will be ignored. Noise resulting from the HRR sensor hardware systems, as well as, from thermal sources introduce a randomness that would be problematic to account for.

A rather important consideration for simplification of the interference effect study is the use of planar target structures in two-dimensional space. The reason for this is due to the ambiguity arising from a three-dimensional structure. Such a target would introduce shadowing effects that would limit the ability to study the interference phenomena without due consideration to multipath effects. Thus, consideration of the range space is now undertaken.

Extending these results to the concept of an HRR radar system signal processing back-end, the range swath under illumination from the transmit waveform is divided into separate range spaces. These range spaces are called

range bins; or for the case of a transmit beamwidth of equal azimuthal and elevation extent, isorange bins (see Figure 27). An extended target structure comprised of ideal point scatterers will populate multiple range bins in what are called the range and cross-range.

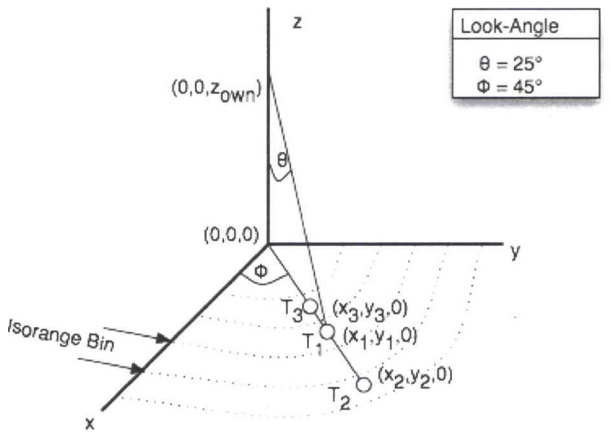

Figure 27: Generalized Extended Point Target Model

Range bins are determined from the round-trip delay time of the reflected waveform; while cross-range locations within a given isorange bin contribute to the interference phenomena under investigation.

An investigation of the HRR subspace will aid in the explanation of how the target, or targets, occupying a given range swath will affect the HRR profile. The range swath of interest is that ground area that is observable by the airborne platform: this range swath may also be called the coverage area of the radar mainbeam. This area is finite in extent and is defined by a pair of orthogonal axis. From geometric principles, these axis are labeled the minor and major axis: thereby representing an ellipse. In the field of radar, these axis are called the

range and cross-range. The range swath area is found from the platform height, azimuth angle, azimuth 3dB beamwidth angle, elevation angle, and elevation 3dB beamwidth angle. The figure below illustrates this relationship.

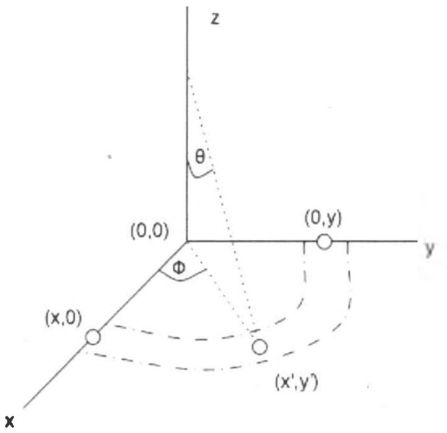

Figure 28: Generalized Representation of a Single Iso-Range Bin

The target range is defined in two ways: as the x-y coordinates on a global Cartesian reference coordinate system, or as the line-of-sight range. The line-of-sight (LOS) range is what the radar captures upon illumination with the mainbeam. The global reference coordinate system is a simplified manner of defining the target locations within the range swath of interest. Generally, the point on the ground under the platform is defined as the global original. The range is defined as being perpendicular with the platform look-angle, in this reference coordinate system. Due to the curvature of the range space, the cross-range is actually a series of arcs parallel to the platform look-angle. Based on the range resolution of the radar waveform, these arcs represent planar annular regions [12]. The annular regions can also be labeled isorange bands, or rings.

Each isorange band, for the case of a perfectly symmetric ellipse, is a singular LOS distance to the platform. Therefore, any and all targets lying within this band will appear as one target to the radar. For the case of an ellipse, there are only two points on each isorange band that will be the same LOS to the radar. As the elevation angle approaches 90°, the ellipses collapse into straight lines. This would mean targets in the cross-range would lie on a straight line parallel to the platform look-angle. Planar geometry is one way straight-line approximations of target points could be made to fill specified LOS range bins. For the practical case of annular range bins, the following formula is useful,

$$(x', y') = (\cos(\theta), \sin(\theta)) \odot (x, y), \tag{3.1}$$

with the $\odot$ symbol denoting the Hadamard product. This formula only applies to the circular isorange band case. In order to find the elliptical coordinate transformation, the following mapping function is used,

$$(x', y') = \left(\frac{a\cos(\theta)}{\sqrt{a^2\cos^2(\theta) + b^2\sin^2(\theta)}}, \frac{b\sin(\theta)}{\sqrt{a^2\cos^2(\theta) + b^2\sin^2(\theta)}} \right) \odot (x, y). \tag{3.2}$$

Solving for the ellipse semiminor axis, b, and semimajor axis, a,

$$2b = 2R_{LOS} \tan\left(\frac{\varphi_{AZ}}{2}\right), \tag{3.3}$$

and semimajor axis, a,

$$2a = 2R_{LOS} \tan\left(\frac{\varphi_{EL}}{2}\right) \csc(90 - \theta), \tag{3.4}$$

where φ_{AZ} and φ_{EL} are the 3 dB mainbeam beamwidths in azimuth and elevation, respectively. Most realized radar systems have antenna 3dB beamwidths that are as narrow as a few degrees in both azimuth and elevation

[18]. This would cover an extremely large range swath and require large amounts of processing and storage capability. Instead, we take the approach that the range swath of interest is less than the total observed range swath. Therefore, an assumption can be made that the target(s) are within only a small region of the observed range swath space and adhere to the assumption of circular annular range bins, thereby making 3.11 appropriate. Arguably, this is a heuristic assumption, but one that simplifies further calculations.

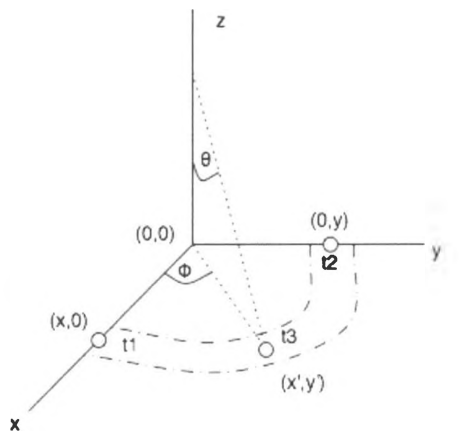

Figure 29: Idealized Point Targets Arranged in Cross-Range

Figure 29 shows a typical arrangement of targets aligned in cross-range following the annular isorange bin formula of 3.11. The vector modulus of each target is identical, $\| t1 \| = \| t2 \| = \| t3 \|$, with respect to the origin. From the discussion prior, the LOS range to the platform should be identical for each of the three target coordinates. In order to illustrate this point, and to analyze the differences arising from range and cross-range target location, a routine was created in

Matlab. The purpose of this program was to investigate the various effects that comprise an actual HRR profile.

Section 3.2-Description of Testing Methodology

The proceeding chapter will detail the results of the testing methodology that is presently presented for explanation of purpose. Initially, the concept of the target signature is introduced, followed by the formation of a complete high-range resolution signature for a generic target model utilizing a full linear frequency modulated (LFM) waveform. Following the creation of the full LFM HRR signature, the range bin statistics responsible for the profile of the signature is detailed. The purpose of the investigation of the statistical properties of the range bin is to demonstrate characteristic quirks that comprise the data point residing in the range bin corresponding to a point on the HRR profile, and subsequent signature. To conclude the introductory testing scheme, X-Patch scattering center data is used to provide target truth and operational validity of the LFM HRR algorithm.

After introduction and verification of the LFM HRR algorithm and signature generating capabilities, a generic idealized point scattering model is introduced. This model will provide the framework for the remainder of the HRR interference phenomena investigation. The first of these investigations centers on a uniform ideal point target model with perfect reflectivity. This, being the ideal case, will give the baseline HRR signature for the generalized two-dimensional target

model. A second phenomenological study on the angular selectivity and subsequent frequency selectivity of multiple target scatterers is conducted. The results of the selectivity of target structures on the appearance of the HRR signature is detailed. To eliminate the singular heuristic scope of the interference phenomena investigation, the signal subspace of the HRR profile is examined and the results of the previously listed selectivity examples compared against the idealized uniform extended point target case.

Section 3.3-Summary Remarks

In this chapter, the concept of high-range resolution (HRR) interference was introduced in a traditional framework. Brief explanations of the testing methodology and relative significance were discussed. Chapter 4 introduces the theory of the interference phenomena in greater detail and provides explanatory remarks, in conjunction with, theoretical concepts to expound upon the summary presented in section 3.2.

CHAPTER 4

HRR INTERFERENCE PHENOMENOLOGY TESTING RESULTS

Section 4.1-Introduction to Target Signatures

From chapter 2 the high-range resolution profile was found to be a weighted coherent sum of point-spread functions corresponding to the effective range delay of scattering centers comprising a complex target. Chapter 3 introduced the concept of the interference phenomena arising from targets lying within a single range bin but widely spaced in cross range. The investigations presented in this chapter seek to illuminate the formation of the HRR signature of a complex target for any given transmit waveform, in general, and an LFM waveform in particular. It is of particular interest to determine the relationship, if any, between the "features" of a HRR signature, typically the strength and location of the peaks, and the scattering phenomena associated with the physical features of the target. That is, the goal is to determine the link, if any, that may exist between the "features" in the signature and the physical features on the target.

The specified target is modeled as collection of point scatterers distributed in a plane for a given look angle. Such decomposition may be obtained from the scattering data generated by electromagnetic prediction codes. Starting with such a data set the HRR signature corresponding to an LFM radar waveform has been determined. In addition, a number of numerical experiments have been conducted to assess the effect of spatial and temporal selectivities of the scattering from the scattering centers on the signature "features" as well as on the decomposition of the signature data space into signal and "noise" subspaces.

Section 4.2-Verification of LFM Signature Representation Using X-Patch Generated Data

The operation of the high-range resolution (HRR) algorithm is verified through the use of X-Patch (see figure 35) [1] and HRR signature comparison to ensure the validity of results presented throughout the remainder of this chapter. The model utilized, created in X-Patch (see figure 35), provides coordinate, as well as, magnitude and phase information on the target frequency response. Since this information is in the frequency domain, the received signal is modified with the inverse Fourier transform of the X-Patch frequency response data. Figure 30 shows the location of the scattering centers.

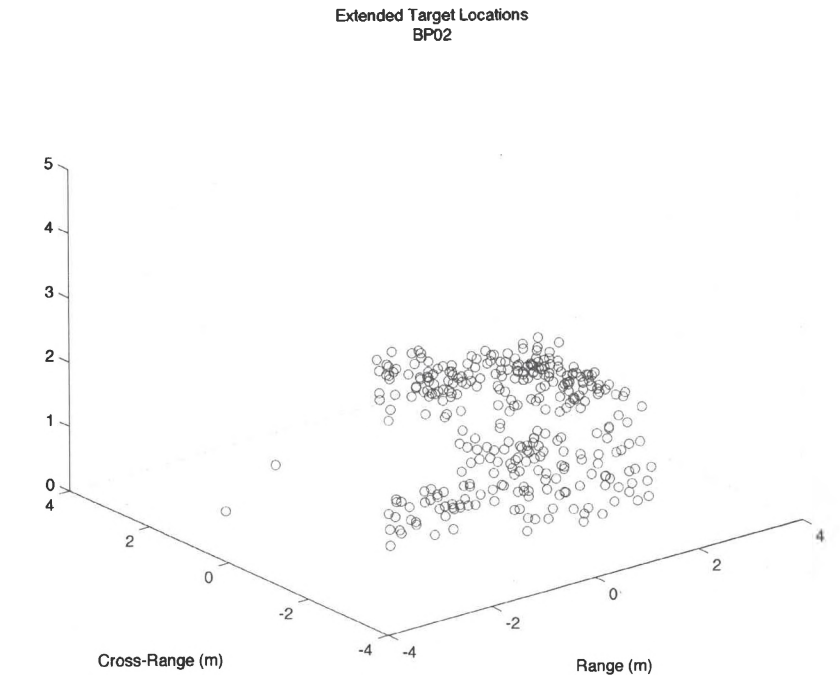

Figure 30: X-Patch BMP-2 Target Scatterer Locations

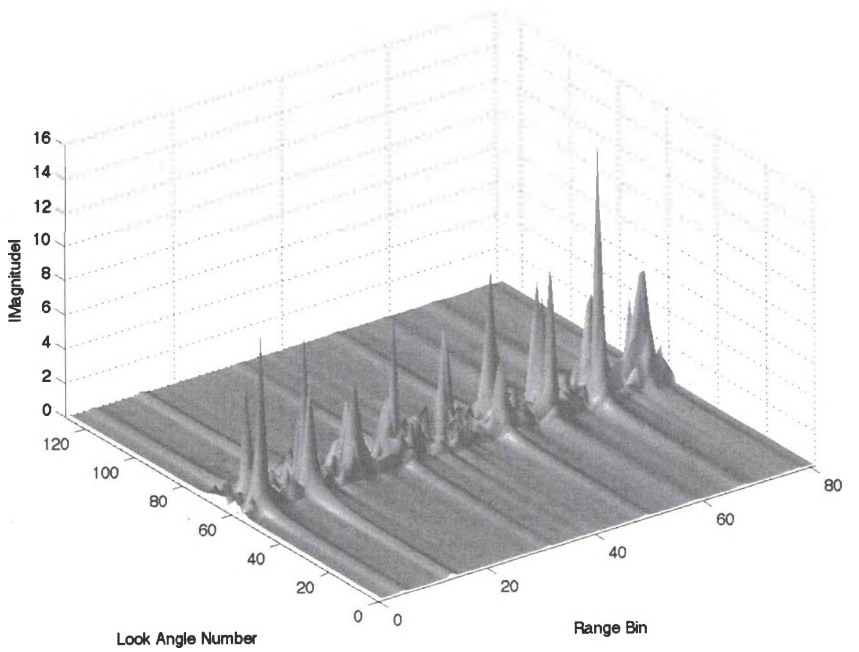

Figure 31: X-Patch BMP-2 Tank Signature

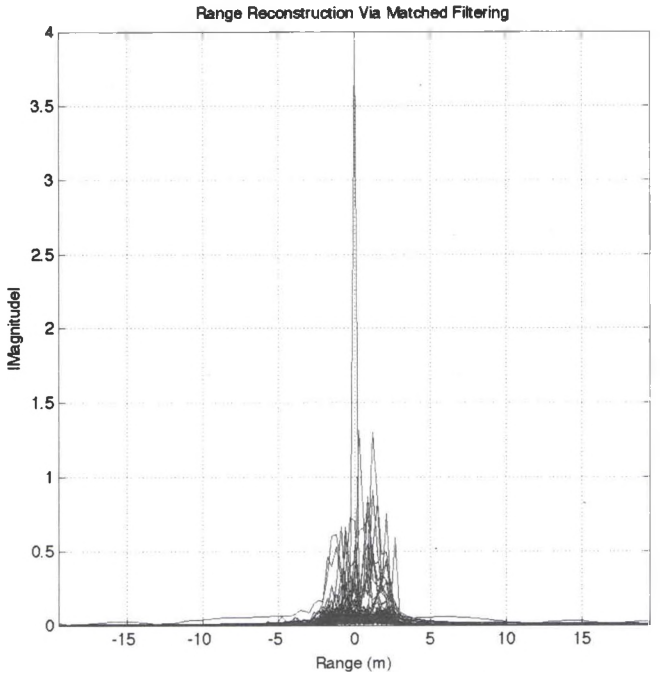

Figure 32: LFM Derived HRR Signature of BMP-2

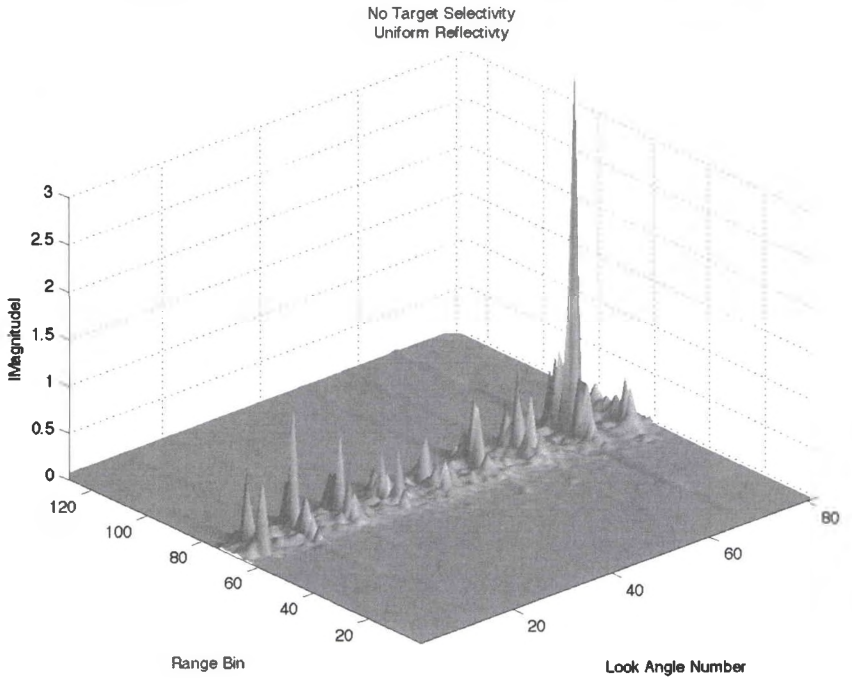

Figure 33: LFM Derived HRR Signature of BMP-2

Section 4.3-Creation of Full LFM Signature

While real-world data (i.e.-X-Patch) is perfectly valid for the remainder of the interference phenomenology study, a three-dimensional structure imposes serious limits on the understanding that target characteristics have on the resultant high-range resolution (HRR) signature. This is due to the inherent shadowing effects that manifest as a result of the three-dimensional target shape. Additionally, edge diffraction and higher-order effects introduce an aire of ambiguity to the HRR signature. Effective mitigation of these said effects is accomplished through the use of a two-dimensional target structure, extended in range and at the same altitude. The "planar" geometry of the extended structure permits easy manipulation of the reflectivity profile while maintaining a relatively pristine testing environment in which to gauge the various selectivity characteristics of the target scatterers.

For the remainder of the study the number of ideal point targets arranged in the range swath under illumination is approximately one-hundred and ten (110). As these point scatterers are uniformly distributed within the given range space, the range bin statistics are valid (see section 4.4) and hence, preserve the information content of the processed signature.

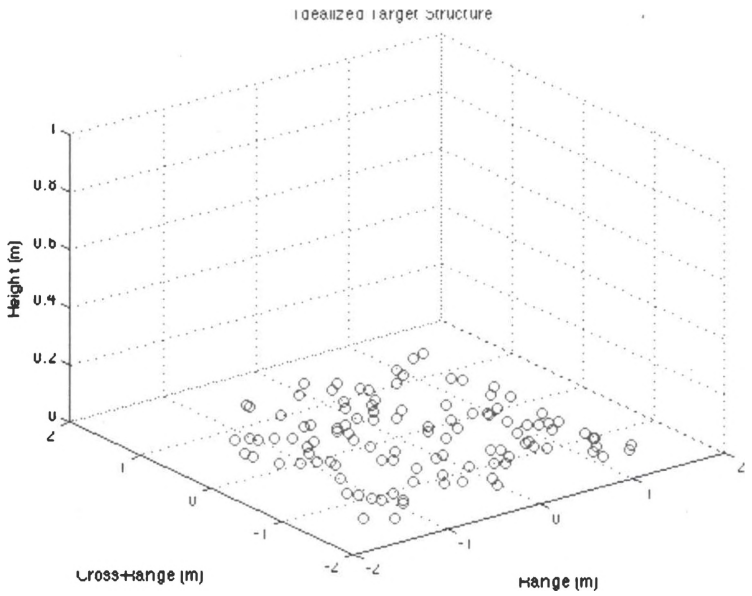

Figure 34: Idealized Target Model

The resolution of the radar is 0.3048 meters (Table 1) and there are eleven (11) range bins covering the range swath from +/-1.524 meters from range swath center, in both range and cross-range. The height of each ideal point scatterer is zero. Thus, a uniform target model with no shadowing or higher-order effects has been successfully created for use in the remainder of the phenomenology study.

All previous chapters detailed the creation of the high-range resolution (HRR) profile as being the reflectivity profile resulting from illumination of some target model with a transmit waveform. For a thorough understanding of the dynamics that arise from varying pose and look-angles in relation to own/target positions, a different empirical framework is now introduced.

If a HRR profile for a series of look-angles are preserved and viewed together, then the result is the HRR signature. The signature is merely a collection of look-angles over which a target is viewed from a standard pose angle. Taking figure 35 to represent the X-Patch Russian BMP-2 tank model, the pose angle would be reference to a particular structural element inherent in the target structure. In this case, let the reference element be the right tank tread. Since the turret is free to move relative to the reference element, the pose angle would not change as a result of turret movement. However, if the tank model were to

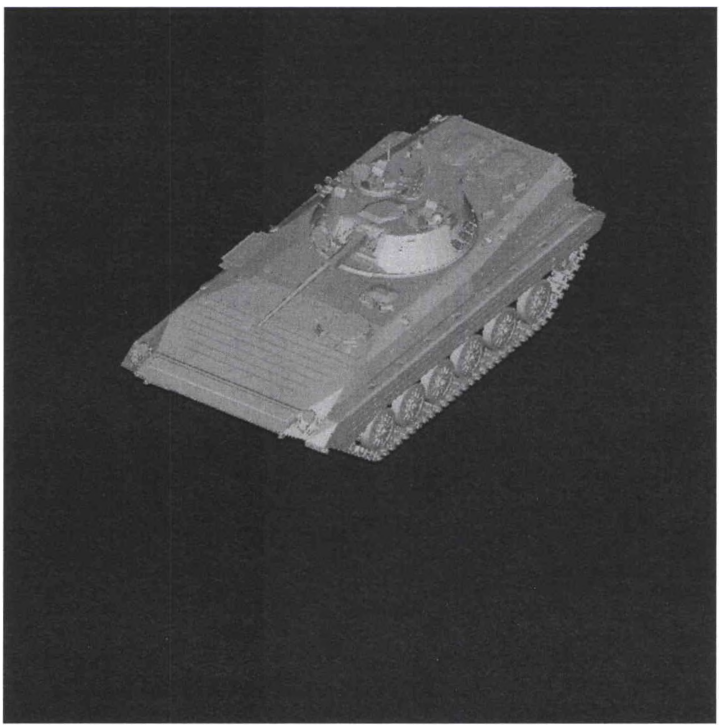

Figure 35: X-Patch Russian BMP-2 Tank Model

turn left or right, then the pose angle of the target has varied, and hence any imaging profile resulting from target illumination would, also, be different.

Having created a synthetic target structure, the corresponding high-range resolution (HRR) signature is found. Initially, the target structure will have an ideal reflectivity of one. Obviously, the amplitude of the echo is perfect and does not represent a real target structure. However, the reflectivity profile of the target structure is investigated in section 4.5. For the case presented, the target structure is viewed over the entire look-window. The overlay of the individual HRR profiles for the control is shown in figure 36.

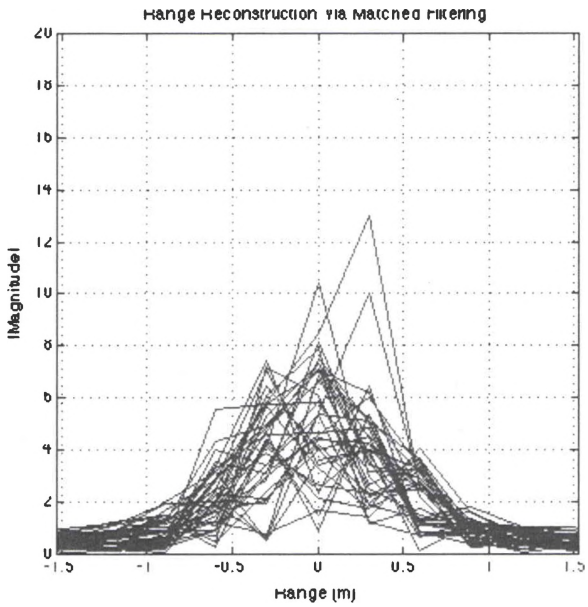

Figure 36: HRR Signature of Idealized Target Model

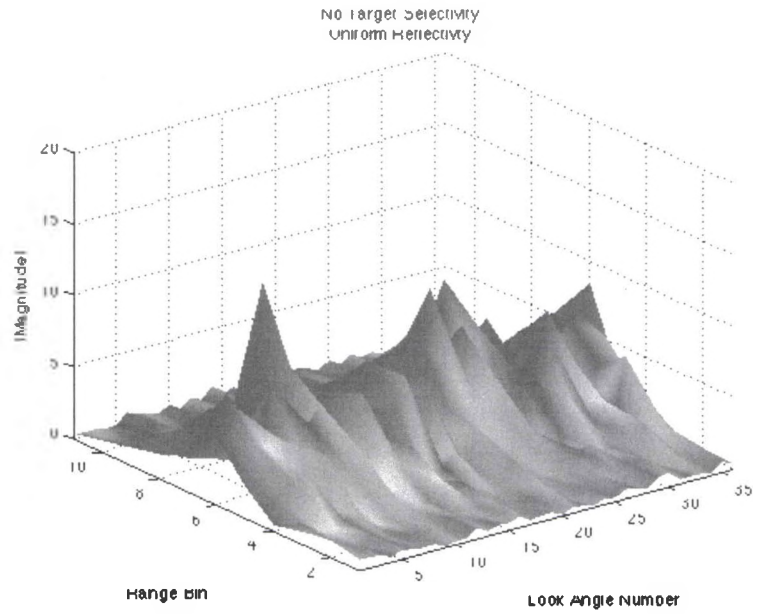

Figure 37: HRR Signature of Idealized Target Model

These signatures were viewed over a given range of look angles. The look window defines this range and is +/-2.5° for the initial look angle of 45° in azimuth and 25° in elevation. This look window is not uniform and is done so purposely to avoid ambiguities that arise when the look angle is the same value as the initial look angle. This will become important more so when dealing with angularly selective target structures; where a look angle equal to the initial look angle will result in an invalid number, or in Matlab NaN (Not a Number).

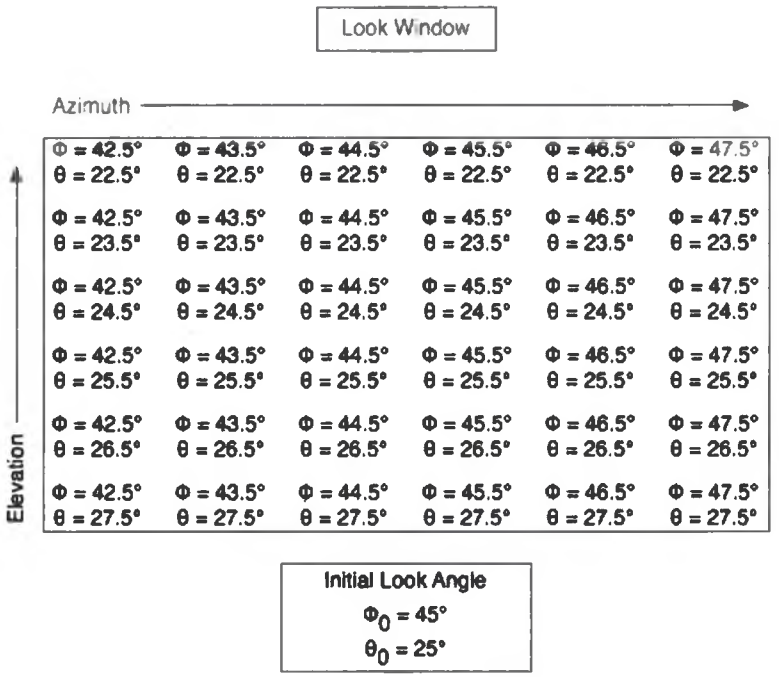

Figure 38: Look Window Utilized for Testing

The total number of look angles is thirty-six (36). This allows for efficient code execution, in addition to minimizing the computational complexity of calculating the signal subspace via eigen decomposition.

Section 4.4-Statistical Analysis of the Received Signal Representation

The received signal from a single ideal point target is modeled by the voltage function [3],

$$Ae^{j\phi}. \tag{4.1}$$

For an extended target structure comprised of a multitude of target discretes, all exhibiting ideal characteristics, 4.1 becomes [3],

$$V = \sum_{n=1}^{N} A_n e^{j\phi_n} \quad . \tag{4.2}$$

By viewing 4.2 as the echo signal voltage function, in Polar format, 4.2 is easily transformed into the Cartesian coordinate using the following transformation [3],

$$V = X + jY \, . \tag{4.3}$$

The real component of 4.3 is defined by the expression,

$$X = V\cos(\phi) = \sum_{n=1}^{N} A_n \cos(\phi_n) = \sum_{n=1}^{N} X_n \, , \tag{4.4}$$

and the corresponding imaginary expression of 4.3 is,

$$Y = V\sin(\phi) = \sum_{n=1}^{N} A_n \sin(\phi_n) = \sum_{n=1}^{N} Y_n \, , \tag{4.5}$$

Together, 4.4 and 4.5 represent the received signal in rectangular form. X and Y are independent identically distributed (i.i.d.) random variables [3]. Solving for the mean of X and Y yields,

$$E\{X_n\} = E\{A_n \cos(\phi_n)\} \, , \tag{4.6}$$

and

$$E\{Y_n\} = E\{A_n \sin(\phi_n)\} \, , \tag{4.7}$$

respectively. Since X and Y are i.i.d. random variables, they are also separable, leading to,

$$E\{X_n\} = E\{A_n\} E\{\cos(\phi)\} \, , \tag{4.8}$$

and

$$E\{Y_n\} = E\{A_n\} E\{\sin(\phi)\} \, . \tag{4.9}$$

We know that the mean of a sinusoidal function is zero, further yielding,

$$E\{X_n\} = \mu_A \cdot 0 = 0 \tag{4.10}$$

and

$$E\{Y_n\} = \mu_A \cdot 0 = 0. \tag{4.11}$$

Therefore the expected value, or mean, of the amplitude distribution is zero. The variance of X and Y are given by,

$$Var\{X_n\} = \sigma_{X_n} = E\left\{A_n^2 \cos(\phi_n)^2\right\}, \tag{4.12}$$

and

$$Var\{Y_n\} = \sigma_{Y_n} = E\left\{A_n^2 \sin(\phi_n)^2\right\}. \tag{4.13}$$

Using the i.i.d. property, the variance is given as,

$$Var\{X_n\} = E\{A_n - \mu_A\}^2 E\{\cos(\phi_n) - \mu_A\}^2. \tag{4.14}$$

Completing the square leads to,

$$Var\{X_n\} = E\{A_n^2\} - (E\{A_n\})^2 + E\left\{\cos(\phi_n)^2\right\} - \left(E\{\cos(\phi_n)\}\right)^2. \tag{4.15}$$

Utilizing 4.10 and 4.12, 4.15 becomes,

$$Var\{X_n\} = \sigma_A^2 - \mu_A^2 + \sigma_A^2. \tag{4.16}$$

Combining like terms,

$$Var\{X_n\} = 2\sigma_A^2 - \mu_A^2. \tag{4.17}$$

Simplification of 4.17 gives the final form of the variance of X,

$$Var\{X_n\} = \frac{\sigma_A^2 - \mu_A^2}{2}. \tag{4.18}$$

Likewise, using the i.i.d. property, the variance of Y is given by,

$$Var\{Y_n\} = E\{A_n - \mu_A\}^2 E\{\sin(\phi_n) - \mu_A\}^2 . \tag{4.19}$$

Completing the square gives the same result as 4.15,

$$Var\{Y_n\} = E\{A_n^2\} - (E\{A_n\})^2 + E\{\sin(\phi_n)^2\} - (E\{\sin(\phi_n)\})^2 . \tag{4.20}$$

Simplification of 4.20 gives,

$$Var\{Y_n\} = \sigma_A^2 - \mu_A^2 + \sigma_A^2 . \tag{4.21}$$

Combining like terms and simplifying yields the final form of the variance of Y,

$$Var\{Y_n\} = 2\sigma_A^2 - \mu_A^2 , \tag{4.22}$$

$$Var\{Y_n\} = \frac{\sigma_A^2 - \mu_A^2}{2} . \tag{4.23}$$

Given the assumption that the random variables are independent identically distributed, we can prove by the central limit theorem that if X_n is a random sample of size *n*, from a population with mean μ and variance σ^2, and if $\bar{X}$ is the sample mean, then the limiting form of the distribution is [15],

$$\mathbb{Z} = \frac{n\bar{X}_n - n\mu}{\sigma\sqrt{n}} . \tag{4.24}$$

Where 4.24 becomes

$$N(0,1), \tag{4.25}$$

as $n \to \infty$. Application of 4.24 to the i.i.d. random variables X and Y yields [15],

$$X = \sum_{n=1}^{N} X_n, \quad Z_X = \frac{n\sum_{n=1}^{N} X_n - n\mu}{\sigma\sqrt{n}}, \tag{4.26}$$

and,

$$Y = \sum_{n=1}^{N} Y_n, \quad Z_X = \frac{n\sum_{n=1}^{N} Y_n - n\mu}{\sigma\sqrt{n}}, \tag{4.27}$$

respectively. Assume that n is large, but not necessarily ∞, $1 << n << \infty$. Then using the central limit theorem, the mean is 0 and the variance is given by,

$$\sigma_{X,Y}^2 = \left(\sqrt{n}\sigma\right)^2. \tag{4.28}$$

Simplification of 4.28 and application of the variance definition yields,

$$\sigma_{X,Y}^2 = n\sigma^2, \tag{4.29}$$

and,

$$\sigma_{X,Y}^2 = n\left(\frac{\sigma_A^2 - \mu_A^2}{2}\right). \tag{4.30}$$

Given that as $\mathbb{Z} \to \infty$ we have,

$$f_Z(Z) \to \frac{1}{\sqrt{2\pi}} e^{-Z^2/2}, \tag{4.31}$$

which is the standard $N(0,1)$ case of the general normal distribution,

$$f_Z(Z) \to \frac{1}{\sigma\sqrt{2\pi}} e^{-(Z-\mu)^2/2\sigma^2}. \tag{4.32}$$

Substituting for the case of X and Y, we have the following mean,

$$E(X) = 0, \tag{4.33}$$

and variance,

$$E(X) = \frac{n\left(\sigma_A^2 + \mu_A^2\right)}{2}. \tag{4.34}$$

Substitution of 4.33 and 4.34 into the generalized normal distribution function yields,

$$f_X(X) = \frac{1}{\sigma\sqrt{2\pi}} e^{-X^2/n\left(\sigma_A^2+\mu_A^2\right)}, \tag{4.35}$$

for X and,

$$f_Y(Y) = \frac{1}{\sigma\sqrt{2\pi}} e^{-Y^2/n\left(\sigma_A^2+\mu_A^2\right)}, \tag{4.36}$$

for random variable Y. Solving for their joint first and second moments, we have,

$$E\{XY\} = \left(\sum_{n=1}^{N} X_n \sum_{m=1}^{M} Y_m\right). \tag{4.37}$$

Substituting 4.6 and 4.7 into 4.37 gives,

$$E\{XY\} = E\left\{\sum_{n=1}^{N}\sum_{m=1}^{M} A_n A_m \cos(\phi_n)\sin(\phi_m)\right\}. \tag{4.38}$$

From the i.i.d. assumption and removing the summation outside of the expected value expression, 4.38 becomes,

$$E\{XY\} = \sum_{n=1}^{N}\sum_{m=1}^{M} E\{A_n A_m\} E\{\cos(\phi_n)\sin(\phi_m)\}. \tag{4.39}$$

Integrating over the full range of possible angles for phi, $E\{\cos(\phi_n)\sin(\phi_m)\}$ for the case of $n \neq m$ is,

$$E\{\cos(\phi_n)\sin(\phi_m)\} = \int_0^{2\pi}\int_0^{2\pi} \cos(\phi_n)\sin(\phi_m)\, d\phi_n d\phi_m, \tag{4.40}$$

and for $n = m$, 4.40 turns into,

$$E\{\cos(\phi_n)\sin(\phi_n)\} = \int_0^{2\pi} \cos(\phi_n)\sin(\phi_n)\, d\phi_n. \tag{4.41}$$

We know that,

$$E\{X\}E\{Y\} = 0. \tag{4.42}$$

If two random variables are independent, such that

$$f_{XY}(X,Y) = f_X(X) f_Y(Y). \tag{4.43}$$

Then since $E\{XY\} = E\{X\}E\{Y\}$, X and Y are uncorrelated. Proof:

$$E\{XY\} = \int_0^\infty \int_0^\infty XY f_X(X) f_Y(Y) dX dY, \tag{4.44}$$

then,

$$E\{XY\} = X f_X(X) dX \int_0^\infty Y f_Y(Y) dY \text{ . QED} \tag{4.45}$$

Hence,

$$E\{XY\} = E\{X\}E\{Y\}. \tag{4.46}$$

For normal random variables, uncorrelatedness corresponds to a covariance coefficient of 0, and thus independence,

$$Cov(XY) = E\{XY\} - E\{X\}E\{Y\} = 0. \tag{4.47}$$

So, given that the rectangular form of the voltage expression is,

$$Ve^{j\phi} = X + jY \ . \tag{4.48}$$

Therefore, solving in terms of V and ϕ, we define,

$$V = \sqrt{X^2 + Y^2} \tag{4.49}$$

and

$$\phi = \tan^{-1}\left(X/Y\right). \tag{4.50}$$

We can obtain the joint density function of 4.49 and 4.50 by application of the Jacobian, hence,

$$f_{XY}(X,Y)=\frac{1}{2\pi\sigma^2}e^{-(X^2+Y^2)/\sigma^2}. \tag{4.51}$$

Since,

$$V=g(X,Y)=\sqrt{X^2+Y^2} \tag{4.52}$$

and

$$\phi=h(X,Y)=\tan^{-1}\left(X/Y\right), \tag{4.53}$$

with ϕ varying from $(0,2\pi)$, there is a single solution pair for 4.52 and 4.53,

$$X=V\cos(\phi) \tag{4.54}$$

and

$$Y=V\sin(\phi). \tag{4.55}$$

The resultant Jacobian expression is,

$$J(r,\phi)=\begin{vmatrix}\frac{\partial X}{\partial V} & \frac{\partial X}{\partial \phi}\\ \frac{\partial Y}{\partial V} & \frac{\partial Y}{\partial \phi}\end{vmatrix}. \tag{4.56}$$

Substitution of 4.54 and 4.55 into 4.56 gives,

$$J(r,\phi)=\begin{vmatrix}\cos(\phi) & -r\sin(\phi)\\ \sin(\phi) & r\cos(\phi)\end{vmatrix}. \tag{4.57}$$

The determinant of 4.57 is thus,

$$J(r,\phi)=V. \tag{4.58}$$

We can then solve for the transform Jacobian,

$$J(X,Y)=\begin{vmatrix} \frac{\partial g}{\partial X} & \frac{\partial g}{\partial X} \\ \frac{\partial h}{\partial Y} & \frac{\partial h}{\partial Y} \end{vmatrix}. \tag{4.59}$$

Substitution of 4.52 and 4.53 results in,

$$J(X,Y)=\begin{vmatrix} \frac{X}{\sqrt{X^2+Y^2}} & \frac{Y}{\sqrt{X^2+Y^2}} \\ \frac{-Y}{\sqrt{X^2+Y^2}} & \frac{X}{\sqrt{X^2+Y^2}} \end{vmatrix}, \tag{4.60}$$

whose determinant is,

$$J(X,Y)=\frac{1}{\sqrt{X^2+Y^2}}, \tag{4.61}$$

which then simplifies to,

$$J(X,Y)=\frac{1}{V}. \tag{4.62}$$

The Jacobian pair for both the cylindrical and rectangular form is therefore,

$$\left|J(r,\phi)\right|=\left|\frac{1}{J(X,Y)}\right|. \tag{4.63}$$

Substituting 4.51, 4.54, 4.55 into 4.58 and 4.62 yields,

$$_{V\phi}(V,\phi)=Vf_{XY}=\frac{V}{2\pi\sigma^2}e^{-V^2/2\sigma^2}, \tag{4.64}$$

where $0<V<\infty$ and $0<\phi<2\pi$. Thus,

$$f_V(V)=\int_0^{2\pi} f_{V\phi}(V,\phi)d\phi=\frac{V}{2\pi\sigma^2}e^{-V^2/2\sigma^2}. \tag{4.65}$$

This represents a Rayleigh random variable with parameter σ^2 for the interval $0<V<\infty$ [16].

$$f_{\phi}(\phi) = \int_{0}^{\infty} f_{V\phi}(V,\phi)\,d\phi = \frac{1}{2\pi}. \tag{4.66}$$

This expression is a uniform random variable within the interval $0 < \phi < 2\pi$ [16]. Hence, from observation,

$$f_{V\phi}(V,\phi) = f_{V}(V) f_{\phi}(\phi), \tag{4.67}$$

which implies that V and ϕ are independent. If we have the X and Y as zero mean common variance Gaussian random variables and functions 4.49 and 4.50 are uniformly distributed within the interval defined by $(0,2\pi)$, then $X + jY$ represents a complex Gaussian random variable [16],

$$Ve^{j\phi} = X + jY\ . \tag{4.68}$$

Therefore, from 4.68, we can conclude that the return voltage signals have Rayleigh magnitude distribution and uniform phase distribution.

To create the High Range Resolution (HRR) profile, the following sequence of events is processed in Matlab:

1.) Target Discretes Chosen

2.) Line-of-Sight Range Determined

3.) Received Signal Created

4.) Pulse Compression

5.) Matched Filtering

6.) Magnitude of Matched Filter Output Mapped to Range Domain

In order to better understand the underlying statistics of the data set, while simultaneously, providing metrics for the performance of the simulation, the

Komolgorov-Smirnov test is utilized. The Kolmogorov-Smirnov (K-S) goodness of fit test is useful for determining the statistical similarity of a vector of random variables and a specified normal distribution. The K-S test is also useful for determining the goodness of fit of two distributions that are not necessarily defined to be normal. The K-S test is valid for cases when the distributions are functions of a single independent variable, that is, data sets where each data point can be associated with a single number. These data points are then easily converted to an unbiased estimator, $S_N(x)$, of the cumulative distribution function (cdf) of the probability distribution from which the data set is drawn. In order to do so, the random variable vector must first be sorted into ascending order, thereby forming the cdf. Next, the values of the normal distribution-mean and variance-may be specified, or they can be assumed standard. All cdfs agree at the far tails, ~0/~1. The K-S test distinguished behavior between the upper and lower tails. The Kolomogorov-Smirnov goodness of fit test measures the maximum value of the absolute difference between the two proposed cdfs.

For the case of an unknown distribution and a known distribution, corresponding to the case for the simulation, the test statisitic, D, is formed by [17],

$$D = \max_{-\infty<x<\infty} \left| S_N(x) - P(x) \right|. \tag{4.67}$$

Where $P(x)$ is the normal distribution defined by the variables, μ and σ^2, representing the mean and variance, respectively; $S_N(x)$ denotes the empirical cumulative distribution function found from the sorted random variables

comprising the unknown distribution. What makes the K-S test useful is the distribution of [17],

$$\sum_{x=-\infty}^{\infty} D_{xi}\,. \tag{4.69}$$

The determination of the critical value is necessary in order to reject or accept the null hypothesis; the null hypothesis is that both distributions are the same. The critical value is found to from the formula developed by L.H. Miller [13],

$$CV = \sqrt{-0.5\frac{\log_{10}(\alpha)}{n}} - \frac{0.16693}{n} - \frac{A}{n^{1.5}}, \tag{4.70}$$

where,

$$A = 0.09037\left[-\log_{10}(\alpha)\right]^{1.5} + 0.01515\left[\log_{10}(\alpha)\right]^{2} - 0.08467\alpha - 0.11143 \tag{4.71}$$

and α is the significance level of the test; generally α is equal to 0.05, representing significance at the 5% level. The limiting values of CV are at the upper and lower tails,

$$\begin{aligned} CV(0) &= 1 \\ CV(\infty) &= 0 \end{aligned}, \tag{4.72}$$

with 1 denoting a rejection of the null hypothesis that the cdf of the unknown variable vector has a normal distribution. Thus, in terms of the CV function, the significance level of an observed value of D is given by [17],

$$\mathrm{P}_r = (D > observed) \cong CV\left(\sqrt{N}D\right). \tag{4.73}$$

The approximation of 4.73 becomes asymptotically accurate as the value of N tends towards infinity. Generally, a value of N=20 is sufficient for the K-S test to show normality [17]. A number less than N may still give valid results, however,

such results are prone to ambiguity, due to the lack of sample support. However, iterative testing showed that N=10 was sufficient to satisfy the K-S test for the range bin statistics validation; even though this value is less than N = 20 as stated in [17].

Since results for small population sizes are ambiguous, they are difficult to categorize, and hence, are not discussed within the context of this section. In order to adequately test and quantifiably show the theory presented in this section, the idealized extended target model was utilized. This target model relied on the use of a uniform random point scatterer generator to spread target points throughout a range swath of interest, thereby distributing approximately ten (10) reflectors per range bin. The K-S test was applied to each of the eleven (11) range bins that comprised the signature. Since each point on the signature represents the summation of all individual scatterers within that range bin, multiple variables, necessary for constructing the cumulative distribution function (CDF), were gathered across each range bin over all of the thirty-six (36) look angles. Results from a representative sample of the range bins are sufficient for examination of the theory previously introduced. All results are found in Appendix 2.A-2.K for future referencing.

Section 4.5-Angular Target Selectivity

Real-world targets often exhibit some sort of angular selectivity as a result of the specular surface that comprise the target skin. These specular surfaces could be curved or flat and exhibit a multitude of possible shapes and sizes. For the purpose of testing the idealized target structure, being comprised of 110 individual point scatterers, represents a hypothesized two-dimensional target structure exhibiting specular, or angular, selectivity. For this case study, individual scatterers were given amplitude functions that depended on the look-angle to the airborne radar platform. This amplitude function is rectangular in shape and has the characteristic frequency response given by the two-dimensional Sinc pulse as shown below,

$$A = \frac{A_x A_y}{\lambda^2} \frac{\sin\left[\left(u_x - u_{x0}\right)\frac{\pi A_x}{\lambda}\right]}{\left(u_x - u_{x0}\right)\frac{\pi A_x}{\lambda}} \frac{\sin\left[\left(u_y - u_{y0}\right)\frac{\pi A_y}{\lambda}\right]}{\left(u_y - u_{y0}\right)\frac{\pi A_y}{\lambda}}, \tag{4.74}$$

where the range variables u_x,

$$u_x = \sin(\theta)\cos(\phi), \tag{4.75}$$

u_{x0},

$$u_{x0} = \sin(\theta_0)\cos(\phi_0), \tag{4.76}$$

and cross-range variables u_y,

$$u_y = \sin(\theta)\sin(\phi), \tag{4.77}$$

and u_{y0},

$$u_{y0} = \sin(\theta_0)\sin(\phi_0), \tag{4.78}$$

are dependent upon the look angle to the target. The amplitude variables A_x and A_y represent the size of the proposed specular target structure. For this simulation, they are given by,

$$\begin{aligned} A_y &= [1\lambda, 5\lambda, 10\lambda, 15\lambda, 20\lambda] \\ A_x &= [1\lambda, 5\lambda, 10\lambda, 15\lambda, 20\lambda] \end{aligned}. \tag{4.79}$$

The equation 4.74 is applied uniformly to all selective targets. This has a noticeable effect when a large number of target discretes become selective, then a spike is observed in the HRR signature. An example of this spike is shown below:

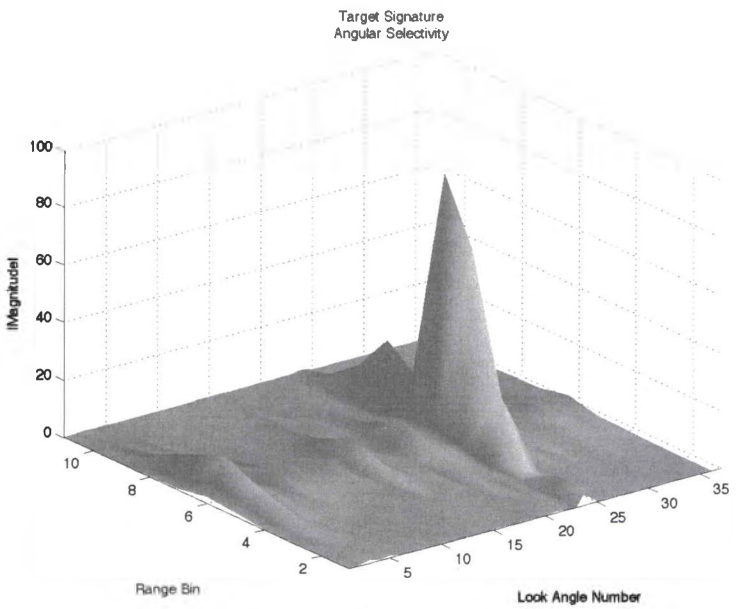

Figure 39: 100 Target Discretes Angularly Selective

What is of most consequence is the affect a number of selective targets have on the overall magnitude of a single range bin. In order to test the case of several

uniformly distributed point targets and a single specular reflection over a range of values, an experiment was derived for an ensemble of signatures. Initially, the target signature is created for the case of a single range bin populated by target discretes. Next, only the range bin of interest is sampled to capture the magnitude resulting from the case only the azimuth or elevation angle is varied. Finally, the specular reflectivity is varied over a number of values in order to try and elicit a magnitude response in the sampled range bin.

Target discretes were placed in the central range bin and the distribution shown in the plot below:

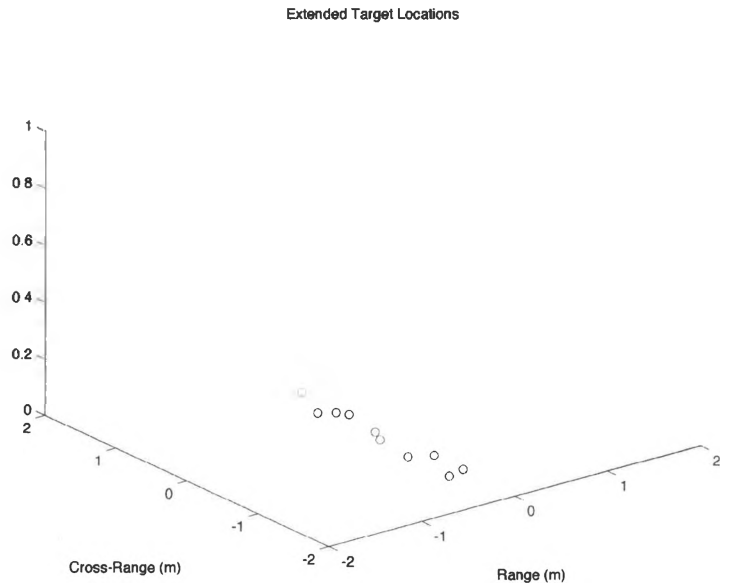

Figure 40: Target Locations Utilized for Testing

Elevation Sweep vs. Range Specular Reflectivity

The amplitude of the specular reflection is modified via the size of the specular surface, A_x and A_y. In this case, A_y is held constant at 1λ, while the range size is varied over $A_x = [1\lambda, 5\lambda, 10\lambda, 15\lambda, 20\lambda]$. Additionally, only the elevation angle is sweeped from 22.5° to 27.5°. The range bin of interest is sampled, and the magnitude plotted vs. u_x.

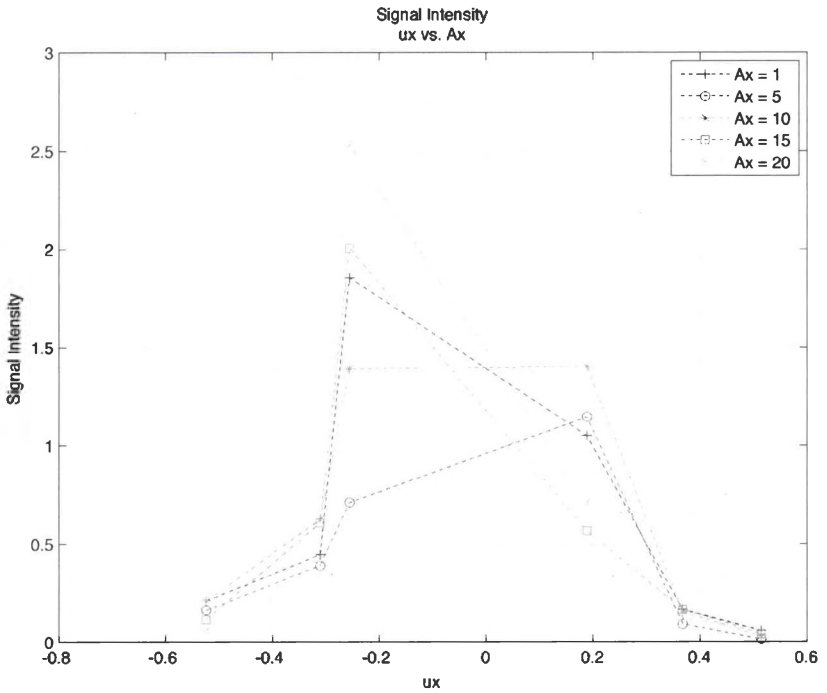

Figure 41: Signal Intensity Plot

From figure 41, there seems to be no discernible difference in signal intensity versus the range specular reflectivity of the target for several cases. This indicates no relationship between signal intensity and elevation angle versus range specular reflectivity.

Elevation Sweep vs. Cross-Range Specular Reflectivity

The amplitude of the specular reflection is modified via the size of the specular surface, A_x and A_y. In this case, A_x is held constant at 1λ, while the range size is varied over $A_y = [1\lambda, 5\lambda, 10\lambda, 15\lambda, 20\lambda]$. Additionally, only the elevation angle is sweeped from 22.5° to 27.5°. The range bin of interest is sampled, and the magnitude plotted vs. u_y.

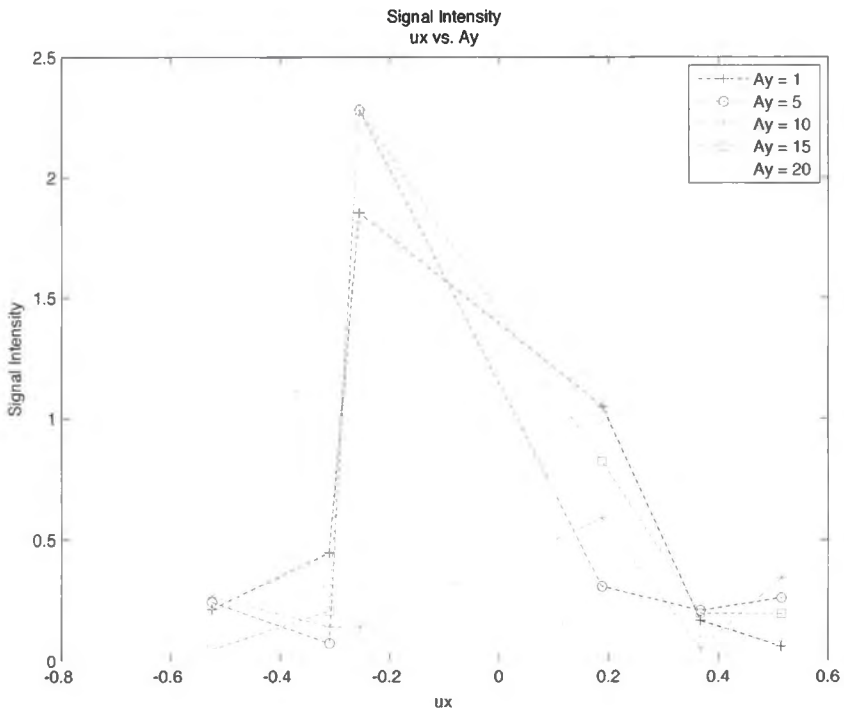

Figure 42: Signal Intensity Plot

From figure 42, there seems to be no discernible difference in signal intensity versus the cross-range specular reflectivity of the target for several cases. This indicates no relationship between signal intensity and elevation angle versus cross-range specular reflectivity.

Azimuth Sweep vs. Range Specular Reflectivity

The amplitude of the specular reflection is modified via the size of the specular surface, A_x and A_y. In this case, A_y is held constant at 1λ, while the range size is varied over $A_x = [1\lambda, 5\lambda, 10\lambda, 15\lambda, 20\lambda]$. Additionally, only the azimuth angle is sweeped from 42.5° to 47.5°. The range bin of interest is sampled, and the magnitude plotted vs. u_x.

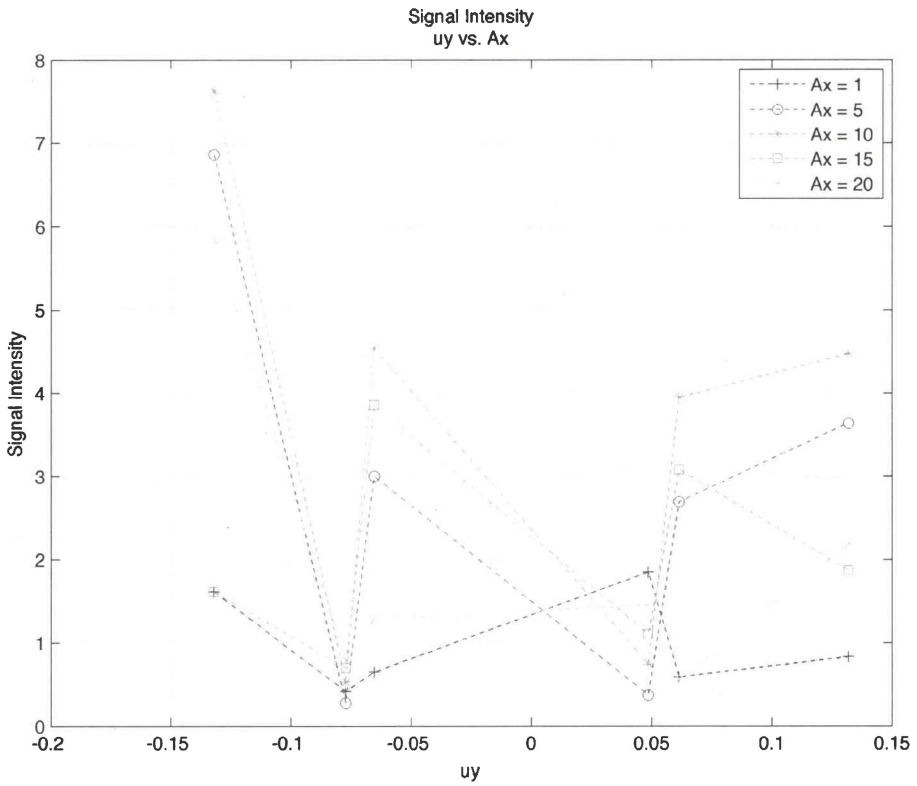

Figure 43: Signal Intensity Plot

From figure 43, there seems to be no discernible difference in signal intensity versus the range specular reflectivity of the target for several cases. This

indicates no relationship between signal intensity and azimuth angle versus range specular reflectivity.

Azimuth Sweep vs. Cross-Range Specular Reflectivity

The amplitude of the specular reflection is modified via the size of the specular surface, A_x and A_y. In this case, A_x is held constant at 1λ, while the range size is varied over $A_y = [1\lambda, 5\lambda, 10\lambda, 15\lambda, 20\lambda]$. Additionally, only the azimuth angle is sweeped from 42.5° to 47.5°. The range bin of interest is sampled, and the magnitude plotted vs. u_y.

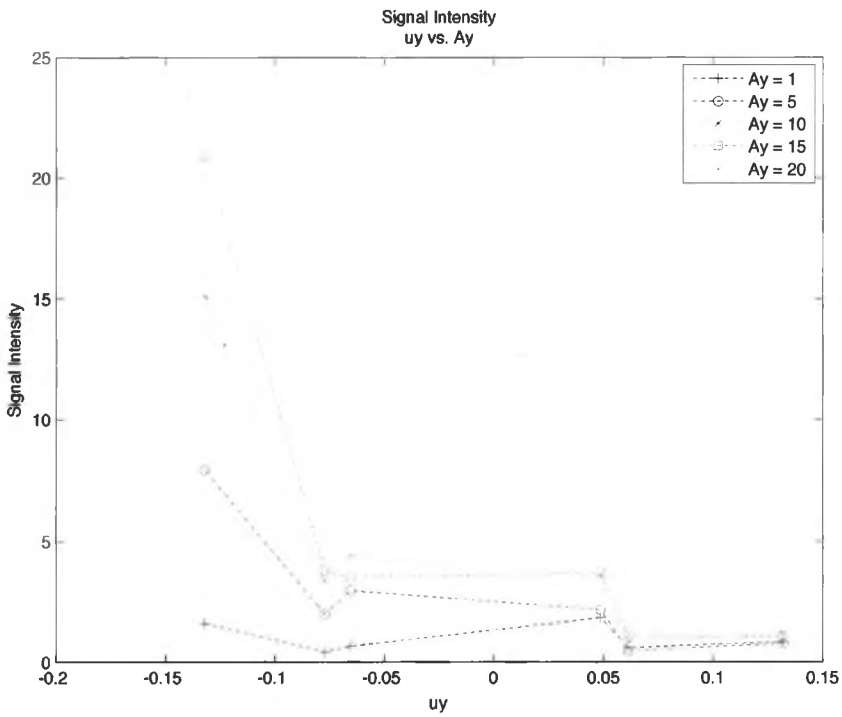

Figure 44: Signal Intensity Plot

From figure 44, there seems to be no discernible difference in signal intensity versus the cross-range specular reflectivity of the target for several cases. This indicates no relationship between signal intensity and azimuth angle versus cross-range specular reflectivity.

Visual Inspection of Angular Selectivity Phenomenology

While quantitative testing shows definitive results that show no observable correlation between specular reflectivity and signal strength, another experiment would be to show the affect of multiple targets having the same specular reflectivity over the look window. This case randomly chooses a point target to be either uniform or specularly reflective; cases considered are for 1, 10, 50, 100 targets, respectively. What will become evident is that for the simple case of 1 angularly selective point scatterer, there is a negligible visual impact. However, as the number increases, there is a noticeable spike for the peak look angle of

To begin, the overlapping high-range resolution (HRR) signature will be shown for the case of 1, 10, 50, and 100 specularly selective point targets; this will be followed the corresponding three-dimensional surface plot of the HRR signature. What is observable (from figures 45-52), is that for the case of 1 specular structure (fig. 45,46), there is a negligible effect; now extend that to the case of 10,50, and 100 spculars structures (fig. 47-52), and suddenly, there is a rather large peak that appears in the HRR signature. This large peak is only present in one location, across all range bins. This is so due to the inherent

nature of the point-spread function approximation of the range bin sample; eventhough there is a single sample per range bin, following reconstruction, the signal is present in all range bins. Hence, the angularly reflectivity flash is observable for a single look angle, as defined by 4.74; however, an explicit assumption that follows is this is valid for only for a given single look and pose angle. The pose angle criteria is referenced to the fact that an actual target would have a varying specular surface and rotation of that surface in reference to the airborne radar platform would violate the conditions of 4.74, such that, there would be no observable flash upon illumination for the maximimum of 4.74. More to the point, the flash is observable for a given look and pose angle, but due to the spreading and summation of the complex signal across all of the range bins, there is no established manner of determining the origin of the flash. The question posed is simply, "Can I tell which range bin from which the flash originiated?" For this example, the answer is esoteric, but the persistent feature set that defines this particular idealized extended structure is just the flash that appears in only one look angle. Could this solitaire peak be effectively utilized to identify the underlying target of interest?

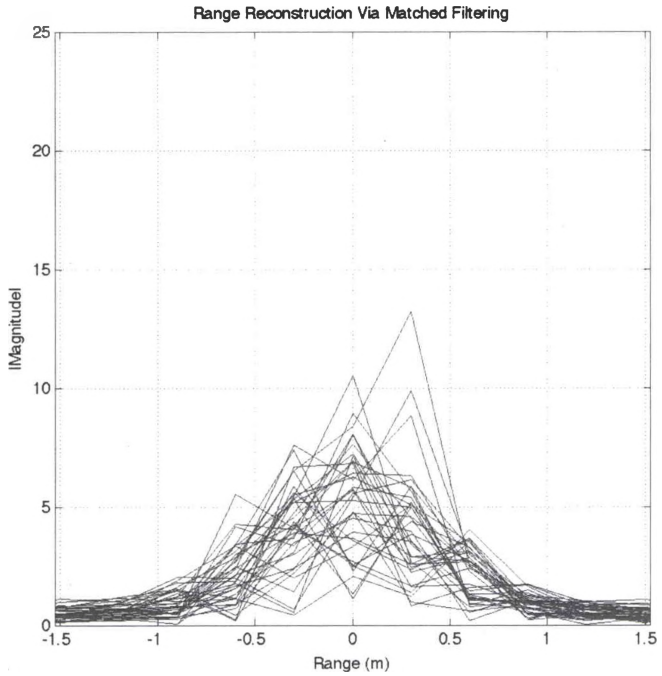

Figure 45: 1 Specular Target HRR Signature (2-D)

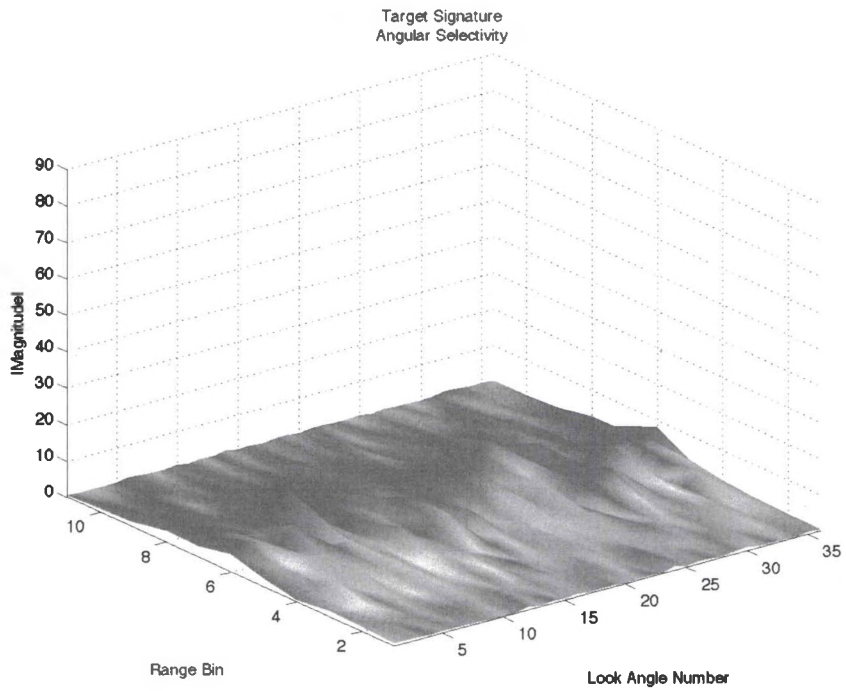

Figure 46: 1 Specular Target HRR Signature (3-D)

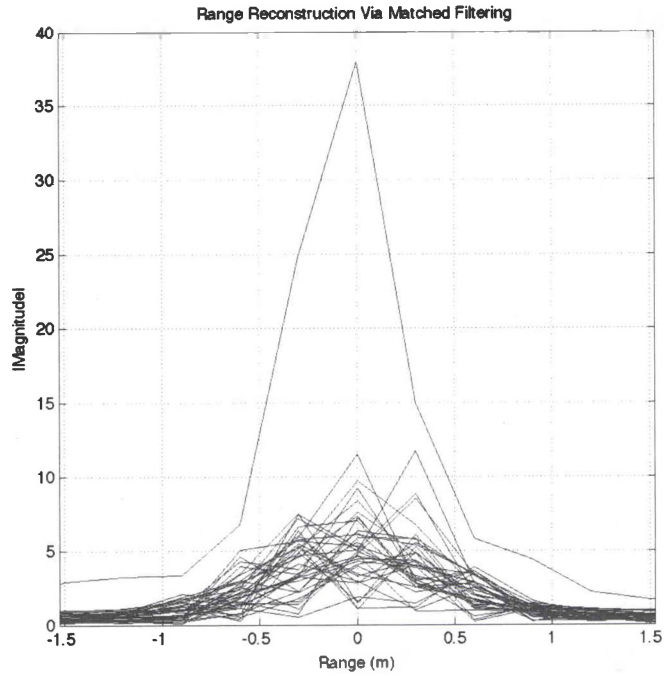

Figure 47: 10 Specular Targets HRR Signature (2-D)

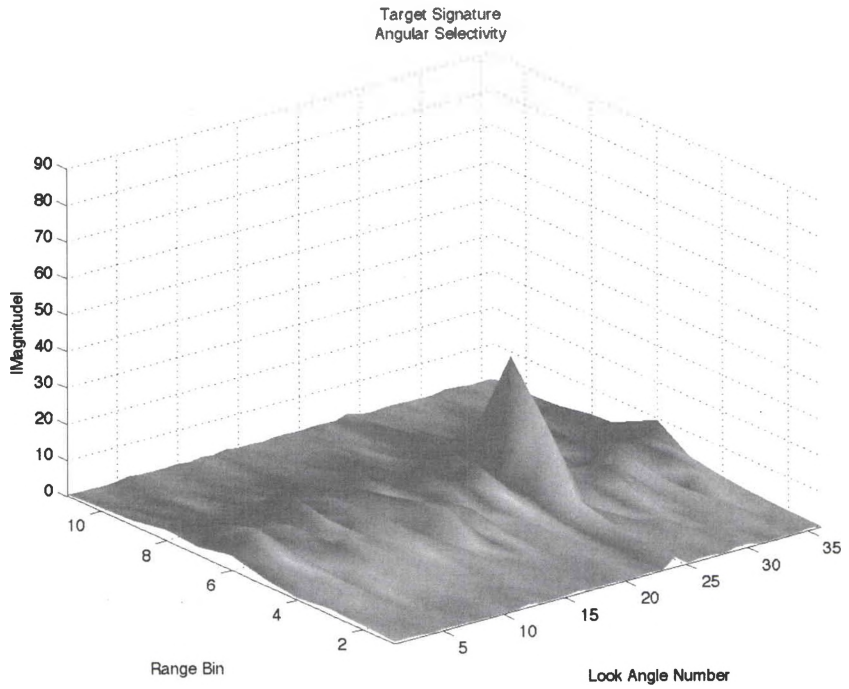

Figure 48: 10 Specular Targets HRR Signature (3-D)

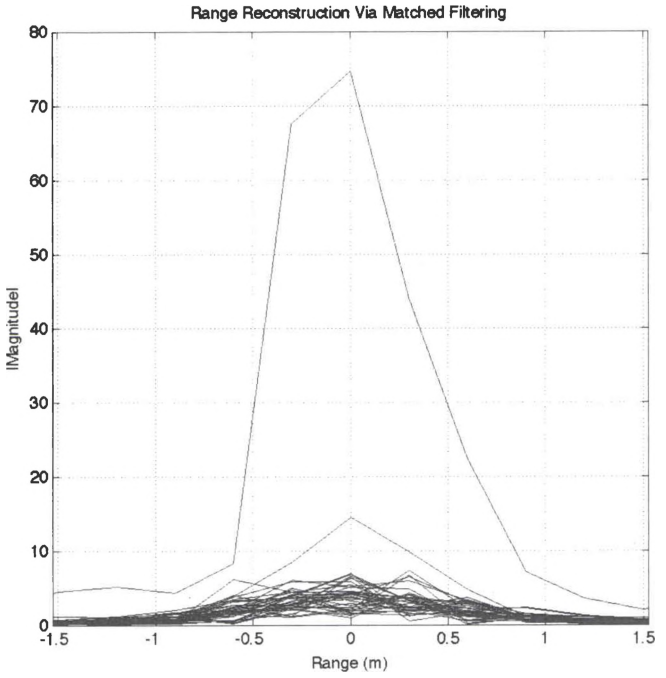

Figure 49: 50 Specular Targets HRR Signature

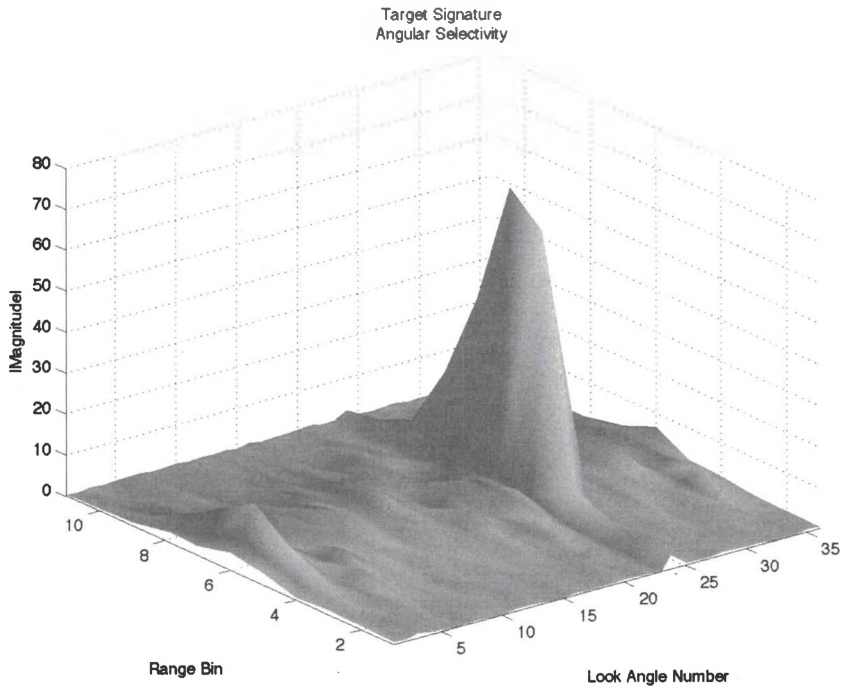

Figure 50: 50 Specular Targets HRR Signature (3-D)

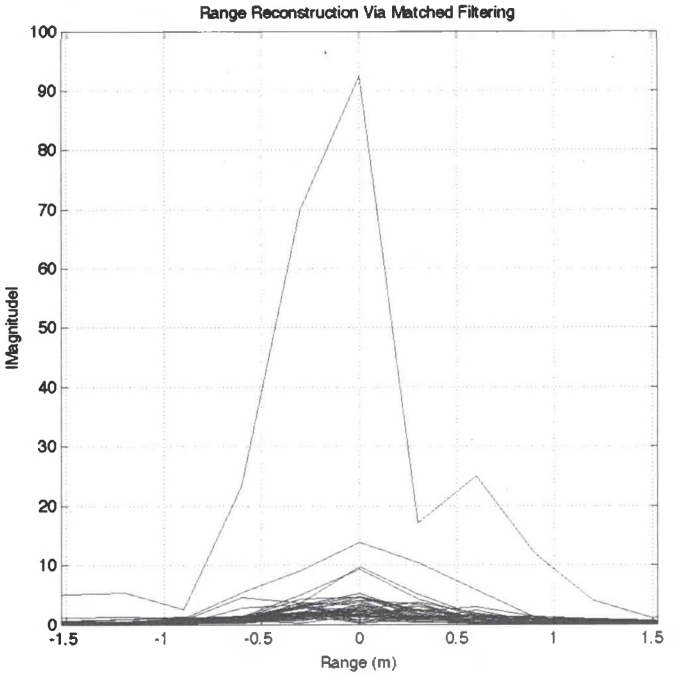

Figure 51: 100 Specular Targets HRR Signature

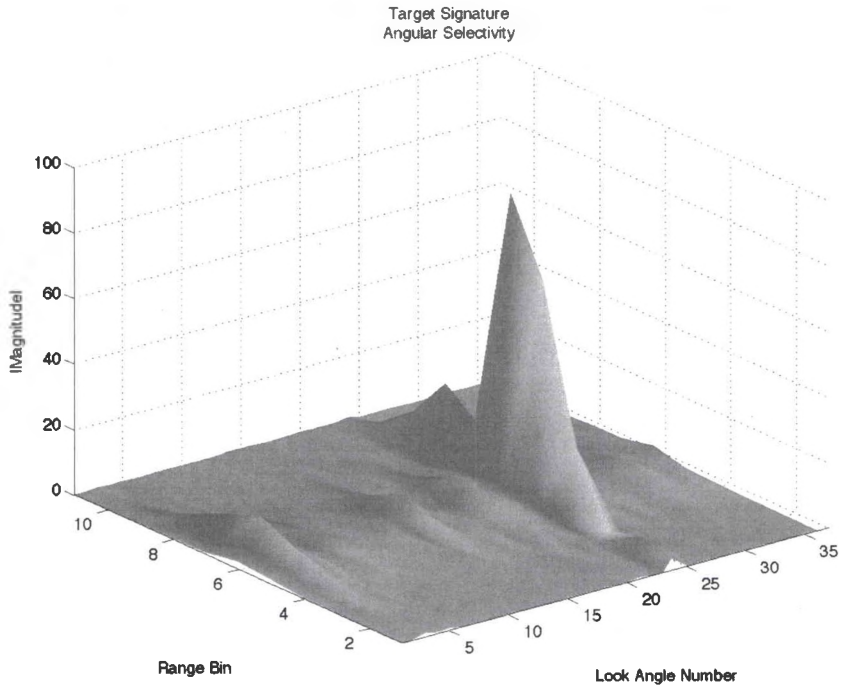

Figure 52: 100 Specular Targets HRR Signature (3-D)

Section 4.6-Frequency Target Selectivity

Exclusive of the angular selectivity concern of an actual real-world target, is that of target skin frequency selectivity. Assuming that the material composition of some theorized extended surface displays at least a modicum of frequency selectivity, what effect will this have on the high-range resolution (HRR) signature? For the case where the selectivity is characterized by the formula,

$$h(f) = \exp\left(-\frac{(f - f_0)^2}{\sigma_f^2} \right), \tag{4.80}$$

with $\sigma_f^2 = BW$. Following normalization, 4.80 becomes,

$$h_{norm}(f) = \frac{1}{\sqrt{2\pi}} \frac{1}{\sigma_f^2} \exp\left(-\frac{(f - f_0)^2}{2\sigma_f^2} \right). \tag{4.81}$$

If our signal representation is modeled as the general form, $s(f)$, the received signal following impact is,

$$r(f) = s(f)h(f). \tag{4.82}$$

Since 4.80, which normalizes to 4.81, is the form of the Gaussian [7], the effect of the frequency selective surface is a spreading of the reflected signal received at the radar aperture. The overall smearing of the received signal is controlled by the bandwidth of the selective target skin, σ_f^2. The following examples demonstrate the effect of a selective target surface on the HRR signature, for both the two-dimensional and three-dimensional cases.

Cases considered for this observation include 100 MHz and 1000 MHz. This represents approximately 20% and 200% of the transmit waveform bandwidth. Additionally, this order of magnitude difference in frequency selectivity should be more readily observable in graphical form. First of these two test cases is the 100 MHz frequency selective surface.

Frequency Selective Targets: 100 MHz

For this test case, the frequency selectivity of the idealized point target representation of the extended target structure is 100 MHz. Initially, only one (1) of 110 point scatterers is given a frequency selective reflectivity. This case is then extended to 10, 50, and then 100 frequency selective target discretes. Observable is the effect of a frequency selective bandwidth on the corresponding HRR signature. For the first case, there is a negligible effect, and this roughly is the uniform reflectivity of the control scenario. As the number of targets that are frequency selective increases, there is a smearing of the HRR signature peaks. As the discretes are chosen randomly, in conjunction with, the nature of the point-spread function approximation of the range bin sample, the final observed phenomena is that the HRR signature appears as a relatively smooth surface. Ripples corresponding to the constructive and destructive interference phenomena of the summation of all target point-spread functions gives rise to the roughness of the HRR signature for the case of 100 frequency selective targets.

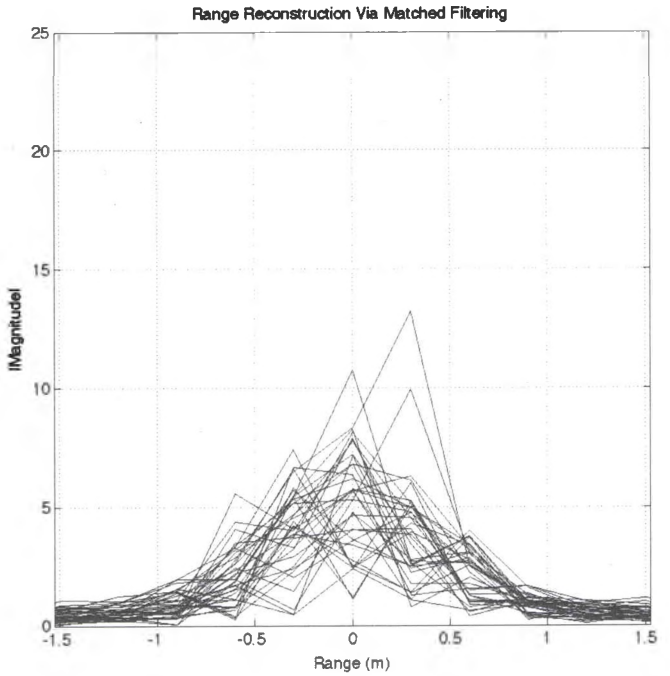

Figure 53: 1 Frequency Selective Target (100 MHz) HRR Signature (2-D)

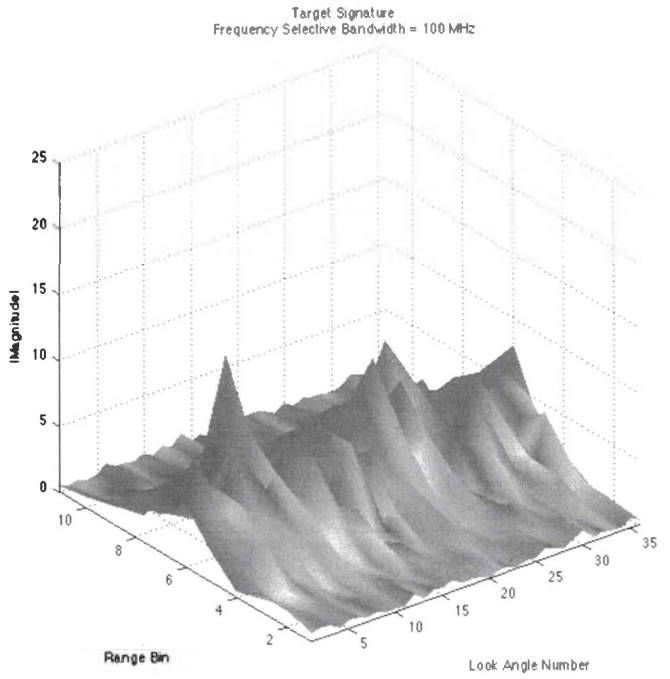

Figure 54: 1 Frequency Selective Target (100 MHz) HRR Signature (3-D)

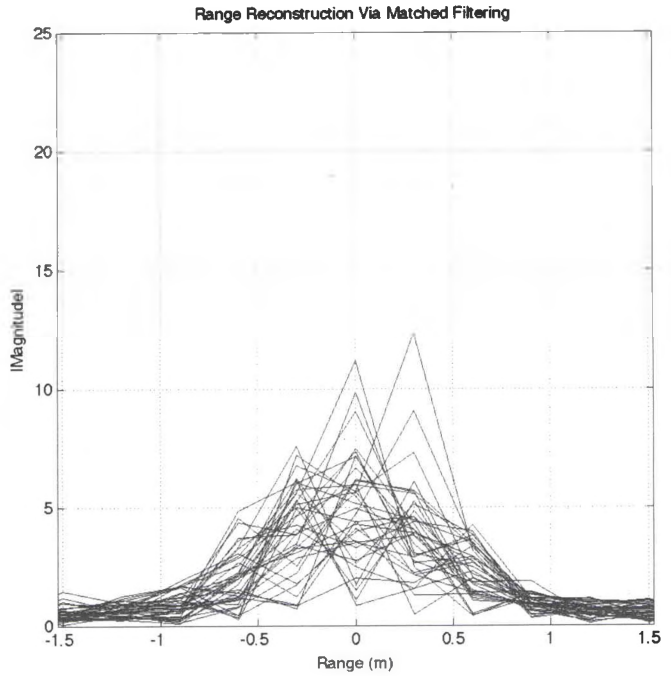

Figure 55: 10 Frequency Selective Targets (100 MHz) HRR Signature (2-D)

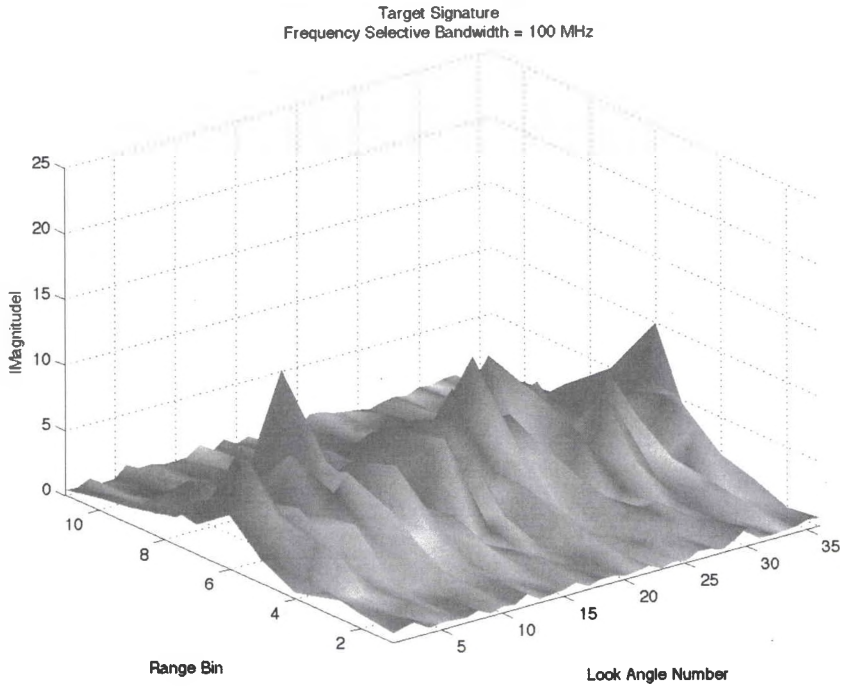

Figure 56: 10 Frequency Selective Targets (100 MHz) HRR Signature (3-D)

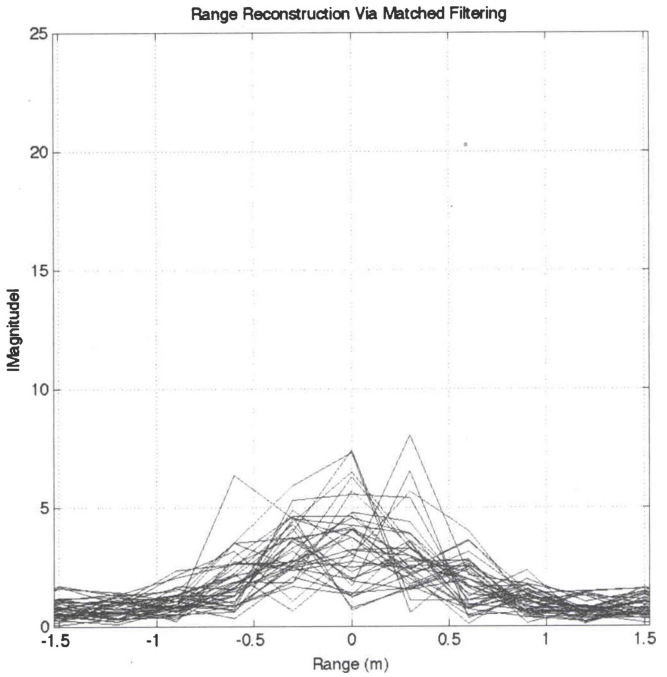

Figure 57: 50 Frequency Selective Targets (100 MHz) HRR Signature (2-D)

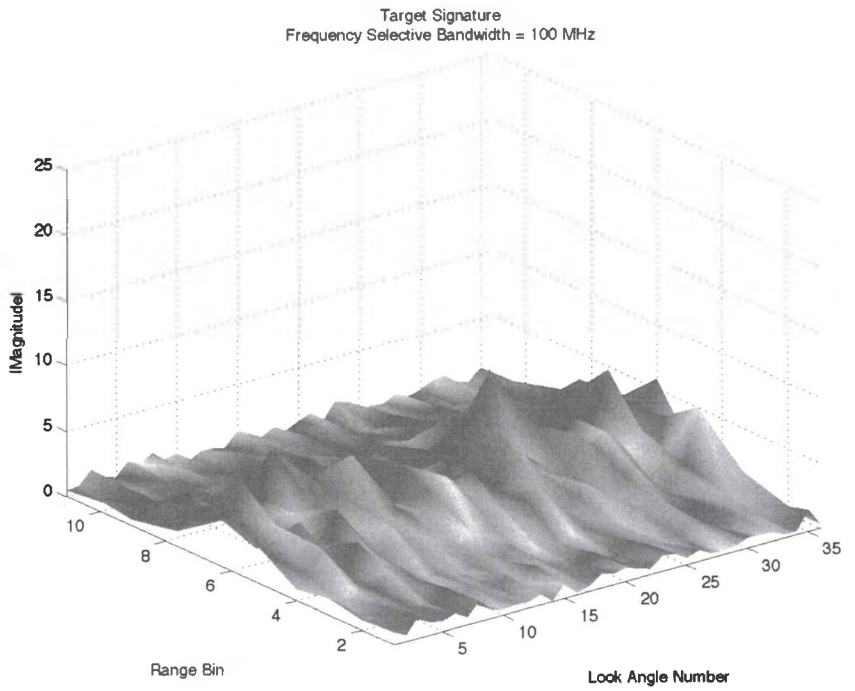

Figure 58: 50 Frequency Selective Targets (100 MHz) HRR Signature (3-D)

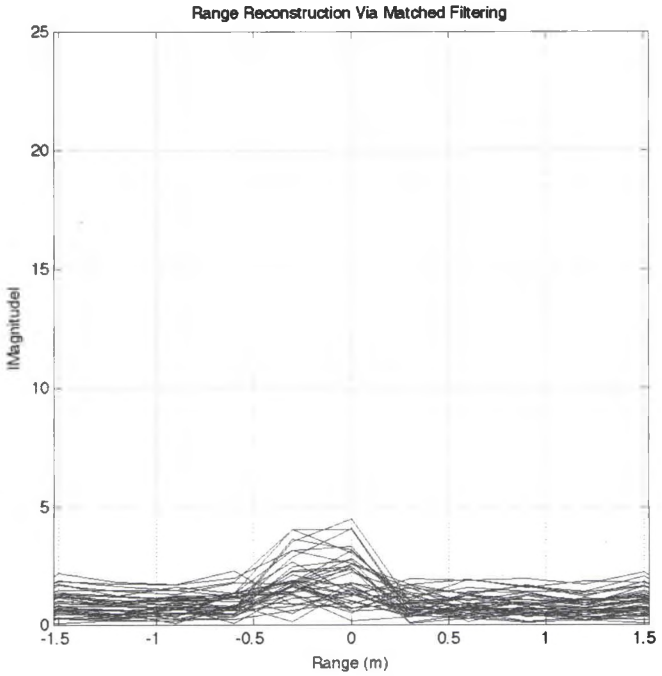

Figure 59: 100 Frequency Selective (100 MHz) HRR Signature (2-D)

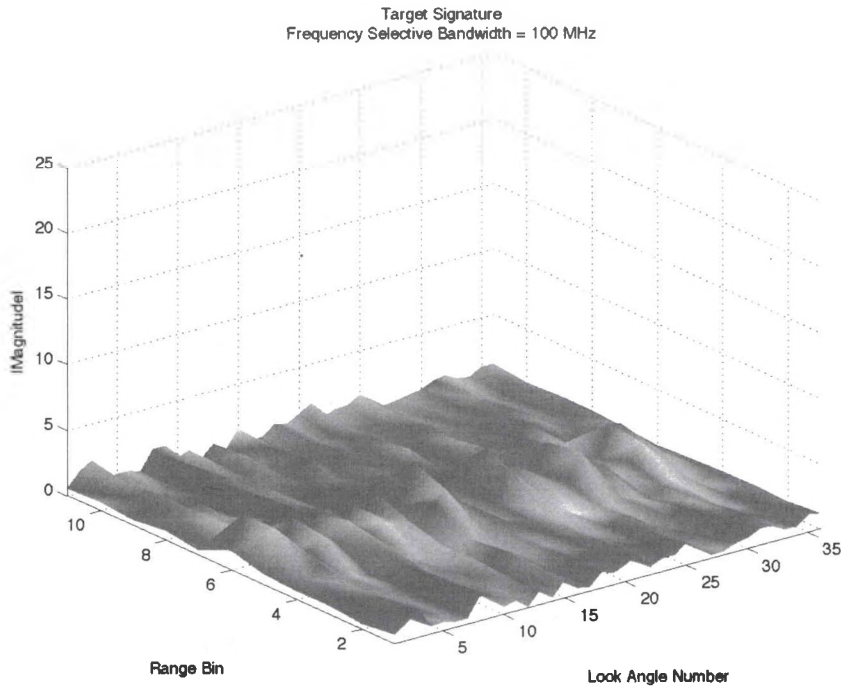

Figure 60: 100 Frequency Selective Targets (100 MHz) HRR Signature (3-D)

Frequency Selective Targets: 1000 MHz

As the magnitude of the matched filtered output is a range-domain representation of the frequency domain in which the frequency selectivity is implemented, there is an important consideration to observe when the selectivity of the target skin is increased. This is the duality conjugate nature of the frequency-time domain; if an infinite bandwidth is observed in the frequency-domain, the time domain representation is a delta function. Since the range-domain is a scaled constant of the corresponding time-domain of the frequency-domain implementation of the frequency selectivity, this wider bandwidth case of 1000 MHz should result in less smearing of the high-range resolution (HRR) signature; for both the two-dimensional and three-dimensional cases. Explicit in this argument is the subjective nature of visual inspection; thereby, this test case is assumed true.

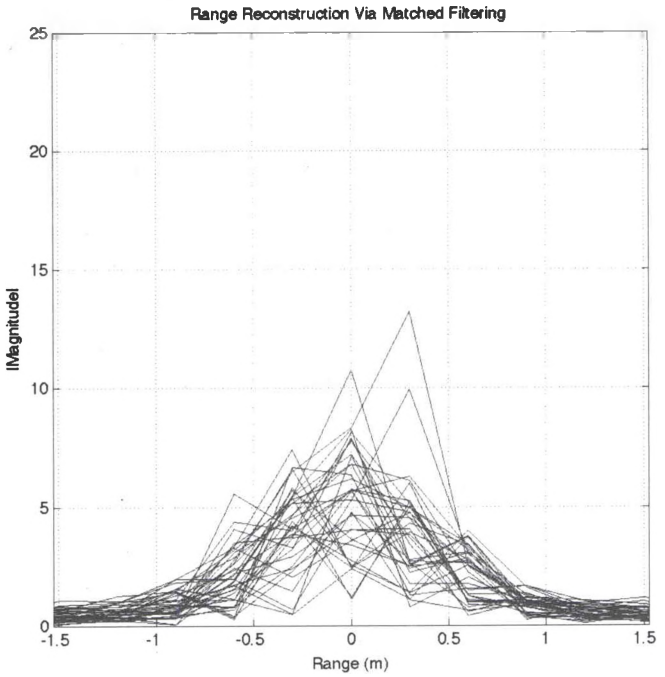

Figure 61: 1 Frequency Selective Target (1000 MHz) HRR Signature (2-D)

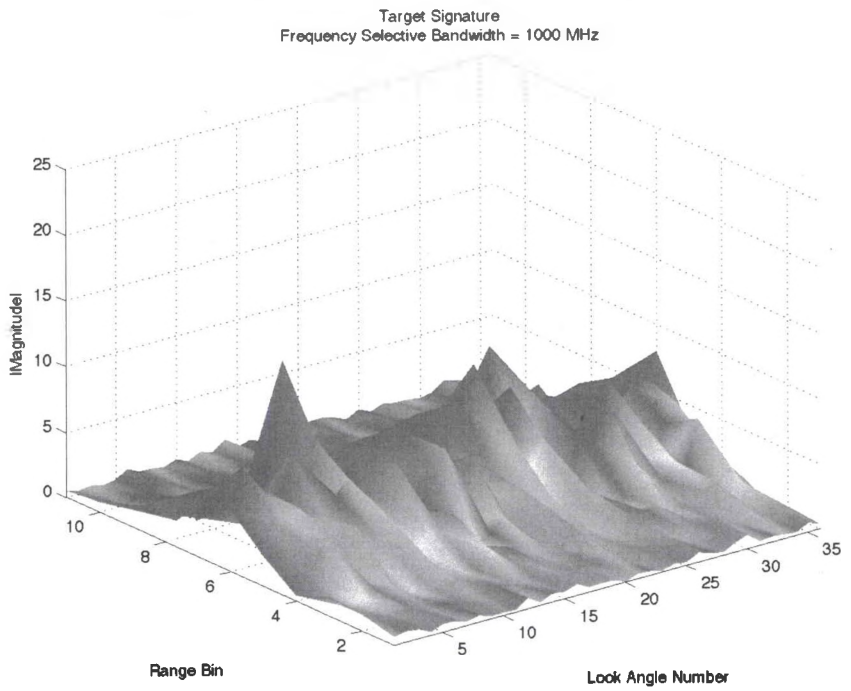

Figure 62: 1 Frequency Selective Target (1000 MHz) HRR Signature (3-D)

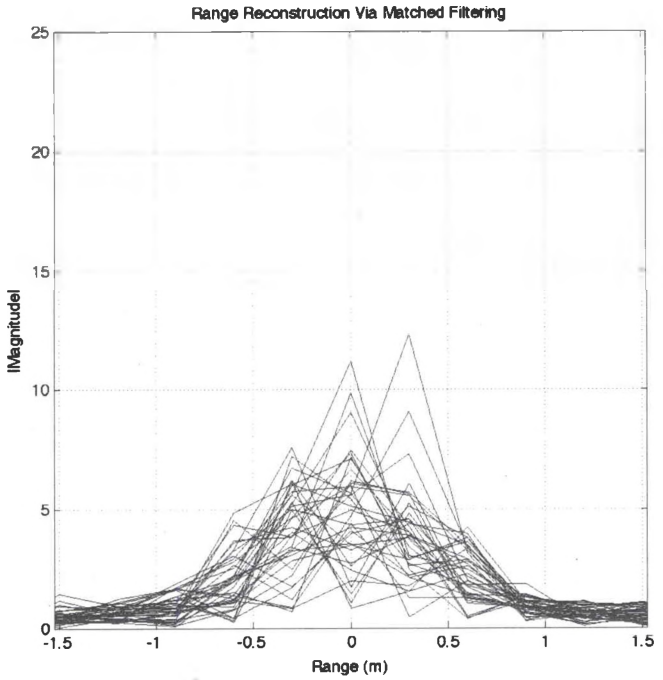

Figure 63: 10 Frequency Selective Targets (1000 MHz) HRR Signature (2-D)

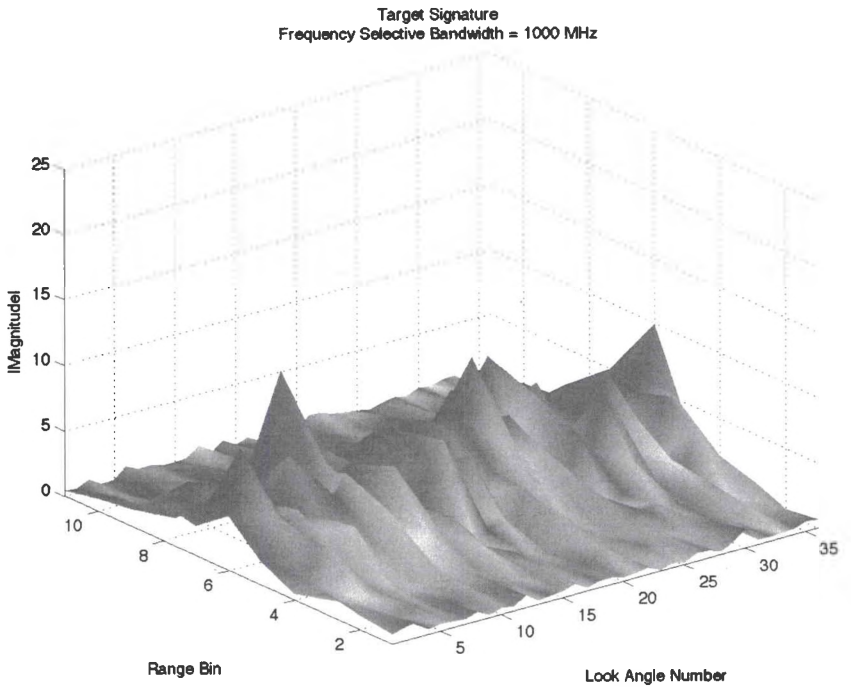

Figure 64: 10 Frequency Selective Targets (1000 MHz) HRR Signature (3-D)

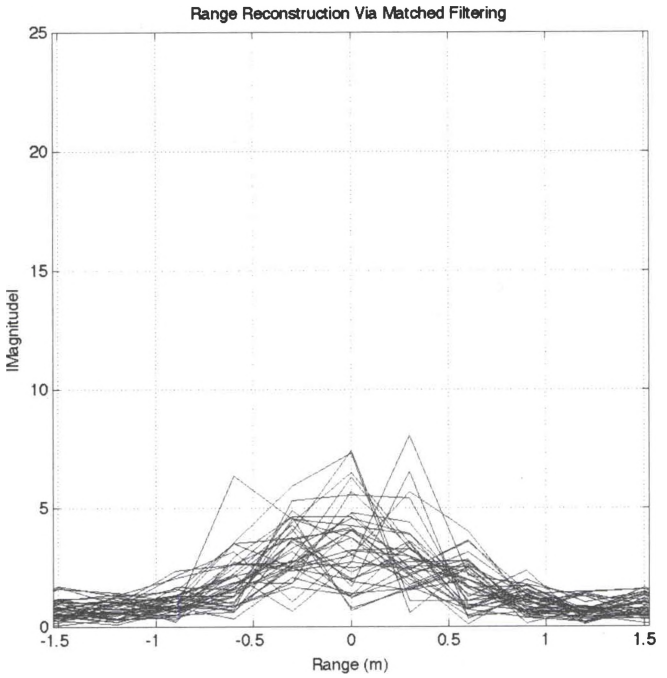

Figure 65: 50 Frequency Selective Targets (1000 MHz) HRR Signature (2-D)

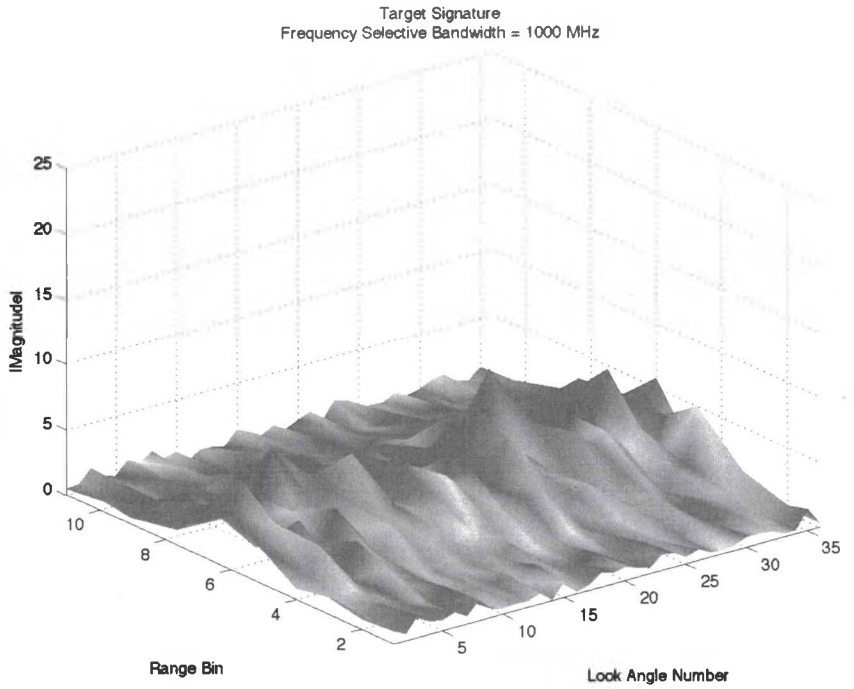

Figure 66: 50 Frequency Selective Targets (1000 MHz) HRR Signature (3-D)

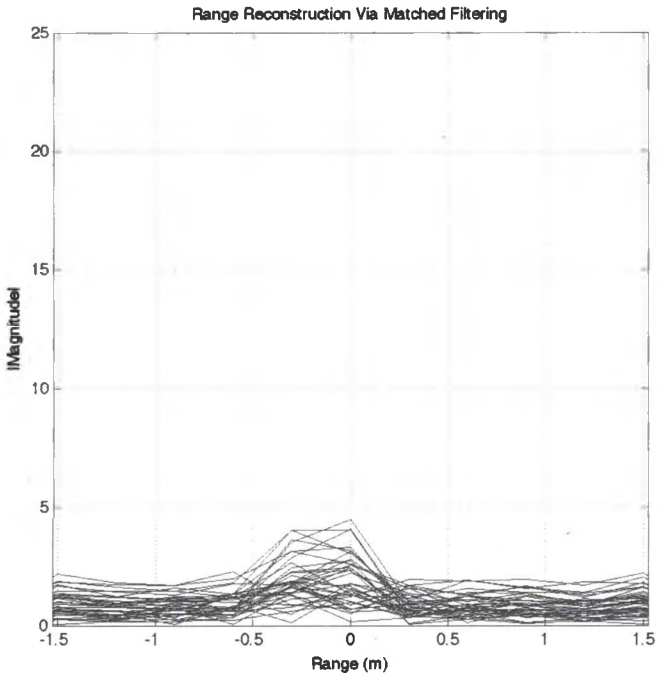

Figure 67: 100 Frequency Selective Targets (1000 MHz) HRR Signature (2-D)

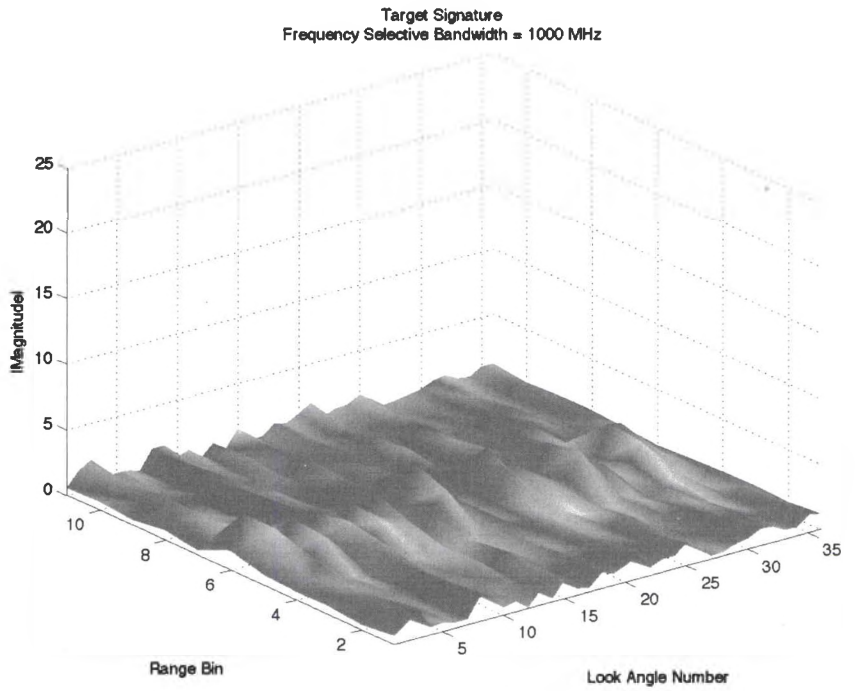

Figure 68: 100 Frequency Selective Targets (1000 MHz) HRR Signature (3-D)

Summary

Having visually examined the frequency selective target case for 100 MHz and 1000 MHz, one effect is certainly observable; that of the smearing phenomena inherent in the bandwidth of the frequency selective due to the duality conjugate of the frequency and time-domain representations. In light of this previous subjective investigation, a more objective test case is considered.

For this example, a single frequency selective target discrete was chosen to have a bandwidth of 10-5000 MHz. This is similar to the test examples of section 4.5, where the signal intensity magnitude of the range bin containing the specular target were plotted versus the look-angle. In the same manner, the sample is in the range bin containing the frequency selective target. The magnitude of the HRR profile is sampled in this range bin over all look angles (36 in total). The sample value is then sorted and plotted for the varying bandwidths of 10 MHz, 100 MHz, 500 MHz, 1000 MHz, and 5000 MHz. If there is a dependence on the magnitude of the matched filtered output on the frequency selectivity of the target, then this plot will show this dependence. However, from figure 69, there is no perceivable difference in the magnitude of the sampled range bin, over all look angles, for the varying bandwidths! An intriguing example that demonstrates the difficulty in relying on the 1-D HRR signature for an identification of a frequency selective target without some further *a priori* knowledge of the target structure.

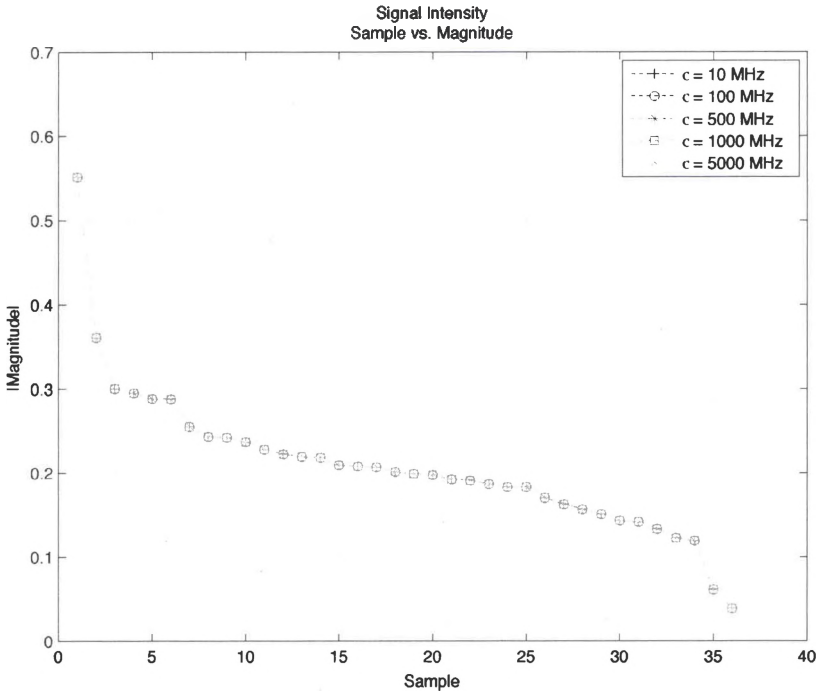

Figure 69: Frequency Selective Target Signal Intensity Plot

Section 4.7-Signal Subspace Representation of Idealized Target Structure

The method utilized to expose the high-range resolution signal subspace is the eigen decomposition of the covariance matrix of the *V*-dimensional observation vectors of length *Z*. Remember that the HRR profile, for a given pair of azimuth and elevation look angles within the look window, is just one observation vector of the HRR signature; the HRR signature being a *ZxV* matrix. Since the values comprising the HRR signature are complex valued, so too, is the covariance matrix, or correlation matrix. Defining *V* as the HRR profile vector for a given azimuth and elevation look angle pair, *I,j*,

$$V_{ij} \in \left[x_1, x_2, \ldots, x_k\right]^T, \tag{4.83}$$

and,

$$Z \in \left[V_{11} \ldots V_{1j}, V_{21} \ldots V_{2j}, \ldots, V_{i1} \ldots V_{ij}\right]. \tag{4.84}$$

Where *k* is the max range bin and the superscript, *T*, stands for the matrix transpose. The covariance matrix is defined as [21],

$$Cov[V,V] = E\left[(V-\mu)(V-\mu)^*\right]. \tag{4.85}$$

The covariance of a complex valued column vector is the product of the expected value of that given vector and the corresponding Hermitian transpose. Equation 4.85 can be rearranged into the form,

$$Cov[V,V] = E\left[VV^*\right] - E\left[\mu\mu^*\right]. \tag{4.86}$$

4.85 or 4.86 is also commonly shown in the form,

$$Cov[V,V] = \sum_{k=1}^{K} \frac{(V_k - \mu_k)(V_k - \mu_k)^*}{K}, \tag{4.87}$$

with *K* representing the kth range bin of a single observation vector, V_{ij}.

The values of the covariance matrix provide a useful method in which to compare the measure of strength of, in this instance, two random variates. Recognizing that 4.87 is a special case of the covariance matrix in which the two random variates are equivalent gives rise to the useful identity,

$$Cov[V,V] = E\left[V^2\right] - E[V]^2, \tag{4.88}$$

$$Cov[V,V] = \sigma_{VV}^2. \tag{4.89}$$

The subscript of 4.89 is a useful method of identifying the two random variates that are responsible for the variances that appear on the diagonal of the covariance matrix. For the case of 4.89, the size of the covariance matrix is VxV. From 4.88 and 4.89, we note that the covariance of vector V is the variance of V.

Now, given a set of random variates, Z, the first-order covariance matrix is given as [21],

$$Var\left(Z_{ij}\right) = Cov\left[Z_i, Z_j\right] = E\left[\left(Z_i - \mu_i\right)\left(Z_j - \mu_j\right)^*\right]. \tag{4.90}$$

Previously, the observation vectors were shown to each be normally distributed with zero means and scalar standard deviations, $N(0,\sigma)$. Using this parametrically to solve for the covariance of the matrix of the HRR signature, we have [21],

$$Cov[Z,Z] = \frac{1}{Q} ZZ^*. \tag{4.91}$$

Equation 4.91 is the unbiased estimate of the covariance Z. The value Q represents the number of observation vectors comprising Z. Thus, for *M* total observations, 4.91 can be rewritten as [21],

$$Cov[Z,Z] = \frac{1}{M-1} ZZ^*. \tag{4.92}$$

An important note on 4.92, the covariance of a complex-valued matrix is also complex-valued. From the properties of the covariance matrix, 4.92 is also positive-semidefinite, meaning that the Hermitian matrix behaves in much the same way as positive real numbers. This will become more relevant once the signal subspace is introduced. For now, the property in relation to the

eigendecomposition of a positive-semidefinite matrix, results in positive real-valued eigenvalues.

The final set of examples derived from the idealized extended target structure detail the signal subspace representation of the uniform, angular and frequency selective target cases. Observable is a deterministic, not subjective difference in signature characteristics in relation to the test case considered. Two plots are given for each of the examples already considered; they represent the full signal subspace and the zoomed signal subspace, respectively. The zoomed signal subspace focuses on the bulk of the eigenvalues that are dwarfed by the principal eigenvalue in the full signal subspace plots. The key trait that is considered hereafter is whether the affects of a uniform or selective target are observable within the eigenvalues of the signal subspace, and if so, are these characteristics significant in relation the uniform control case.

Uniform Target Reflectivity

As manner of semantics, significant eigenvalues are those with values greater than 1. Each eigenvalue represents a mode of the signal subspace. Thereby, all eigenvalues less than 1 are viewed as noise. As all received signals consist of a signal plus noise plus interference component, $r(t) = s(t) + n(t)$, the signal subspace is a useful measure of information content within the received signal. For the uniform reflectivity case, sans selectivity, the signal subpspace is of mode 5.

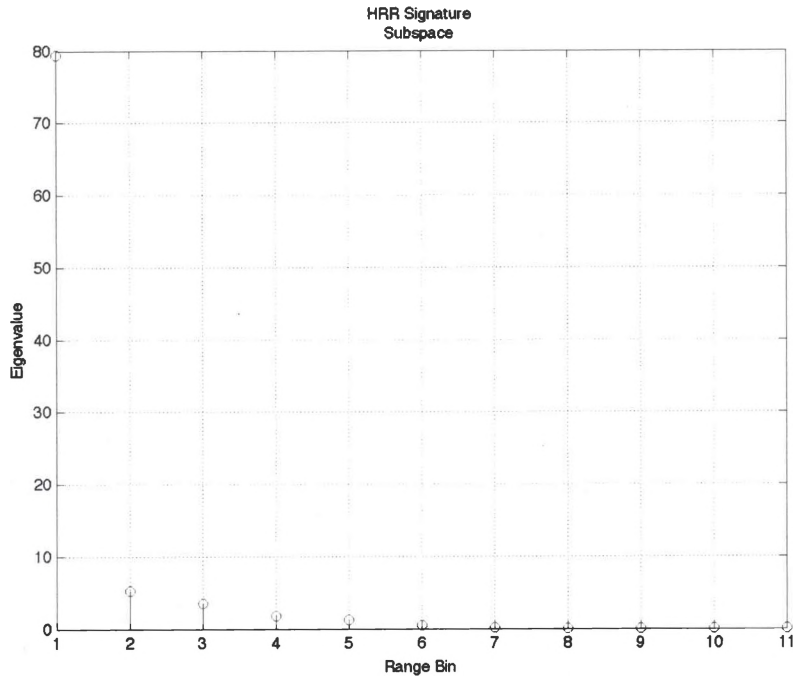

Figure 70: Uniform Target Reflectivity Signal Subspace (Full)

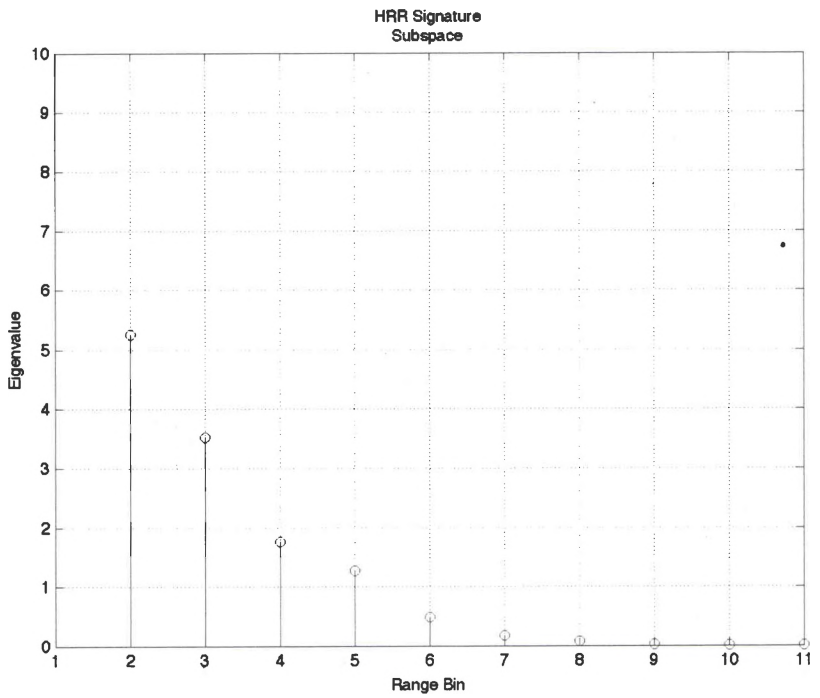

Figure 71: Uniform Target Reflectivity Signal Subspace (Zoomed)

Range Bin	Eigenvalue
1	78.8978
2	5.0953
3	3.8569
4	1.7486
5	1.2000
6	0.4962
7	0.1848
8	0.0786
9	0.0251
10	0.0096
11	0.0027

Figure 72: Uniform Target Eigenvalue Table

Angularly Selective Target

For the case of 1 specular target, there is no observable effect on the signal subspace eigenvalues (figure 72). However, as the number of angular selective discretes increases, so does the principal eigenvalue (figures 73-80), by a significant amount. This would indicate interdependence on specular target numbers and signal subspace eigenvalues. This assumption is only valid for the principal case, though, as all other eigenvalues decrease in value as the number of specular targets increases; indicating more noise is introduced in the signature in relation to the number of selective target structures. As a consequence, there is greater difficulty in determining salient feature sets on target as the number of specular target discretes inceases.

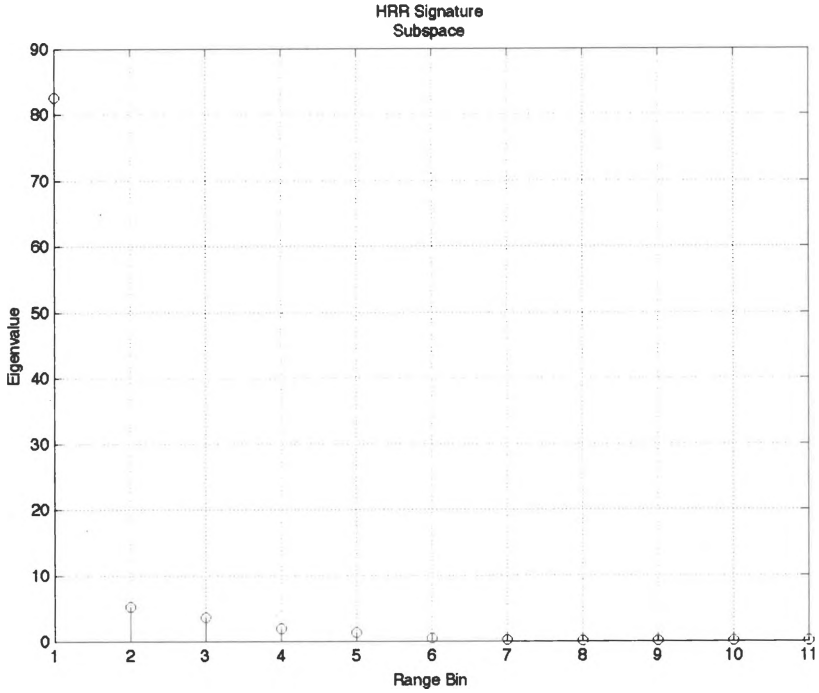

Figure 73: 1 Angularly Selective Target Signal Subspace (Full)

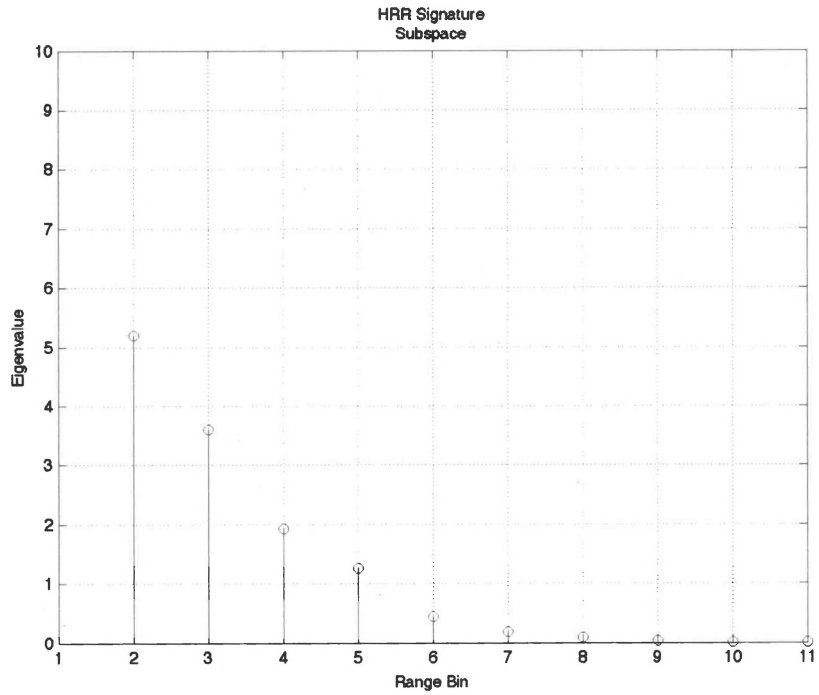

Figure 74: 1 Angularly Selective Target Signal Subspace (Zoomed)

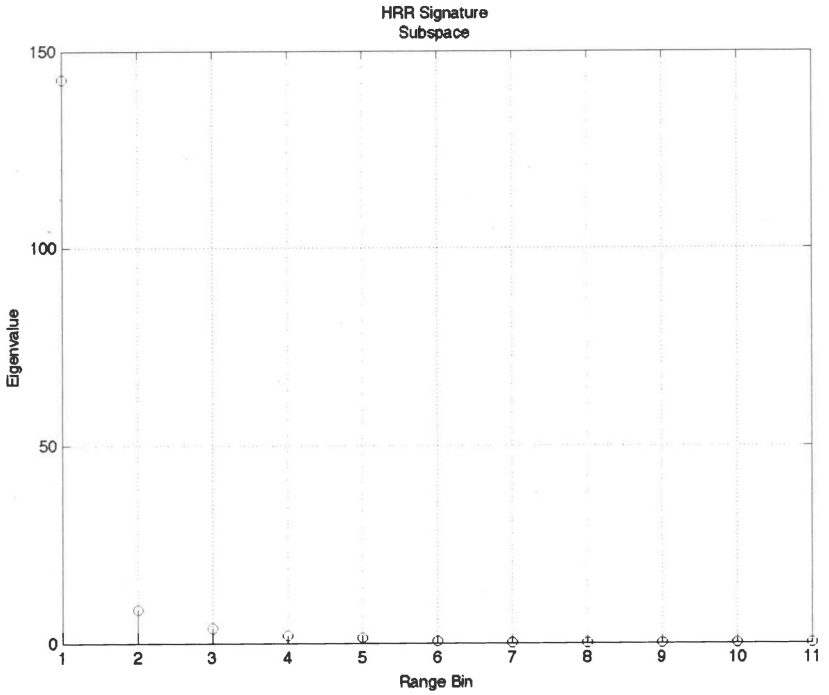

Figure 75: 10 Angularly Selective Targets Signal Subspace (Full)

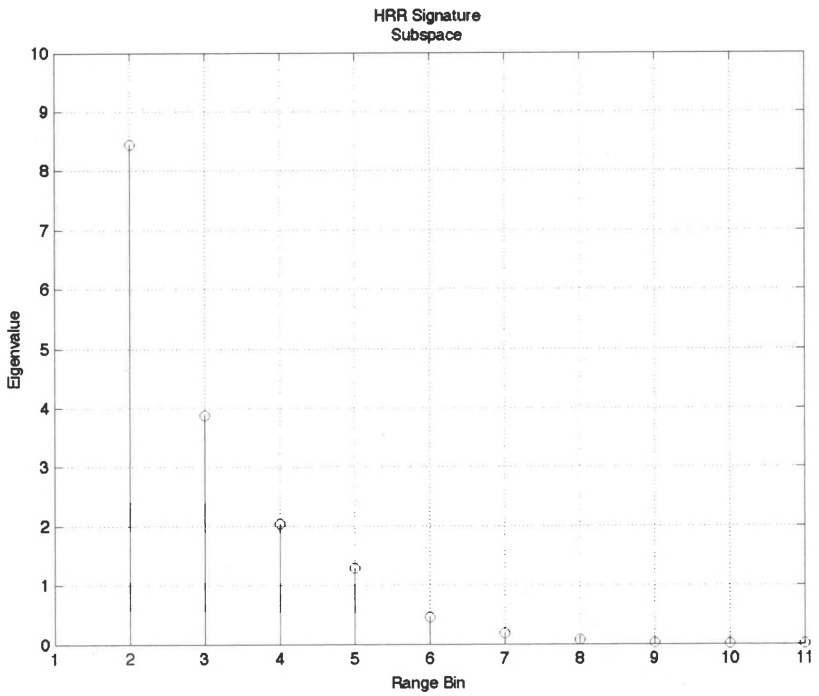

Figure 76: 10 Angularly Selective Targets Signal Subspace (Zoomed)

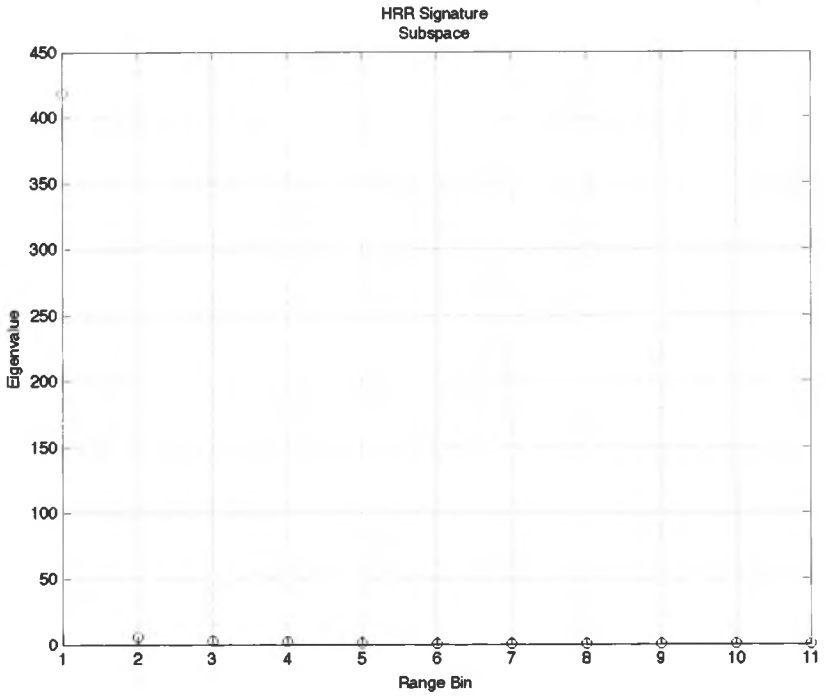

Figure 77: 50 Angularly Selective Targets Signal Subspace (Full)

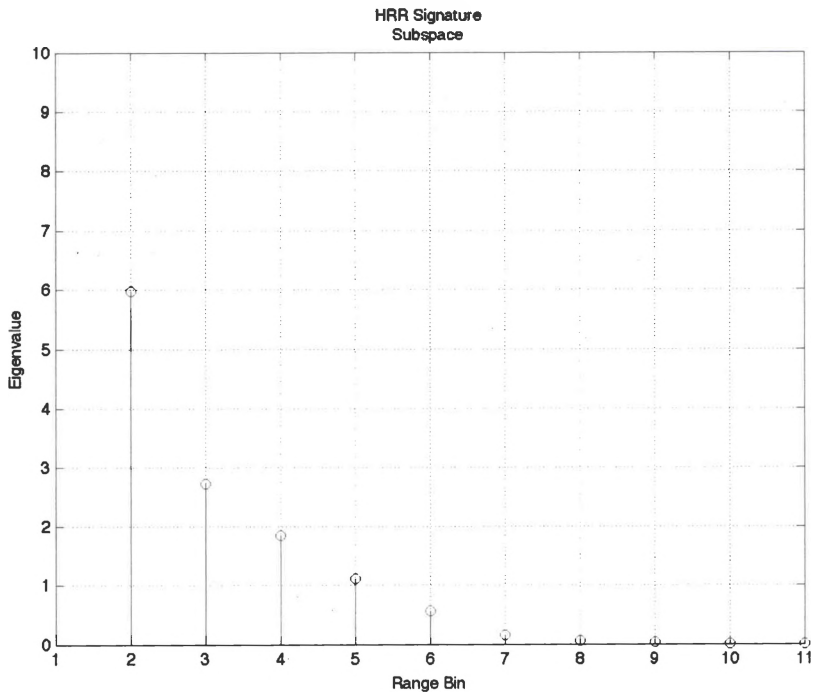

Figure 78: 50 Angularly Selective Targets Signal Subspace (Zoomed)

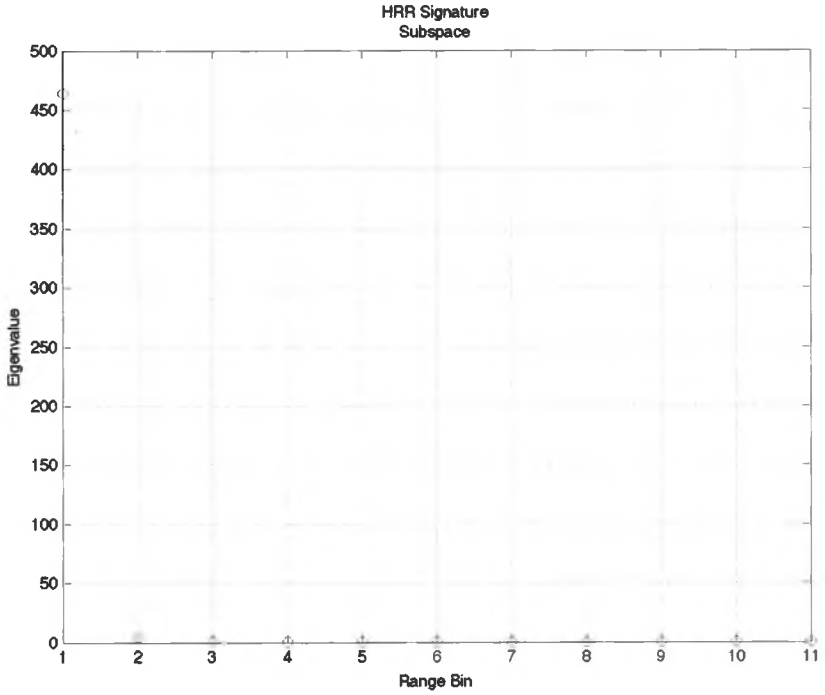

Figure 79: 100 Angularly Selective Targets Signal Subspace (Full)

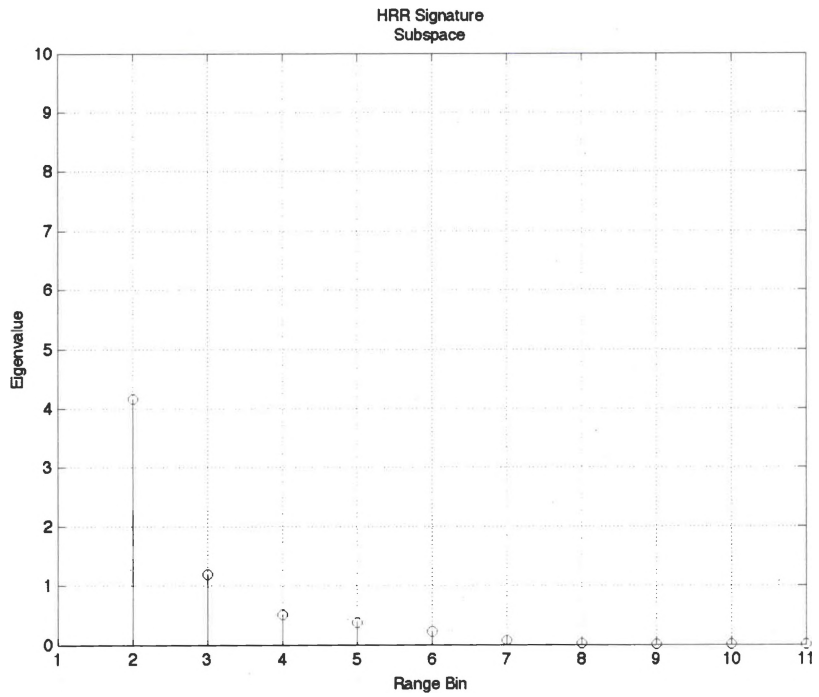

Figure 80: 100 Angularly Selective Targets Signal Subspace (Zoomed)

Range Bin	Eigenvalue			
	1	10	50	100
1	79.3990	142.7457	418.6269	463.9496
2	5.2506	8.449	5.9753	4.1676
3	3.5222	3.8748	2.7333	1.1965
4	1.7615	2.0378	1.8525	0.5115
5	1.2711	1.2892	1.1073	0.3683
6	0.4813	0.4524	0.5701	0.2271
7	0.1719	0.1773	0.1548	0.0683
8	0.0801	0.0738	0.0630	0.0208
9	0.0223	0.0269	0.0309	0.0056
10	0.0098	0.0070	0.0093	0.0012
11	0.0025	0.0025	0.0017	0.0004

Figure 81: Angularly Selective Eigenvalue Table

Frequency Selective Target (BW = 100 MHz)

In contrast to the specular case, the frequency selective target signal subspace (figures 82-90) has a decreasing maximum eigenvalue as the number of selective targets increases. This is an expected result, as the effect of the time-domain smearing of the frequency selective discretes becomes more prominent. What is surprising is just how similar the smaller eigenvalues are, relatively, in relation to the specular case. This would indicate that for the case of several target discretes that aside from the principal eigenvalue, there is no discernible difference in the signal subspace of the two cases.

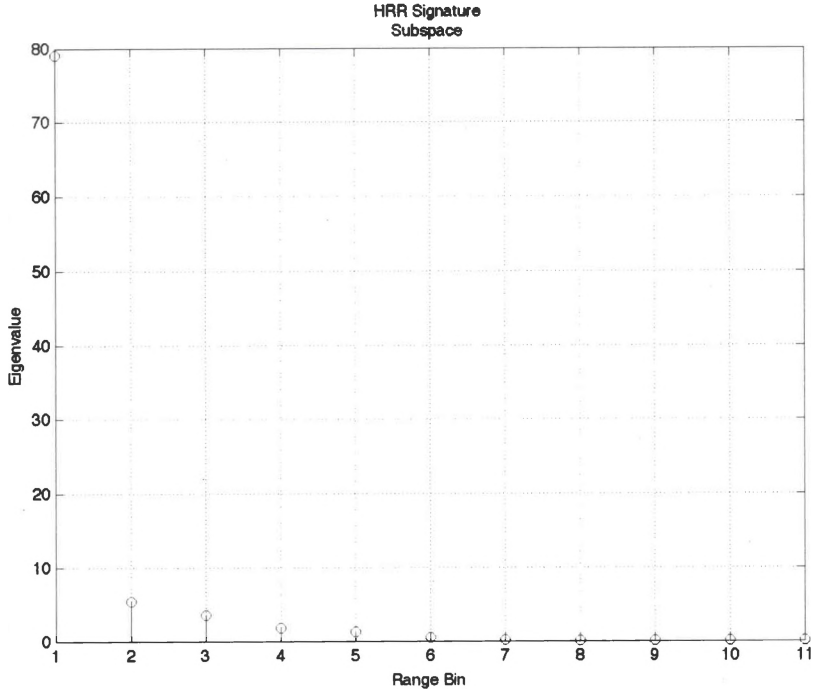

Figure 82: 1 Frequency Selective Target (100 MHz) Signal Subspace (Full)

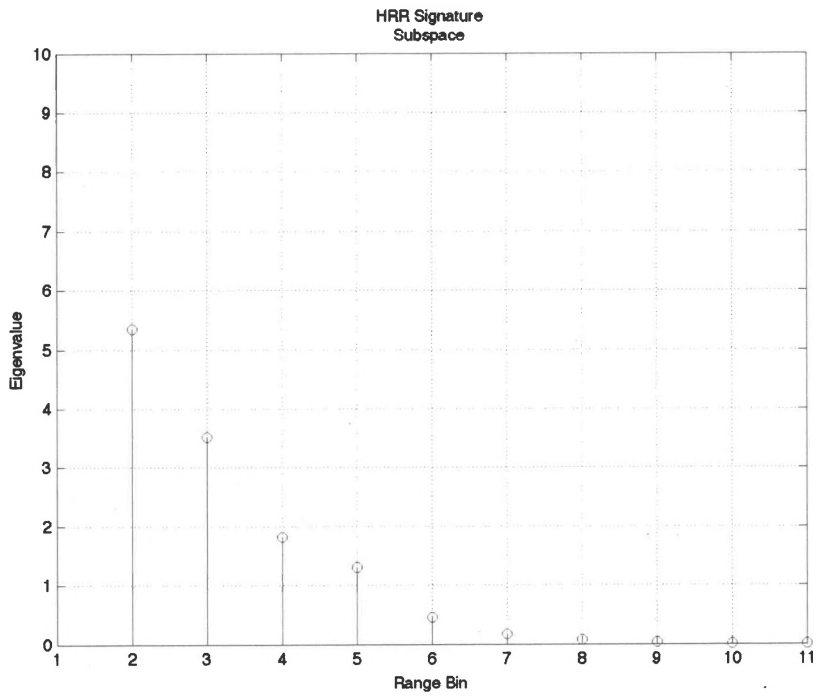

Figure 83: 1 Frequency Selective Target (100 MHz) Signal Subspace (Zoomed)

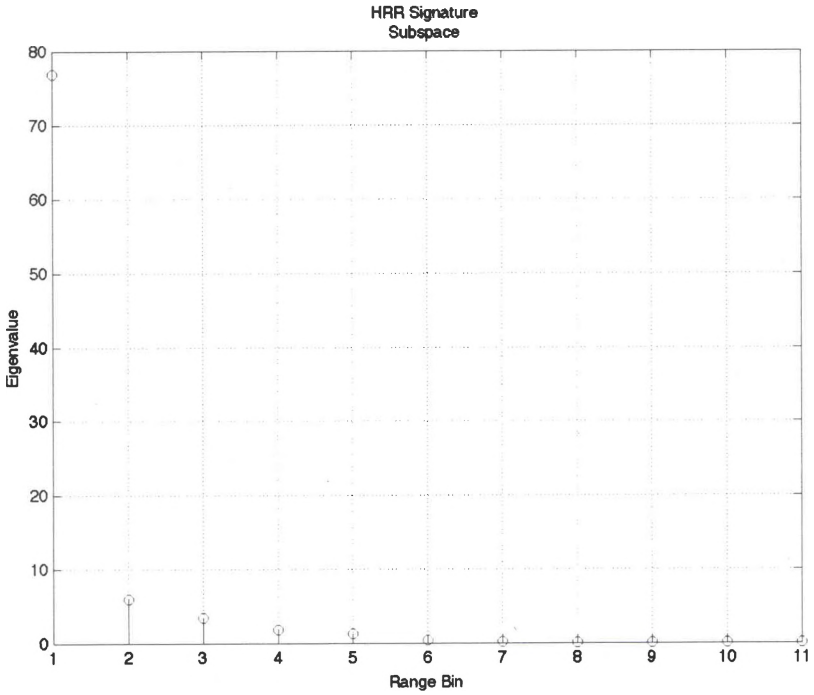

Figure 84: 10 Frequency Selective Targets (100 MHz) Signal Subspace (Full)

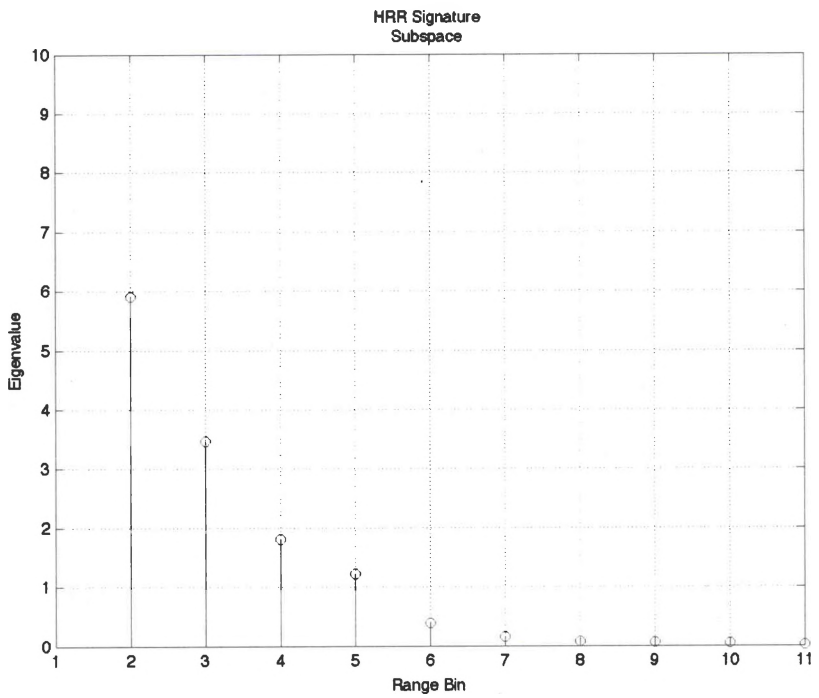

Figure 85: 10 Frequency Selective Targets (100 MHz) Signal Subspace (Zoomed)

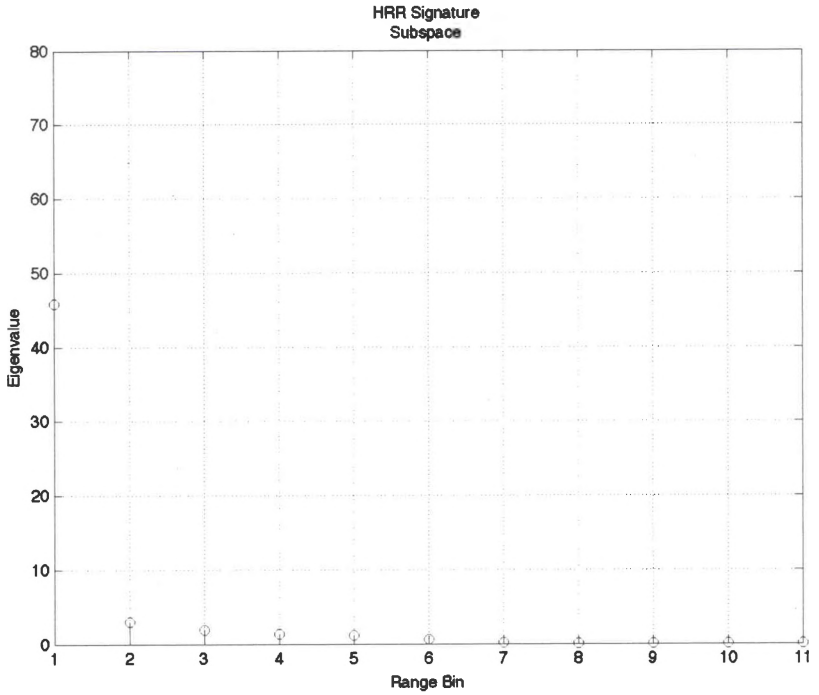

Figure 86: 50 Frequency Selective Targets (100 MHz) Signal Subspace (Full)

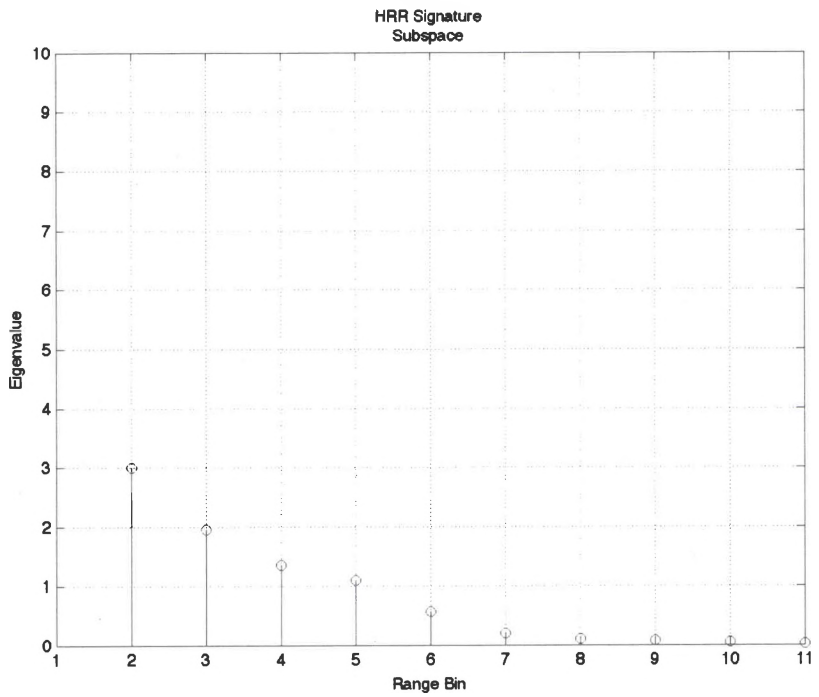

Figure 87: 50 Frequency Selective Targets (100 MHz) Signal Subspace (Zoomed)

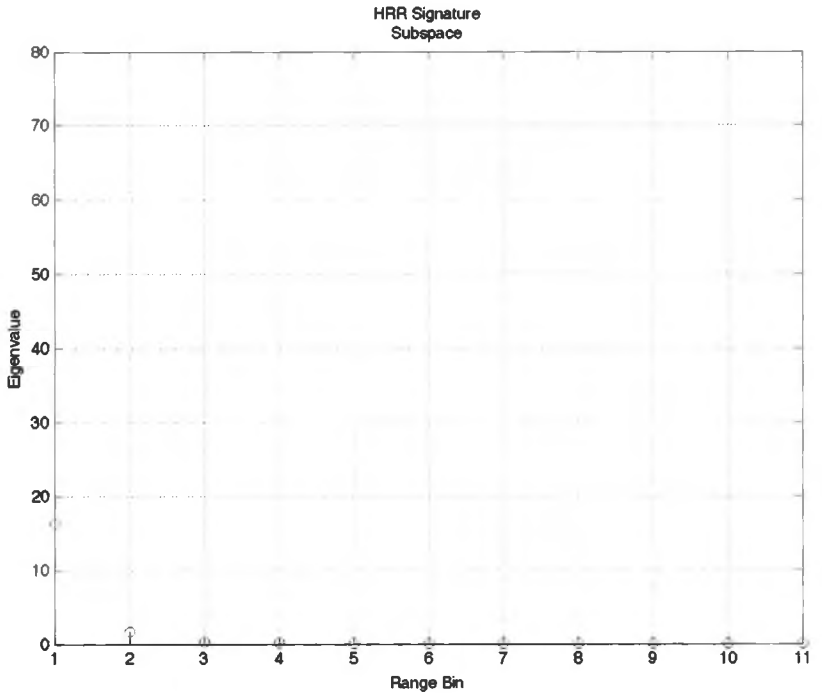

Figure 88: 100 Frequency Selective Targets (100 MHz) Signal Subspace (Full)

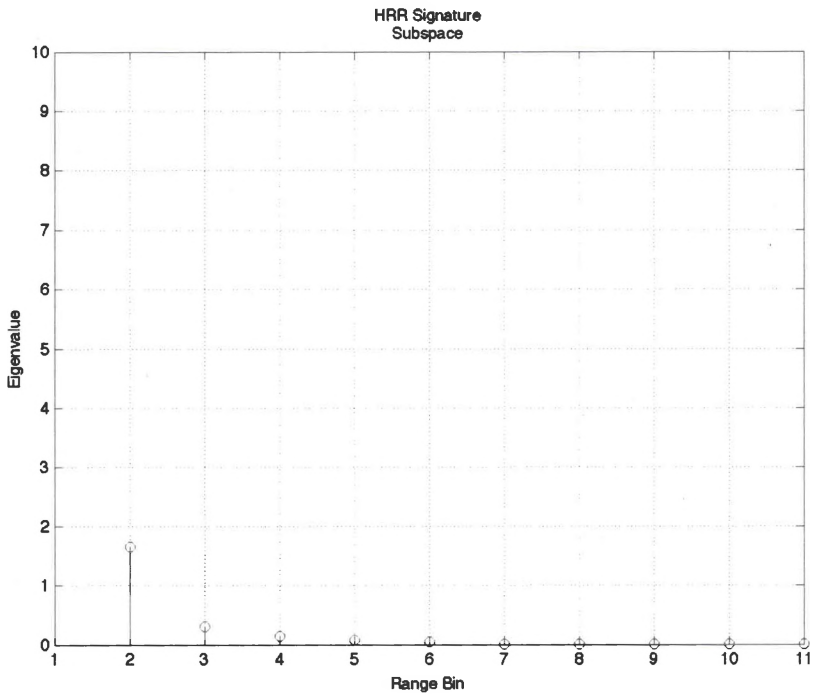

Figure 89: 100 Frequency Selective Targets (100 MHz) Signal Subspace (Zoomed)

Range Bin	Eigenvalue			
	1	10	50	100
1	79.0340	76.9204	45.8605	16.2624
2	5.3459	5.9039	3.0068	1.6588
3	3.5186	3.4627	1.9610	0.3059
4	1.8218	1.7988	1.3574	0.1465
5	1.3023	1.2222	1.0976	0.0696
6	0.4621	0.3884	0.5713	0.0427
7	0.1638	0.1502	0.1978	0.0131
8	0.0744	0.0800	0.1086	0.0085
9	0.0290	0.0608	0.0771	0.0014
10	0.0121	0.0411	0.0476	0.0004
11	0.0064	0.0252	0.0142	0.0002

Figure 90: Frequency Selective (100 MHz) Eigenvalue Table

Frequency Selective Target (BW = 1000 MHz)

The eigenvalues of the signal subspace representation (figures 91-99) of the frequency selective target case (BW = 1000 MHz) are nearly identical to those of the previous case, where the frequency selective bandwidth was 100 MHz. This is not a surprising result, as the effect of the frequency selective reflectivity is a smearing of the point-spread function following transformation from the frequency to the time-domain; and after scaling, the range-domain. This signifies the difficulty in determining the bandwidth of the frequency selective target reflectivity, in addition to, finding a salient feature set in which to test against for identification.

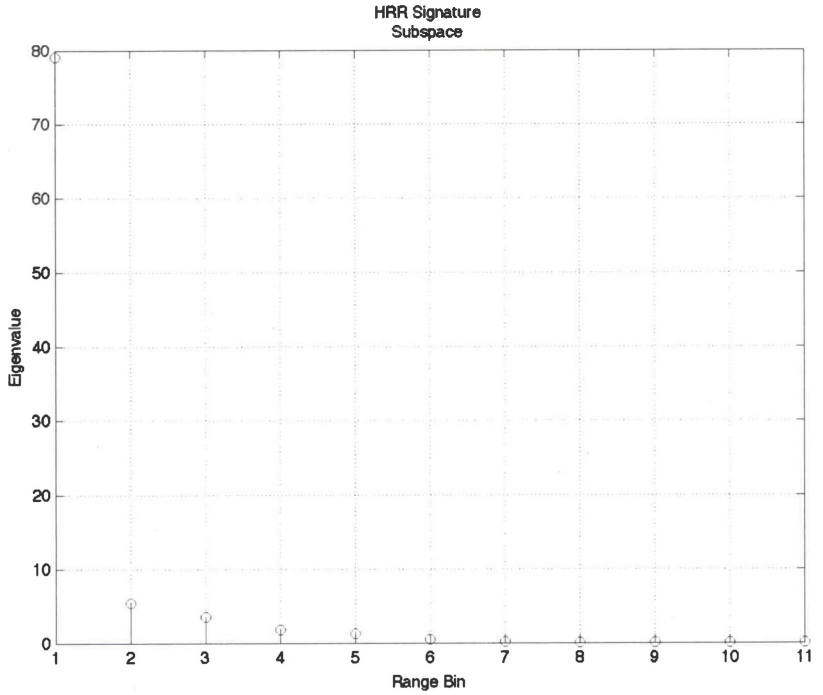

Figure 91: 1 Frequency Selective Target (1000 MHz) Signal Subspace (Full)

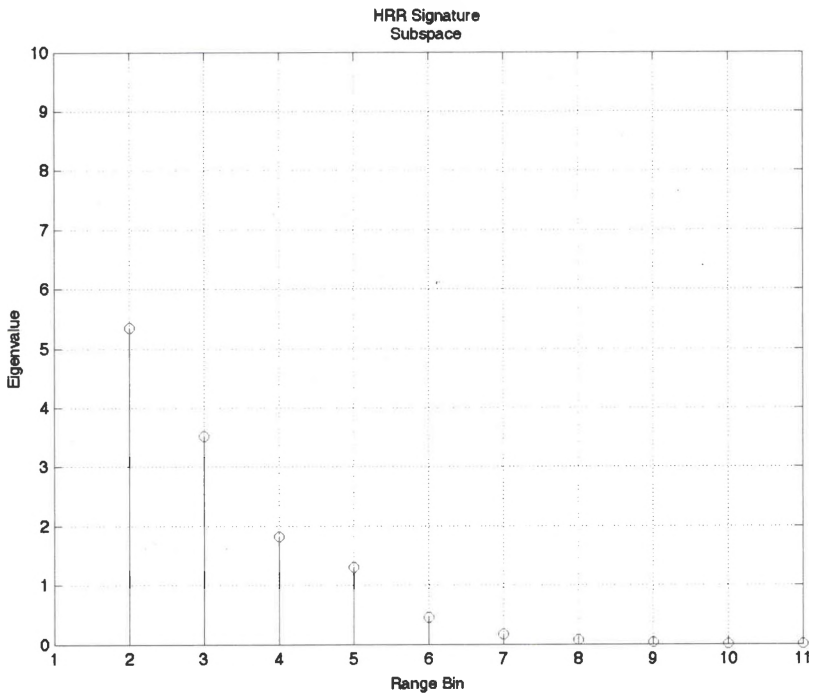

Figure 92: 1 Frequency Selective Target (1000 MHz) Signal Subspace (Zoomed)

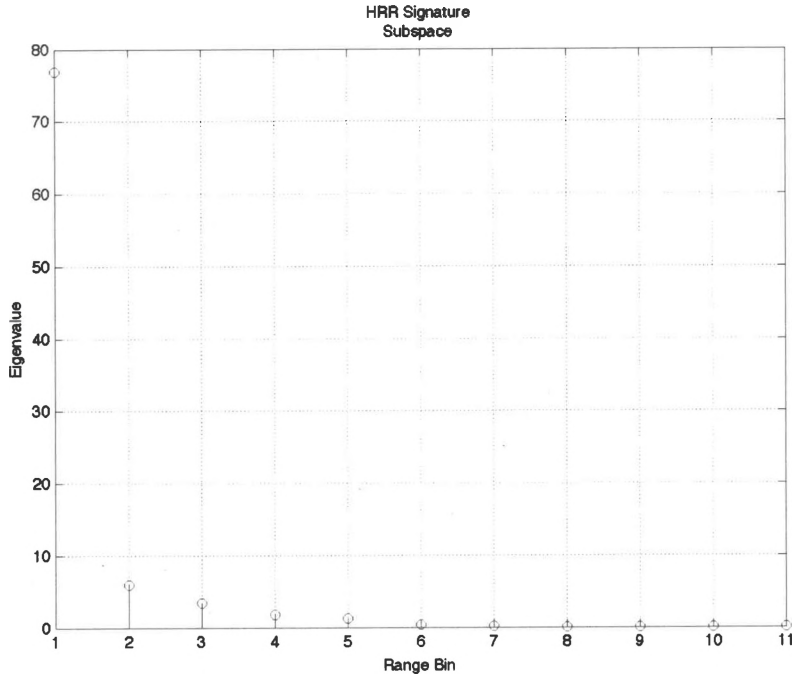

Figure 93: 10 Frequency Selective Targets (1000 MHz) Signal Subspace (Full)

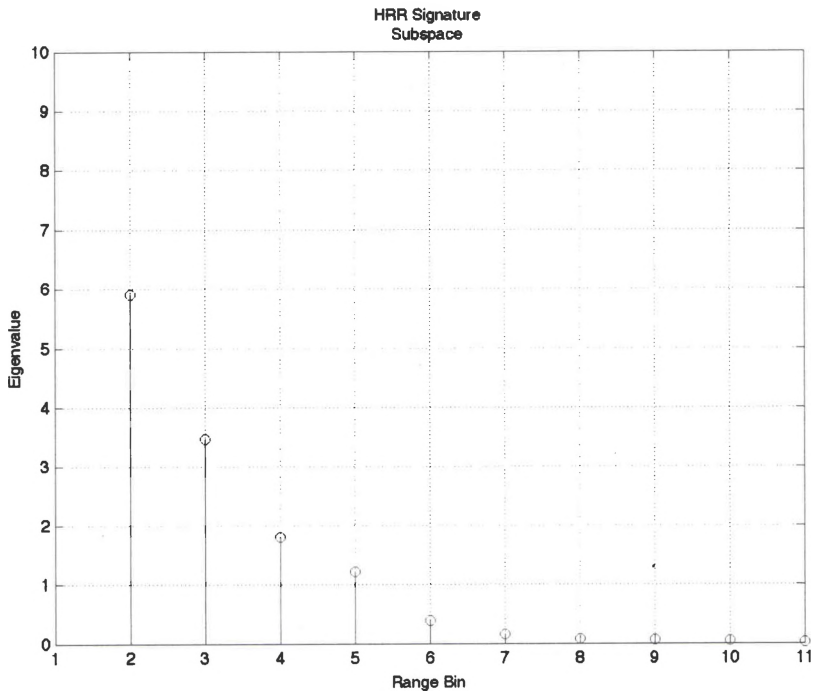

Figure 94: 10 Frequency Selective Targets (1000 MHz) Signal Subspace (Zoomed)

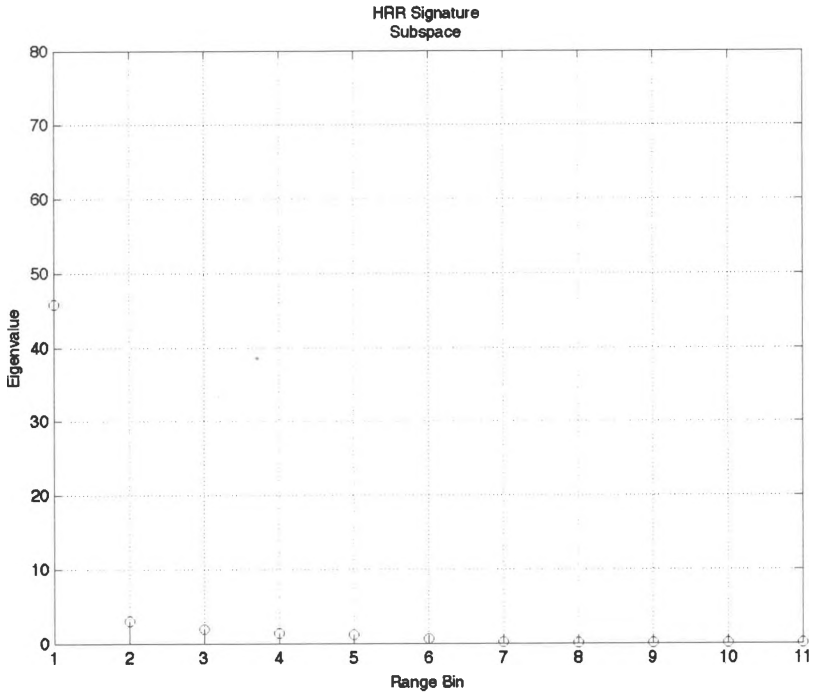

Figure 95: 50 Frequency Selective Targets (1000 MHz) Signal Subspace (Full)

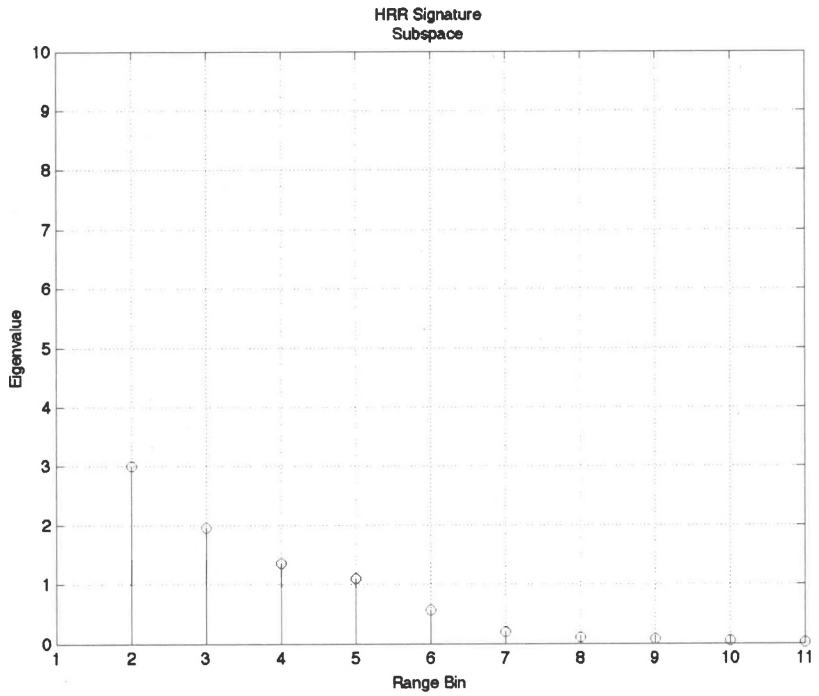

Figure 96: 50 Frequency Selective Targets (1000 MHz) Signal Subspace (Zoomed)

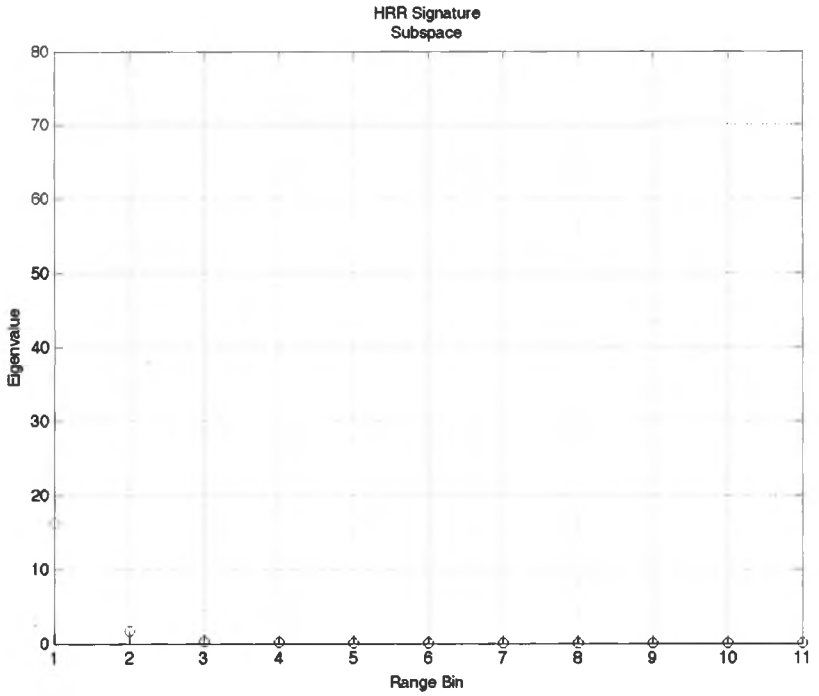

Figure 97: 100 Frequency Selective Targets (1000 MHz) Signal Subspace (Full)

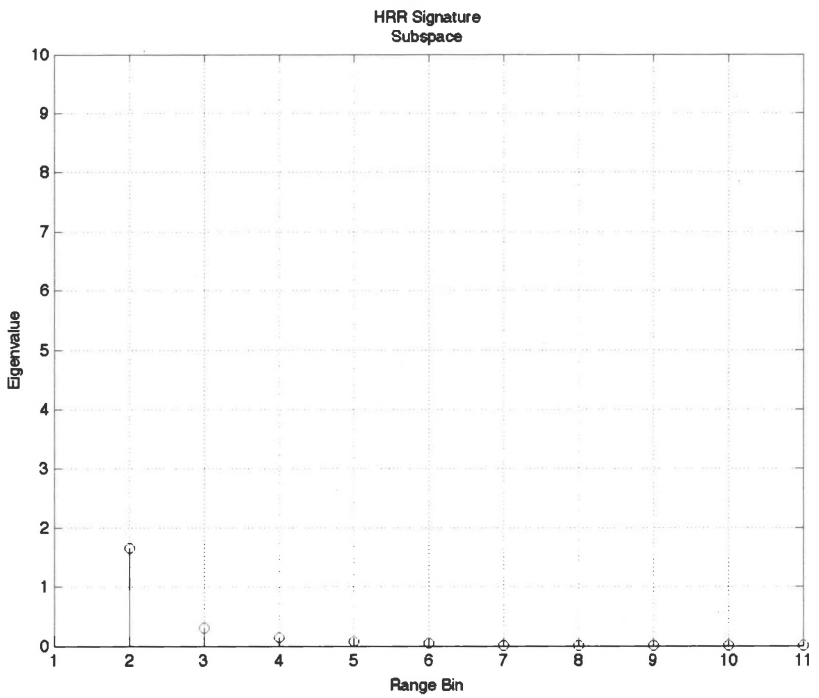

Figure 98: 100 Frequency Selective Targets (1000 MHz) Signal Subspace (Zoomed)

Range Bin	Eigenvalue			
	1	10	50	100
1	79.0340	76.9204	45.8608	16.2633
2	5.3459	5.9039	3.0068	1.6590
3	3.5186	3.4627	1.9610	0.3059
4	1.8218	1.7988	1.3575	0.1465
5	1.2023	1.2222	1.0976	0.0696
6	0.4621	0.3884	0.5713	0.0427
7	0.1638	0.1502	0.1978	0.0131
8	0.0744	0.0800	0.1086	0.0085
9	0.0290	0.0608	0.0771	0.0014
10	0.121	0.0411	0.0476	0.0004
11	0.0064	0.0252	0.0142	0.0002

Figure 99: Frequency Selective Target (1000 MHz) Eigenvalue Table

Section 4.8-Summary Remarks

In this chapter the testing results were presented and explanatory notes were provided to aid in the understanding of phenomenology observable in 2-D, 3-D and signal subspace plots. Essential supplementary theory was provided to aid in the understanding of the testing methodology. Chapter 5 will detail the conclusions of the testing regime and the significance on linear-frequency modulation derived high-range resolution signatures for target identification.

CHAPTER 5

SUMMARY AND CONCLUSIONS

Section 5.1-Summary of Problem

Chapter 1 detailed the problem, motivation and subsequent importance of the interference effects in the linear-frequency modulation (LFM) derived high-range resolution (HRR) signature. Chapter 2 covered essential theory, introduced the concept of the point-spread function and demonstrated the basic operation of the HRR algorithm. Chapter 3 presented testing methodology along with an introduction to the point-spread function, in detail. Chapter 4 presented the results of the testing and consideration was given to angular and frequency selective target discretes. The explanation of the HRR phenomenology study is the subject of the present chapter.

Section 5.2-Summary of Results

Having verified the operation of the high-range resolution (HRR) algorithm on both experimental data (section 2.7-2.9, 4.3), range bin statistics (section 4.4), and data generated from X-Patch (section 4.2), the signatures and signal subspaces of targets modeled by a collection of scattering centers exhibiting

varying degrees of selectivity in angle and frequency were examined. Starting with the idealized planar target structure having uniform reflectivity profile as the baseline test case, target discretes were given either angular or frequency selectivity. For the case of an extended target exhibiting specular target discretes, the effects on the HRR signature and signal subspace were both visible. When there were sufficient numbers of specular scattering centers, then the signal subspace principal eigenvalue increased dramatically; however the remainder of the eigenvalues dropped considerably from the case of 1 specular scattering center. In the instance of an extended target exhibiting frequency selectivity, the differences in selectivity bandwidth were found to be negligible.

However, with an increase in the number of scattering centers having a frequency selective reflectivity, the eigenvalues decreased proportionally. This phenomena is most noticeable in the case of 50 or more frequency selective scattering centers. Indeed, upon the inclusion of 100 scattering centers exhibiting frequency selectivity, the principal eigenvalue is less than 25% in value, while the mode of the signal subspace decreases by a factor of 3. Thus, the more scattering centers exhibiting frequency selectivity, the more noise that was introduced into the HRR signature. This can be viewed as the point-spread function being smeared by the Gaussian profile of the frequency selective scattering center. The extent of this smearing phenomena is determined by the bandwidth of frequency selectivity of the scattering center. As the individual point-spread functions are modified by Gaussian shape of the scattering

mechanism, they broaden. This broadening exacerbates the constructive interefence already occurring during the HRR signature process.

A similar result was shown for the angularly selective scattering center reflectivity profile; except that the principal eigenvalues increase proportionally. Non-principal eigenvalues follow the trend observed in the frequency selective scattering center case, and thus decrease in value proportional to the number of angularly selective scattering centers. This can be viewed as an increase in noise in the signal subspace. Noise is introduced when the flash associated with the specular scattering centers appear; giving rise to a scatterer response with a strong amplitude. These large scatterer responses spill over into adjacent range bins, which results in obfuscation of the neighboring individual scattering center responses. A number of these scattering centers exhibiting strong amplitudes exacerbate the constructive interference occurring within each range bin.

Section 5.3-Conclusion

The topic of the linear-frequency (LFM) modulated high-range resolution (HRR) signature interference phenomena was examined within the framework of scattering center angular and frequency selectivity. Range bin statistics, experimental and generated data sets verified operation of the HRR algorithm. Subjective and objective testing methodologies showed the effects of the interference phenomena on the LFM derived HRR signature. The results of chapter 4 showed the difficulty in characterizing the deleterious effects of target

selectivity on both the HRR signature and the accompanying signal subspace. The notion of salient feature-sets, for use in target identification, was introduced and found to be an artifact of the constructive and destructive interference summation of the individual point-spread functions present in individual range bins. The effect of a bandlimited signal in the frequency domain is an point spread function with infinite extent in the time or range-domains. This means there is signal (defined as signal plus interference plus noise) in all range bins, even though the samples were taken once per range bin. This interference phenomena makes difficult, the task of determining the particular range bin for which the angular or frequency selectivity is emanating. Hence, while peaks may be present within a given LFM derived signature, there is difficulty in associating peaks with any specific or characteristic scattering mechanism taking place on the target. Each peak is really the result of a constructive interference of a number of differing scattering phenomena taking place, in that particular range bin. As such, there is usually a considerable variation in the strength of the peak.

APPENDIX 1

LFM RECEIVED SIGNAL FROM THE K^{TH} SCATTERER

Appendix 1.A-Expansion and Simplification of Quadratic Term

From equation 2.80, we have,

$$y_k(\tilde{t},l)\exp\Big(j\Big[2\pi f_0\big(\tilde{t}-\tau_0-\tilde{T}_k(t)\big)+\gamma\big(\tilde{t}-\tau_0-\tilde{T}_k(t)\big)^2\Big]\ldots \\ -j\Big[2\pi f_0\big(\tilde{t}-\tau_0\big)+\gamma\big(\tilde{t}-\tau_0\big)^2\Big]\Big) \tag{1.A.1}$$

Let,

$$A=\exp\Big(j\Big[2\pi f_0\big(\tilde{t}-\tau_0-\tilde{T}_k(t)\big)\Big]-j\Big[2\pi f_0\big(\tilde{t}-\tau_0\big)\Big]\Big) \tag{1.A.2}$$

and,

$$B=\exp\Big(j\Big[\gamma\big(\tilde{t}-\tau_0-\tilde{T}_k(t)\big)^2\Big]-j\Big[\gamma\big(\tilde{t}-\tau_0\big)^2\Big]\Big). \tag{1.A.3}$$

Simplifying A yields,

$$A=\exp\Big(j\Big[2\pi f_0\big(\tilde{t}-\tau_0-\tilde{T}_k(t)\big)\Big]-j\Big[2\pi f_0\big(\tilde{t}-\tau_0\big)\Big]\Big) \tag{1.A.4}$$

$$A=\exp\Big(j2\pi f_0\big[\tilde{t}-\tau_0-T_k(t)-\tilde{t}+\tau_0\big]\Big) \tag{1.A.5}$$

$$A=\exp\big(-j2\pi f_0T_k(t)\big). \tag{1.A.6}$$

Simplifying B yields,

$$B=\exp\Big(j\Big[\gamma\big(\tilde{t}-\tau_0-\tilde{T}_k(t)\big)^2\Big]-j\Big[\gamma\big(\tilde{t}-\tau_0\big)^2\Big]\Big) \tag{1.A.7}$$

$$B=\exp\Big(j\gamma\Big[\tilde{t}^2-\tilde{t}\tau_0-\tilde{t}\tilde{T}_k(t)-\tau_0\tilde{t}+\tau_0^2+\tau_0\tilde{T}_k(t)\ldots \\ -\tilde{t}\tilde{T}_k(t)+\tau_0\tilde{T}_k(t)+\tilde{T}_k^2(t)-\tilde{t}^2+\tilde{t}\tau_0+\tilde{t}\tau_0-\tau_0^2\Big]\Big) \tag{1.A.8}$$

$$B=\exp\Big(j\gamma\Big[\tilde{T}_k^2(t)-2\tilde{t}\tilde{T}_k(t)+2\tau_0\tilde{T}_k(t)\Big]\Big) \tag{1.A.9}$$

$$B=\exp\Big(j\gamma\Big[\tilde{T}_k^2(t)+2\big(\tau_0-\tilde{t}\big)\tilde{T}_k(t)\Big]\Big). \tag{1.A.10}$$

Combining A and B yields,

$$AB = \exp\left(-j2\pi f_0 T_k(t)\right)\exp\left(j\gamma\left[\tilde{T}_k^{\,2}(t) + 2\left(\tau_0 - \tilde{t}\right)\tilde{T}_k(t)\right]\right). \qquad \text{(1.A.11)}$$

Let $\tilde{T}_k(t) = \dfrac{2\tilde{R}_k(t)}{c}$,

$$\therefore AB = \exp\left(-j2\pi f_0 \frac{2\tilde{R}_k(t)}{c}\right)\exp\left(j\gamma\left[\frac{4\tilde{R}_k^{\,2}(t)}{c^2} + \left(\tau_0 - \tilde{t}\right)\frac{4\tilde{R}_k(t)}{c}\right]\right). \qquad \text{(1.A.12)}$$

Appendix 1.B-Expansion of the LFM Quadratic Term

Let, $R_k(t) = R_k - R_0 + V_k t$, thus,

$$\exp\left(j\frac{4\gamma R_k{}^2(t)}{c^2} \right) = \exp\left(j\frac{4\gamma\left[R_k - R_0 + V_k t\right]^2}{c^2} \right). \tag{1.B.1}$$

Let,

$$A = \exp\left(j\frac{4\gamma\left[R_k - R_0 + V_k t\right]^2}{c^2} \right). \tag{1.B.2}$$

Therefore,

$$A = \exp\left(j\frac{4\gamma\left[R_k{}^2 - R_0 R_k + R_k V_k t - R_0 R_k + R_0{}^2 \cdots \right.\right.}{c^2} \left.\left. \frac{-R_0 V_k t + R_k V_k t - R_0 V_k t + V_k{}^2 t^2}{c^2} \right] \right) \tag{1.B.3}$$

Following simplification,

$$A = \exp\left(j\frac{4\gamma\left(R_k - R_0\right)^2}{c^2} \right) \exp\left(j\frac{4\gamma\left(R_k - R_0\right)2V_k t}{c} \right) \exp\left(j\frac{4\gamma V_k{}^2 t^2}{c^2} \right). \tag{1.B.4}$$

Thus,

$$\therefore A = \exp\left(j\frac{4\gamma\left(R_k - R_0\right)^2}{c^2} \right) \exp\left(j\frac{8\gamma\left(R_k - R_0\right)V_k t}{c} \right) \exp\left(j\frac{4\gamma V_k{}^2 t^2}{c^2} \right). \tag{1.B.5}$$

Appendix 1.C-LFM Approximation Analysis of Quadratic Terms

Let,

$$A = \exp\left(j\frac{8\gamma(R_k - R_0)V_k t}{c^2} \right) \tag{1.C.1}$$

$$B = \exp\left(-j\frac{2R_k(t)}{c}\left(2\pi f_0 + 2\gamma(\tilde{t} - \tau_0)\right) \right). \tag{1.C.2}$$

Let, $R_k(t) = R_k - R_0 + V_k t$,

$$B = \exp\left(-j\frac{2(R_k - R_0 + V_k t)}{c}\left(2\pi f_0 + 2\gamma(\tilde{t} - \tau_0)\right) \right). \tag{1.C.3}$$

Thus,

$$B = \exp\left(-j\frac{2(R_k - R_0 + V_k(\tilde{t} - lT))}{c}\left(2\pi f_0 + 2\gamma(\tilde{t} - \tau_0)\right) \right). \tag{1.C.4}$$

Let, $t = \tilde{t} - lT$,

$$\begin{aligned} B = \exp&\left(-j\frac{2(R_k - R_0)}{c}\left(2\pi f_0 + 2\gamma(\tilde{t} + \tau_0)\right) \right)\cdots \\ &\exp\left(-j\frac{2V_k(\tilde{t} - lT)}{c}\left(2\pi f_0 + 2\gamma(\tilde{t} + \tau_0)\right) \right) \end{aligned} \tag{1.C.5}$$

Let, $t = \tilde{t} - lT$,

$$A = \exp\left(j\frac{8\gamma(R_k - R_0)V_k(\tilde{t} - lT)}{c^2} \right) . \tag{1.C.6}$$

Thus,

$$\begin{aligned} AB = \exp&\left(j\frac{8\gamma(R_k - R_0)V_k(\tilde{t} - lT)}{c^2} \right)\exp\left(-j\frac{2(R_k - R_0)}{c}\left(2\pi f_0 + 2\gamma(\tilde{t} + \tau_0)\right) \right)\cdots \\ &\exp\left(-j\frac{2V_k(\tilde{t} - lT)}{c}\left(2\pi f_0 + 2\gamma(\tilde{t} + \tau_0)\right) \right) \end{aligned} \tag{1.C.7}$$

Appendix I.D-Explanation of Equation 2.87

Let,

$$A = \exp\left(-j\left(\frac{2(R_k - R_0)}{c}\left(2\pi f_0 + 2\gamma(\tilde{t} - \tau_0)\right)\right)\right) \tag{1.D.1}$$

$$B = \exp\left(-j\left(\frac{2V_k(\tilde{t} - lT)}{c}\left(2\pi f_0 + 2\gamma(\tilde{t} - \tau_0)\right)\right)\right) \tag{1.D.2}$$

$$C = \exp\left(j\left(\frac{8\gamma(R_k - R_0)V_k(\tilde{t} - lT)}{c^2}\right)\right). \tag{1.D.3}$$

Expansion of A,B, and C yields,

$$A = \exp\left(-j\left(\frac{2(R_k - R_0)}{c}\left(2\pi f_0 + 2\gamma(\tilde{t} - \tau_0)\right)\right)\right) \tag{1.D.4}$$

$$B = \exp\left(-j\left(\frac{4\pi(V_k\tilde{t}f_0 + V_k lT)}{c} + \ldots \right.\right. \\ \left.\left. \frac{4\gamma(V_k\tilde{t}^2 - V_k\tilde{t}\tau_0 + V_k lT\tilde{t} - V_k lT\tau_0)}{c}\right)\right) \tag{1.D.5}$$

$$C = \exp\left(j\left(\frac{8\gamma(R_k V_k\tilde{t} - R_k V_k lT - R_0 V_k\tilde{t} - R_0 V_k lT)}{c^2}\right)\right). \tag{1.D.6}$$

Substitution of $\lambda = c/f_0$ and $\tau_0 = 2R_0/c$ yields,

$$A = \exp\left(-j\left(\frac{4\pi R_k}{\lambda} - \frac{4\pi R_0}{\lambda} + \frac{4\gamma R_k\tilde{t}}{c} - \frac{8\gamma R_k R_0}{c^2} - \frac{4\gamma R_o\tilde{t}}{c} + \frac{8\gamma {R_0}^2}{c^2}\right)\right) \tag{1.D.7}$$

$$B = \exp\left(-j\left(\frac{4\pi V_k\tilde{t}}{\lambda} + \frac{4\pi V_k lT}{\lambda} + \frac{4\gamma V_k\tilde{t}}{c} - \frac{8\gamma V_k\tilde{t}R_0}{c^2} + \frac{4\gamma V_k lT\tilde{t}}{c} - \frac{8\gamma V_k lTR_0}{c^2}\right)\right) \tag{1.D.8}$$

$$C = \exp\left(j\left(\frac{8\gamma R_k V_k \tilde{t}}{c^2} + \frac{8\gamma R_k V_k lT}{c^2} - \frac{8\gamma R_0 V_k \tilde{t}}{c^2} - \frac{8\gamma R_0 V_k lT}{c^2} \right) \right). \tag{1.D.9}$$

Thus,

$$\begin{aligned} ABC = \exp\left(-j\frac{4\gamma\left(R_k - R_0\right)\tilde{t}}{c} \right) \exp\left(-j\left(\frac{4\pi V_k \tilde{t}}{\lambda} - \frac{8\gamma R_k V_k \tilde{t}}{c^2} \right) \right) \cdots \\ \exp\left(-j\frac{4\gamma V_k \tilde{t}^2}{c} \right) \exp\left(-j\left(\frac{4\pi V_k lT}{\lambda} - \frac{8\gamma R_k V_k lT}{c^2} \right) \right) \exp\left(-j\frac{4\gamma V_k lT\tilde{t}}{c} \right) \end{aligned} \tag{1.D.10}$$

APPENDIX 2

THE KOLMOGOROV-SMIRNOV HYPOTHESIS TESTING RESULTS

Appendix 2.A-Range Bin 1

Komolgorov-Smirnov Test Results

Confidence Level =
95.00

Backscattered E-Field: Mean of Real
0.01

Backscattered E-Field: Standard Deviation of Real
0.30

Backscattered E-Field: Mean of Imaginary
0.00

Backscattered E-Field: Standard Deviation of Imaginary
0.41

Backscattered E-Field: Null Hypothesis for Real
--Accepted--
Observed p-value, P = 0.402127
Observed Kolmogorov-Smirnov Statistic = 0.145519
The Cutoff Value for determining if the Kolmogorov-Smirnov Statistic is Significant = 0.221211

Backscattered E-Field: Null Hypothesis for Real
--Accepted--
Observed p-value, P = 0.673675
Observed Kolmogorov-Smirnov Statistic = 0.117689
The Cutoff Value for determining if the Kolmogorov-Smirnov Statistic is Significant = 0.221211

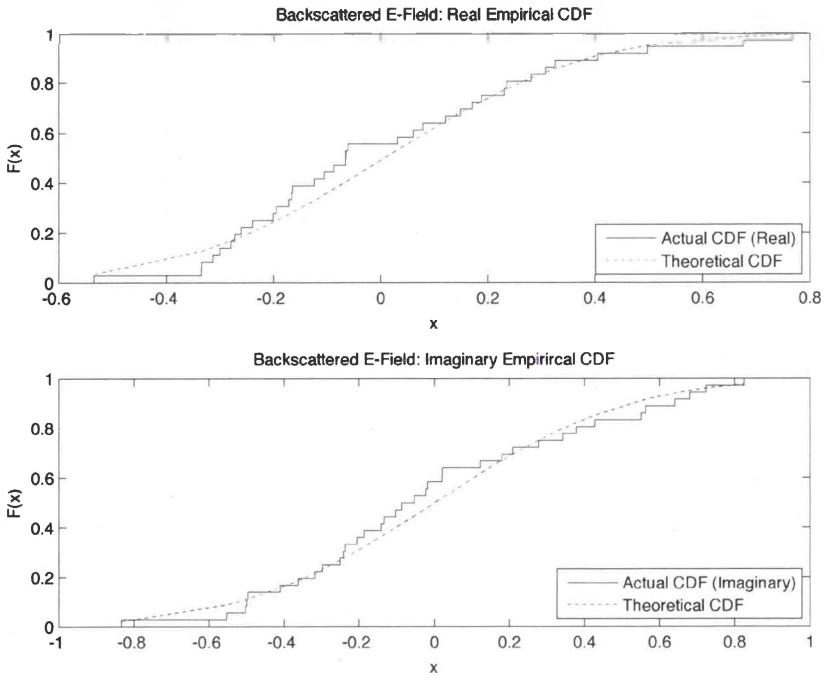

Figure 100: Kolmogorov-Smirnov CDFs

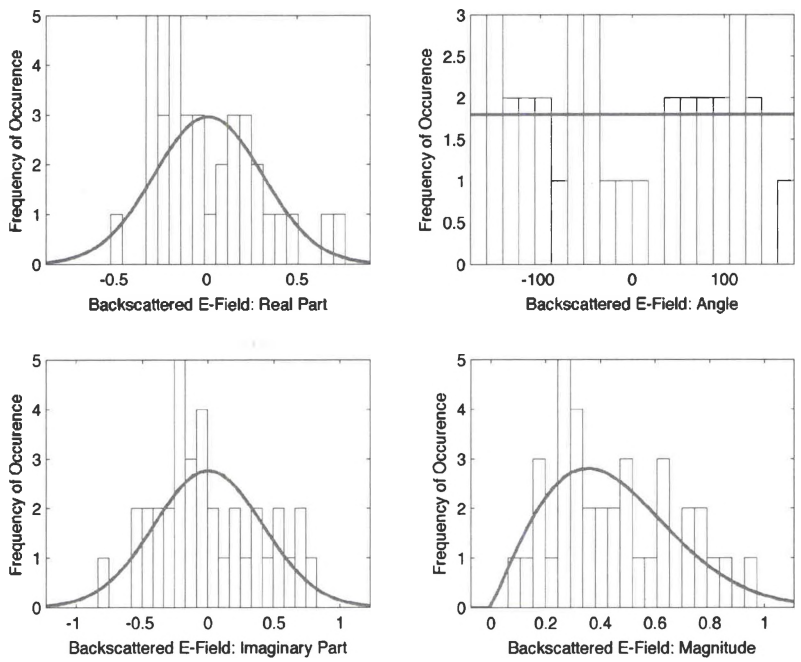

Figure 101: Backscattered E-Field Plots

Appendix 5.B-Range Bin 2

Komolgorov-Smirnov Test Results

Confidence Level =
95.00

Backscattered E-Field: Mean of Real
0.00

Backscattered E-Field: Standard Deviation of Real
0.43

Backscattered E-Field: Mean of Imaginary
-0.05

Backscattered E-Field: Standard Deviation of Imaginary
0.46

Backscattered E-Field: Null Hypothesis for Real
--Accepted--
Observed p-value, P = 0.658452
Observed Kolmogorov-Smirnov Statistic = 0.11916
The Cutoff Value for determining if the Kolmogorov-Smirnov Statistic is Significant = 0.221211

Backscattered E-Field: Null Hypothesis for Real
--Accepted--
Observed p-value, P = 0.92573
Observed Kolmogorov-Smirnov Statistic = 0.0891234
The Cutoff Value for determining if the Kolmogorov-Smirnov Statistic is Significant = 0.221211

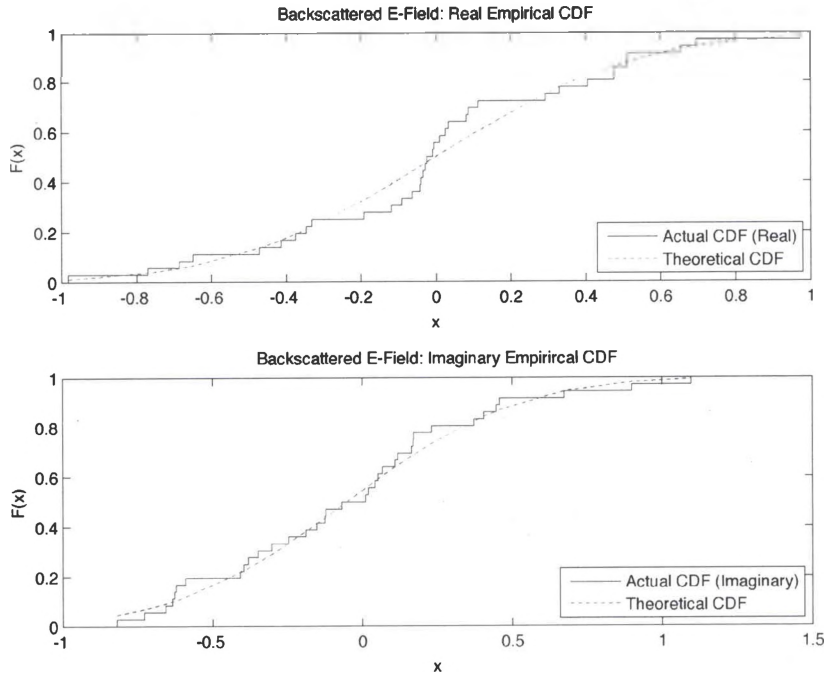

Figure 102: Kolmogorov-Smirnov CDFs

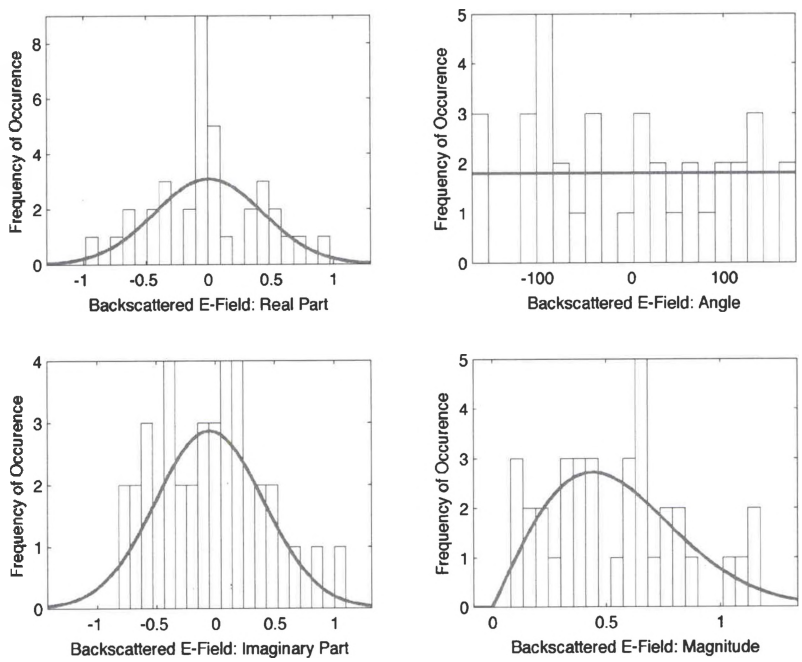

Figure 103: Backscattered E-Field Plots

Appendix 2.C-Range Bin 3

Komolgorov-Smirnov Test Results

Confidence Level =
95.00

Backscattered E-Field: Mean of Real
-0.03

Backscattered E-Field: Standard Deviation of Real
0.78

Backscattered E-Field: Mean of Imaginary
0.12

Backscattered E-Field: Standard Deviation of Imaginary
0.64

Backscattered E-Field: Null Hypothesis for Real
--Accepted--
Observed p-value, P = 0.939029
Observed Kolmogorov-Smirnov Statistic = 0.0867989
The Cutoff Value for determining if the Kolmogorov-Smirnov Statistic is Significant = 0.221211

Backscattered E-Field: Null Hypothesis for Real
--Accepted--
Observed p-value, P = 0.834118
Observed Kolmogorov-Smirnov Statistic = 0.101304
The Cutoff Value for determining if the Kolmogorov-Smirnov Statistic is Significant = 0.221211

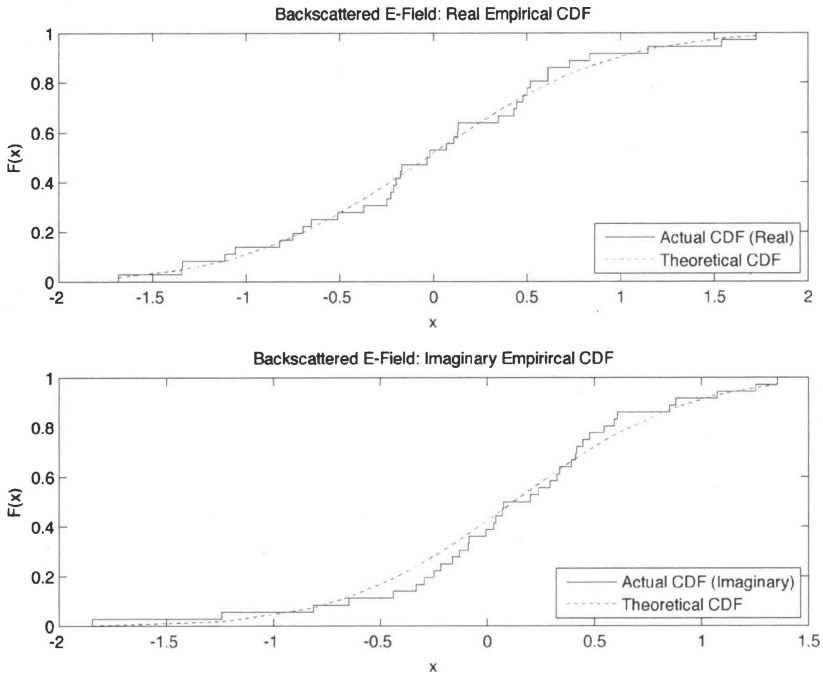

Figure 104: Kolmogorov-Smirnov CDFs

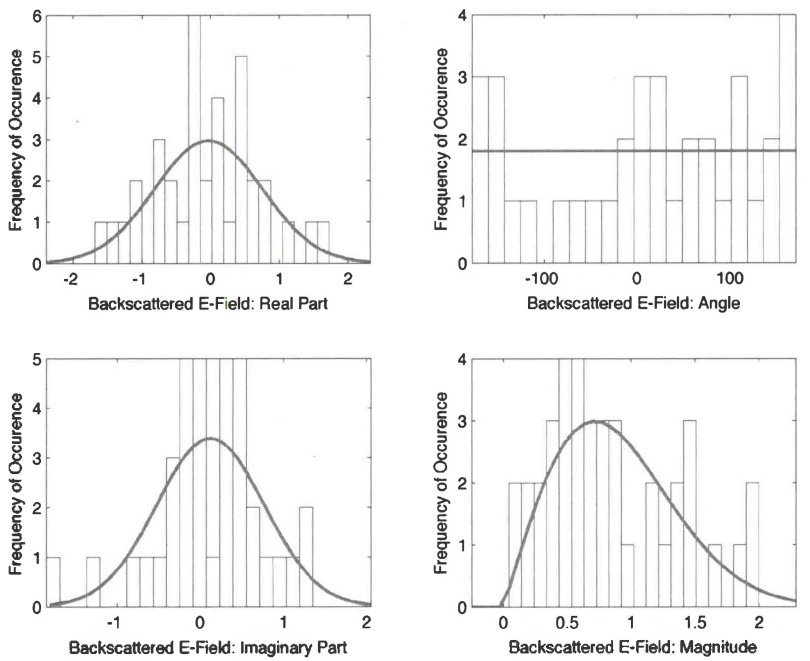

Figure 105: Backscattered E-Field Plots

Appendix 2.D-Range Bin 4

Komolgorov-Smirnov Test Results

Confidence Level =
95.00

Backscattered E-Field: Mean of Real
0.40

Backscattered E-Field: Standard Deviation of Real
1.91

Backscattered E-Field: Mean of Imaginary
-0.10

Backscattered E-Field: Standard Deviation of Imaginary
1.52

Backscattered E-Field: Null Hypothesis for Real
--Accepted--
Observed p-value, P = 0.742842
Observed Kolmogorov-Smirnov Statistic = 0.110917
The Cutoff Value for determining if the Kolmogorov-Smirnov Statistic is Significant = 0.221211

Backscattered E-Field: Null Hypothesis for Real
--Accepted--
Observed p-value, P = 0.968892
Observed Kolmogorov-Smirnov Statistic = 0.0801352
The Cutoff Value for determining if the Kolmogorov-Smirnov Statistic is Significant = 0.221211

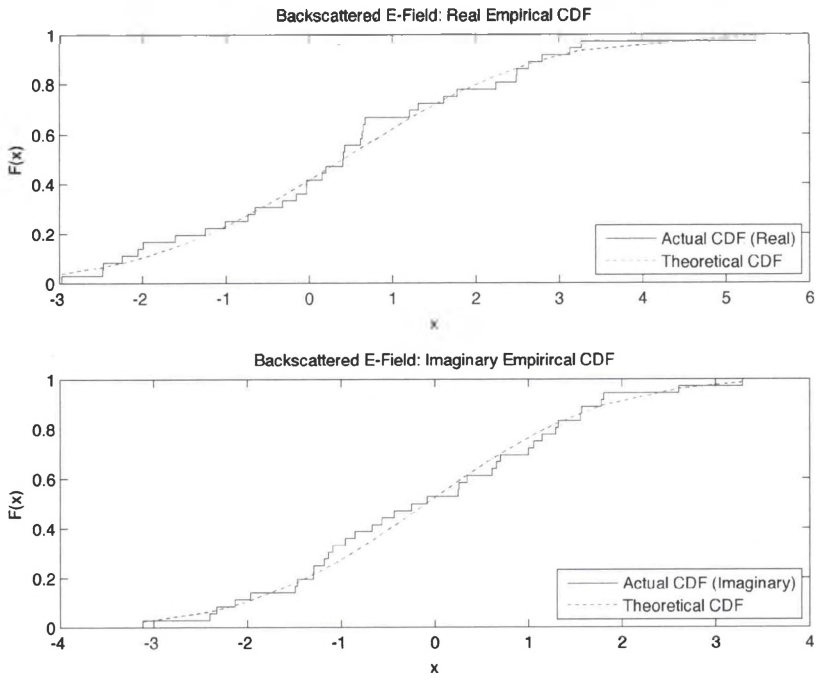

Figure 106: Kolmogorov-Smirnov CDFs

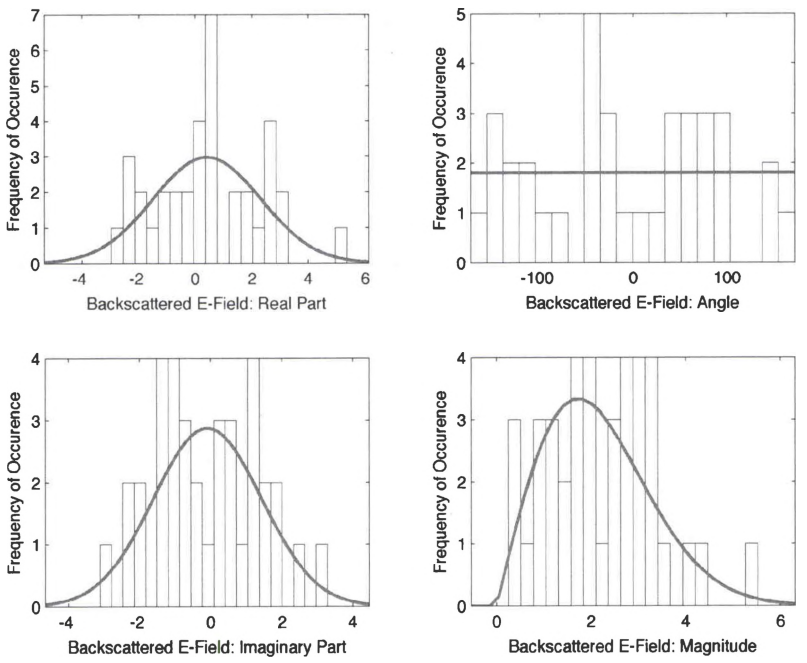

Figure 107: Backscattered E-Field Plots

Appendix 2.E-Range Bin 5

Komolgorov-Smirnov Test Results

Confidence Level =
95.00

Backscattered E-Field: Mean of Real
0.40

Backscattered E-Field: Standard Deviation of Real
3.58

Backscattered E-Field: Mean of Imaginary
0.40

Backscattered E-Field: Standard Deviation of Imaginary
2.74

Backscattered E-Field: Null Hypothesis for Real
--Accepted--
Observed p-value, P = 0.998776
Observed Kolmogorov-Smirnov Statistic = 0.0617216
The Cutoff Value for determining if the Kolmogorov-Smirnov Statistic is Significant = 0.221211

Backscattered E-Field: Null Hypothesis for Real
--Accepted--
Observed p-value, P = 0.874035
Observed Kolmogorov-Smirnov Statistic = 0.0965271
The Cutoff Value for determining if the Kolmogorov-Smirnov Statistic is Significant = 0.221211

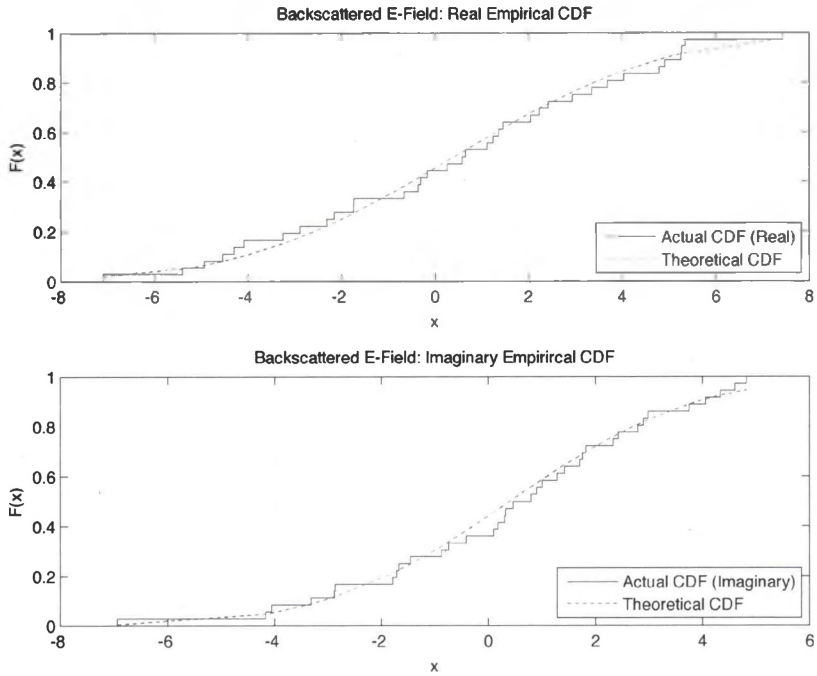

Figure 108: Kolmogorov-Smirnov CDFs

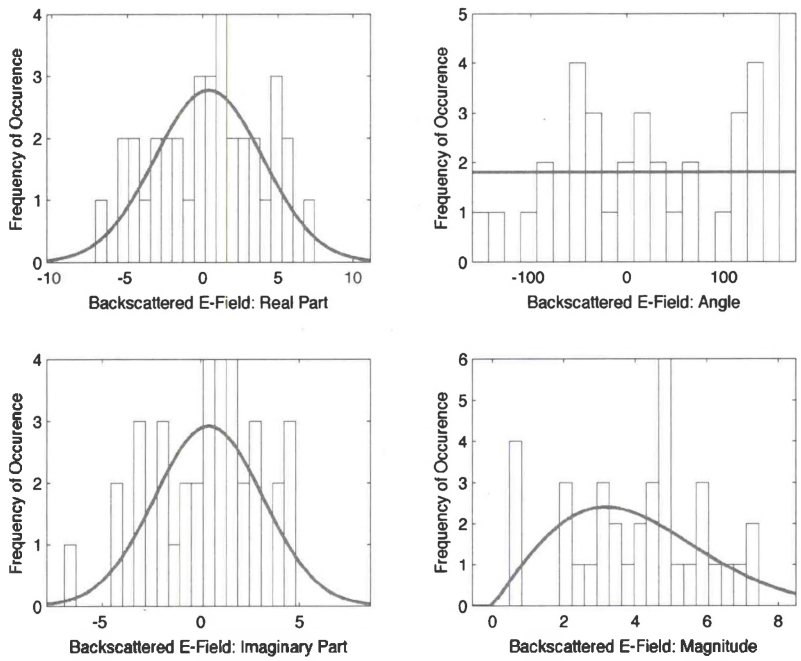

Figure 109: Backscattered E-Field Plots

Appendix 2.F-Range Bin 6

Komolgorov-Smirnov Test Results

Confidence Level =
95.00

Backscattered E-Field: Mean of Real
-0.45

Backscattered E-Field: Standard Deviation of Real
3.82

Backscattered E-Field: Mean of Imaginary
0.45

Backscattered E-Field: Standard Deviation of Imaginary
4.22

Backscattered E-Field: Null Hypothesis for Real
--Accepted--
Observed p-value, P = 0.986903
Observed Kolmogorov-Smirnov Statistic = 0.0735705
The Cutoff Value for determining if the Kolmogorov-Smirnov Statistic is Significant = 0.221211

Backscattered E-Field: Null Hypothesis for Real
--Accepted--
Observed p-value, P = 0.919721
Observed Kolmogorov-Smirnov Statistic = 0.0900976
The Cutoff Value for determining if the Kolmogorov-Smirnov Statistic is Significant = 0.221211

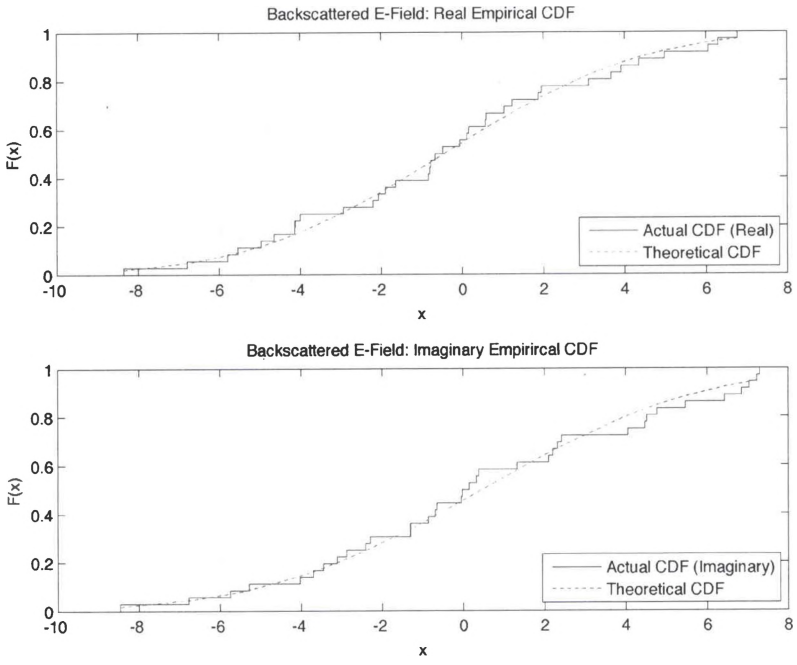

Figure 110: Kolmogorov-Smirnov CDFs

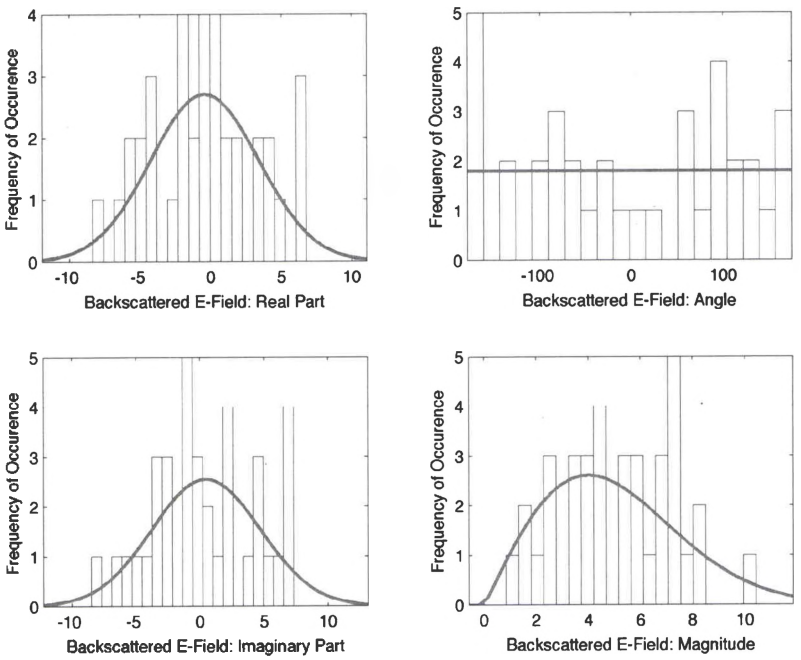

Figure 111: Backscattered E-Field Plots

Appendix 2.G-Range Bin 7

Komolgorov-Smirnov Test Results

Confidence Level =
95.00

Backscattered E-Field: Mean of Real
-0.18

Backscattered E-Field: Standard Deviation of Real
3.29

Backscattered E-Field: Mean of Imaginary
0.02

Backscattered E-Field: Standard Deviation of Imaginary
3.47

Backscattered E-Field: Null Hypothesis for Real
--Accepted--
Observed p-value, P = 0.194385
Observed Kolmogorov-Smirnov Statistic = 0.175843
The Cutoff Value for determining if the Kolmogorov-Smirnov Statistic is Significant = 0.221211

Backscattered E-Field: Null Hypothesis for Real
--Accepted--
Observed p-value, P = 0.836292
Observed Kolmogorov-Smirnov Statistic = 0.101056
The Cutoff Value for determining if the Kolmogorov-Smirnov Statistic is Significant = 0.221211

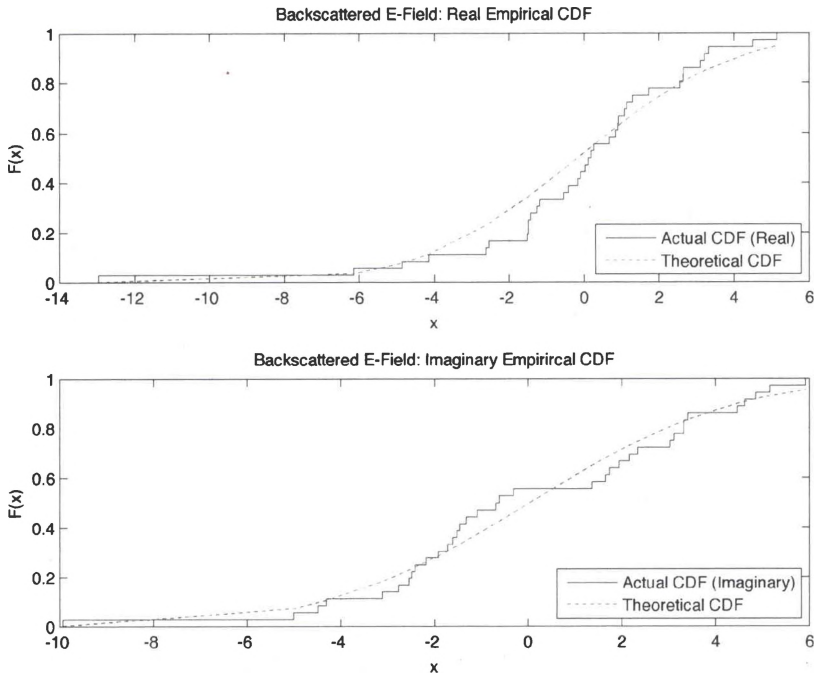

Figure 112: Kolmogorov-Smirnov CDFs

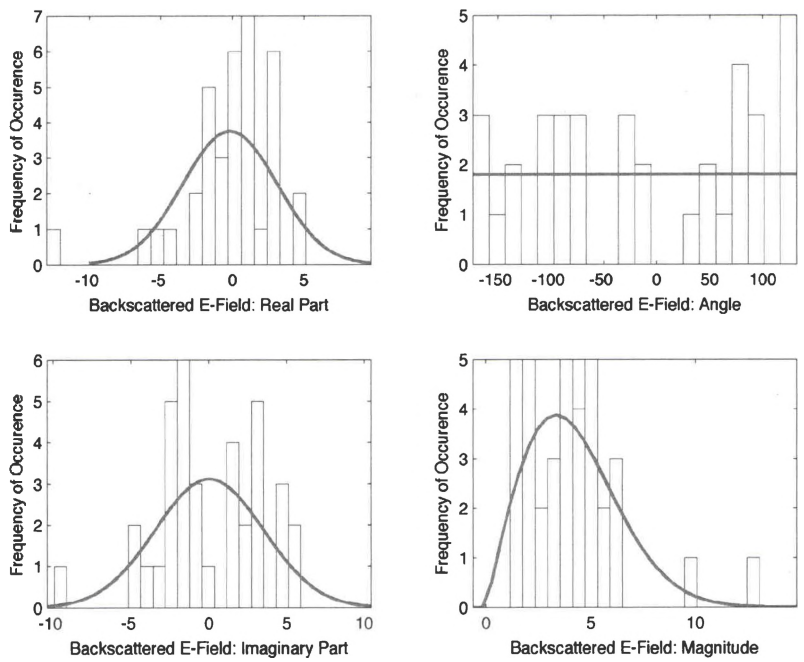

Figure 113: Backscattered E-Field Plots

Appendix 2.H-Range Bin 8

Komolgorov-Smirnov Test Results

Confidence Level =
95.00

Backscattered E-Field: Mean of Real
-0.01

Backscattered E-Field: Standard Deviation of Real
1.82

Backscattered E-Field: Mean of Imaginary
0.09

Backscattered E-Field: Standard Deviation of Imaginary
1.58

Backscattered E-Field: Null Hypothesis for Real
--Accepted--
Observed p-value, P = 0.959256
Observed Kolmogorov-Smirnov Statistic = 0.0826039
The Cutoff Value for determining if the Kolmogorov-Smirnov Statistic is Significant = 0.221211

Backscattered E-Field: Null Hypothesis for Real
--Accepted--
Observed p-value, P = 0.982231
Observed Kolmogorov-Smirnov Statistic = 0.0756857
The Cutoff Value for determining if the Kolmogorov-Smirnov Statistic is Significant = 0.221211

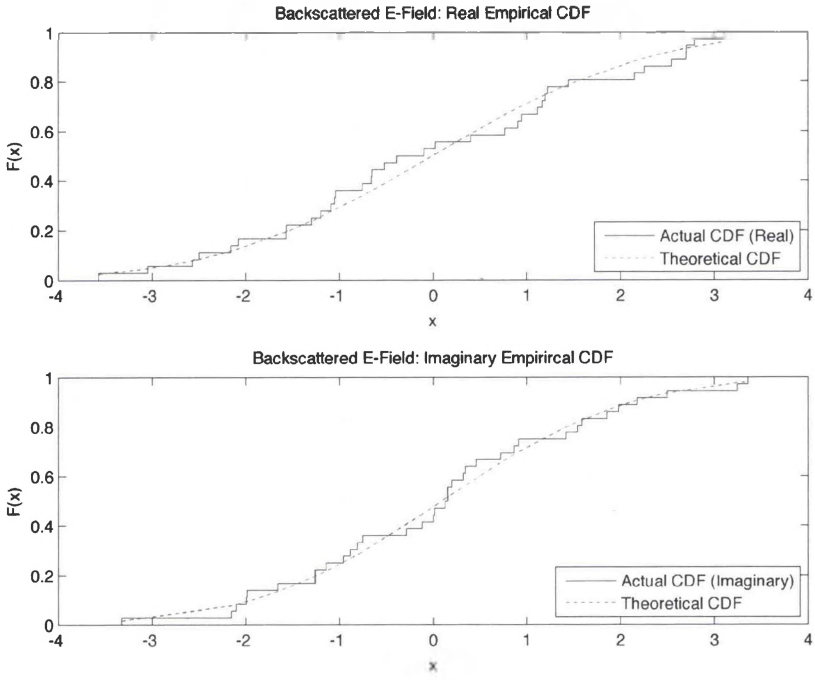

Figure 114: Kolmogorov-Smirnov CDFs

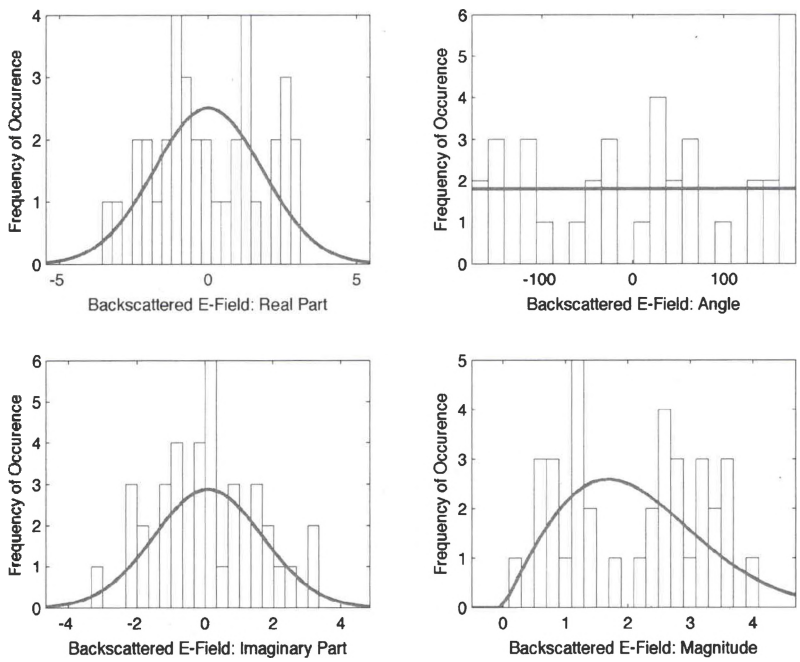

Figure 115: Backscattered E-Field Plots

Appendix 2.I-Range Bin 9

Komolgorov-Smirnov Test Results

Confidence Level =
95.00

Backscattered E-Field: Mean of Real
-0.02

Backscattered E-Field: Standard Deviation of Real
0.60

Backscattered E-Field: Mean of Imaginary
0.02

Backscattered E-Field: Standard Deviation of Imaginary
0.77

Backscattered E-Field: Null Hypothesis for Real
--Accepted--
Observed p-value, P = 0.899164
Observed Kolmogorov-Smirnov Statistic = 0.0931685
The Cutoff Value for determining if the Kolmogorov-Smirnov Statistic is Significant = 0.221211

Backscattered E-Field: Null Hypothesis for Real
--Accepted--
Observed p-value, P = 0.76379
Observed Kolmogorov-Smirnov Statistic = 0.108808
The Cutoff Value for determining if the Kolmogorov-Smirnov Statistic is Significant = 0.221211

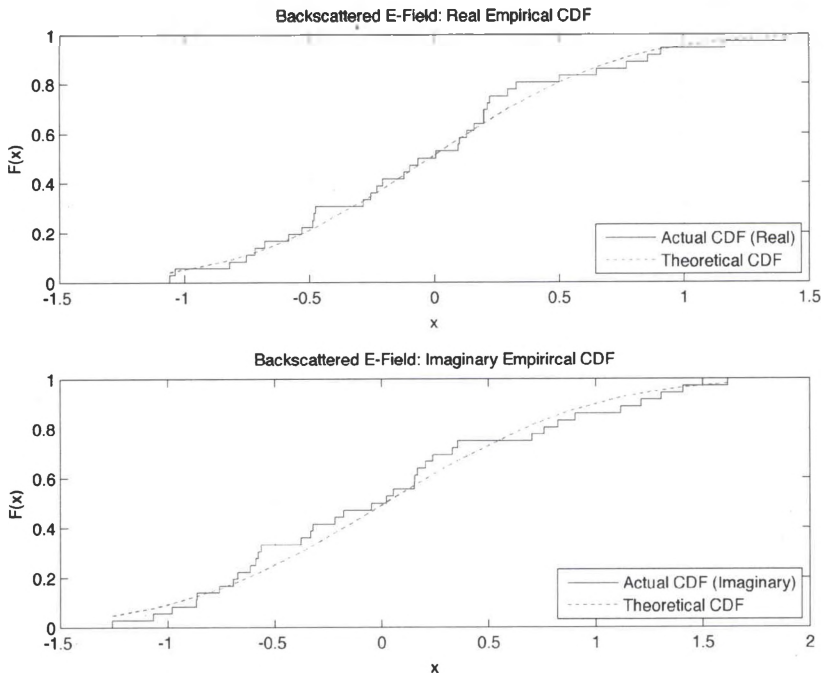

Figure 116: Kolmogorov-Smirnov CDFs

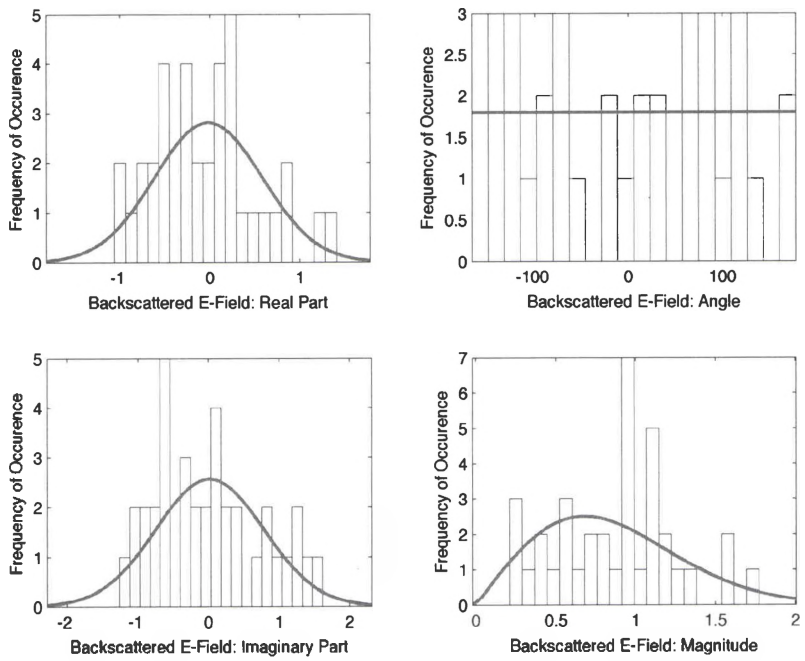

Figure 117: Backscattered E-Field Plots

Appendix 2.J-Range Bin 10

Komolgorov-Smirnov Test Results

Confidence Level =
95.00

Backscattered E-Field: Mean of Real
0.07

Backscattered E-Field: Standard Deviation of Real
0.40

Backscattered E-Field: Mean of Imaginary
0.01

Backscattered E-Field: Standard Deviation of Imaginary
0.49

Backscattered E-Field: Null Hypothesis for Real
--Accepted--
Observed p-value, P = 0.991137
Observed Kolmogorov-Smirnov Statistic = 0.0711182
The Cutoff Value for determining if the Kolmogorov-Smirnov Statistic is Significant = 0.221211

Backscattered E-Field: Null Hypothesis for Real
--Accepted--
Observed p-value, P = 0.787007
Observed Kolmogorov-Smirnov Statistic = 0.106417
The Cutoff Value for determining if the Kolmogorov-Smirnov Statistic is Significant = 0.221211

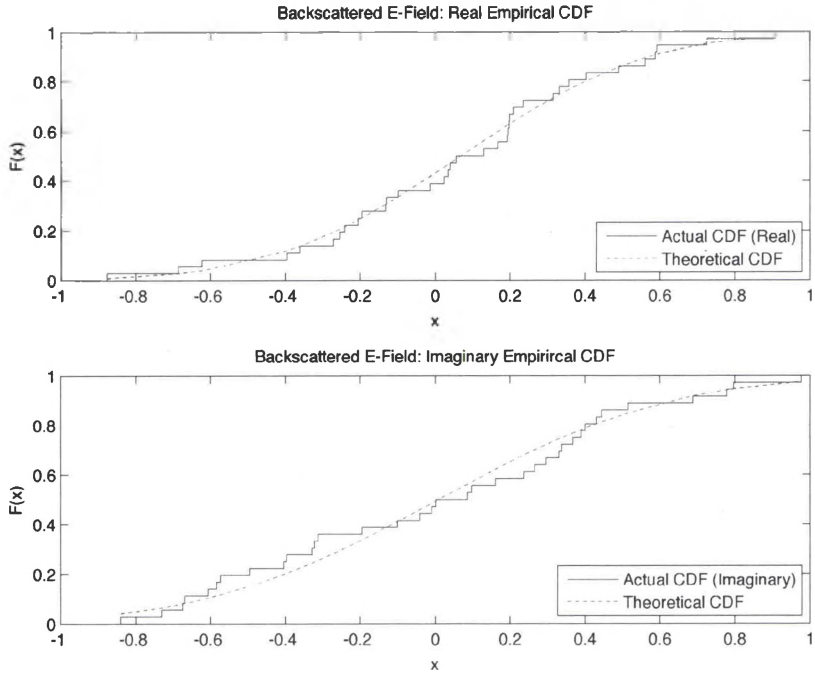

Figure 118: Kolmogorov-Smirnov CDFs

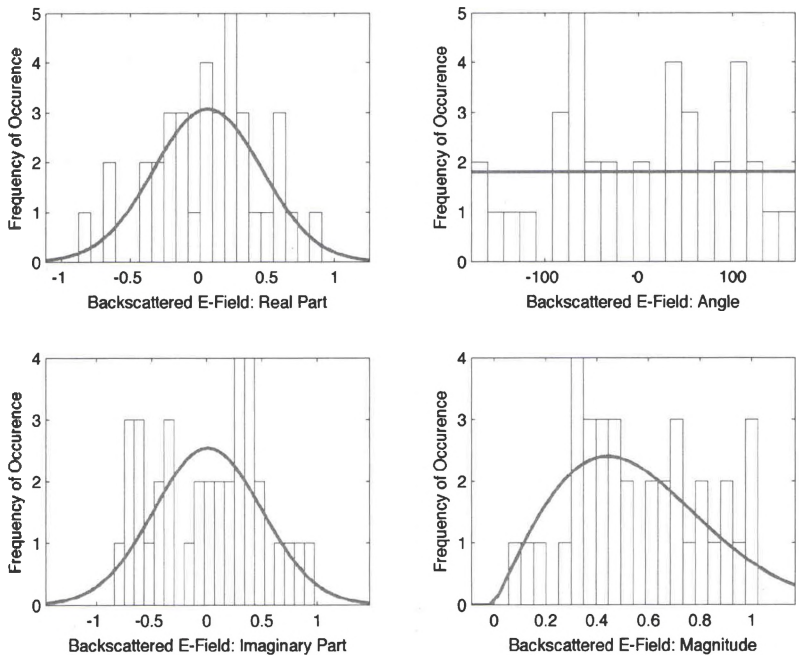

Figure 119: Backscattered E-Field Plots

Appendix 2.K-Range Bin 11

Komolgorov-Smirnov Test Results

Confidence Level =
95.00

Backscattered E-Field: Mean of Real
-0.05

Backscattered E-Field: Standard Deviation of Real
0.35

Backscattered E-Field: Mean of Imaginary
-0.03

Backscattered E-Field: Standard Deviation of Imaginary
0.36

Backscattered E-Field: Null Hypothesis for Real
--Accepted--
Observed p-value, P = 0.93543
Observed Kolmogorov-Smirnov Statistic = 0.0874541
The Cutoff Value for determining if the Kolmogorov-Smirnov Statistic is Significant = 0.221211

Backscattered E-Field: Null Hypothesis for Real
--Accepted--
Observed p-value, P = 0.942176
Observed Kolmogorov-Smirnov Statistic = 0.0862075
The Cutoff Value for determining if the Kolmogorov-Smirnov Statistic is Significant = 0.221211

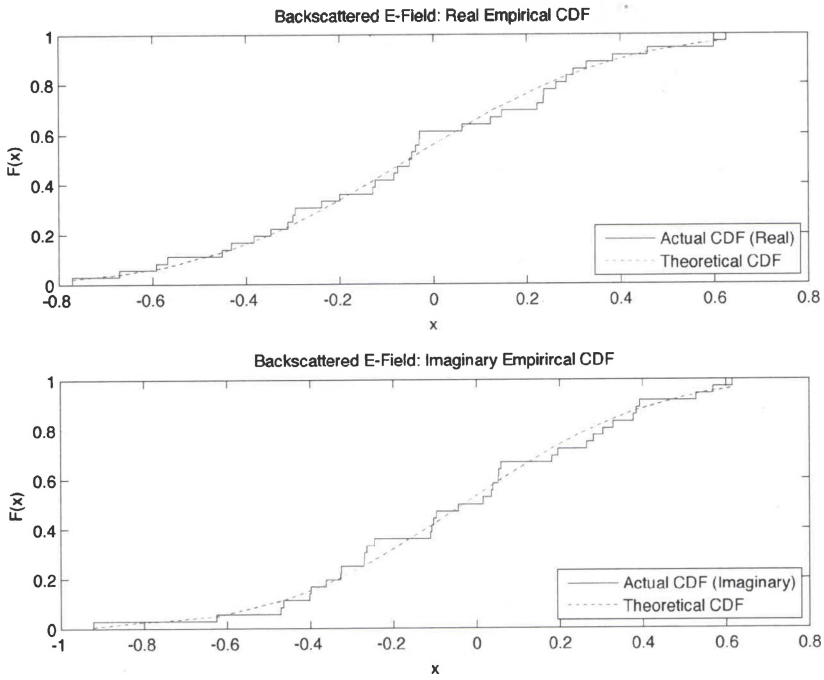

Figure 120: Kolmogorov-Smirnov CDFs

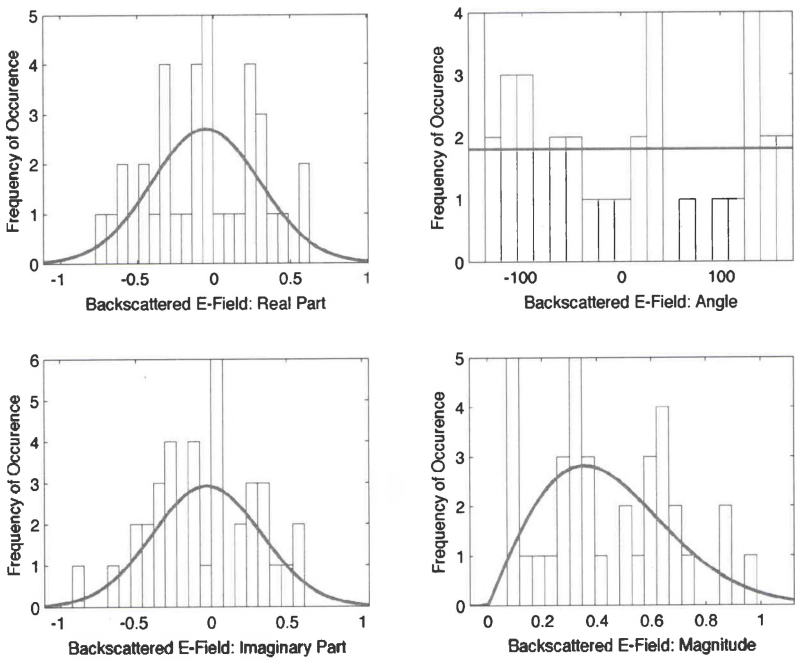

Figure 121: Backscattered E-Field Plots

BIBLIOGRAPHY

[1] Andersh, D., J. Moore, S. Kosanovich., D. Kapp, R. Bhalla, R. Kipp, T. Courtney, A. Nolan, F. German, J. Cook, and J. Hughes, "XPatch 4: The Next Generation in High Frequency Electromagnetic Modeling and Simulation Software," *IEEE International Radar Conference, 2000.* 2000.

[2] Balanis, Constantine, *Antenna Theory: Analysis and Design*, 3rd Ed., John Wiley & Sons, Inc., Hoboken, NJ, 2005.

[3] Bell, Mark R., Information Theory and Radar: Mutual Information and the Design and Analysis of Radar Waveforms and Systems, Ph.D Dissertation, California Institute of Technology, Pasadena, CA, 1988.

[4] Cheng, David K., Field and Wave Electromagnetics, Addison Wesley, Reading, MA, 1983.

[5] Cheung, Julian, William Baldygo, and Yoshikazu Saito, "Optimal Target Identification Based Upon Ultra High Resolution Radar Profiles," *IEEE National Radar Conference*, 1997.

[6] Einstein, A., "Zur Elektrohynamik bewegter Körper," *Annalen der Physik*, vol. 17, pg. 891-921, June 30, 1905.

[7] Goodman, Joseph W., *Introduction to Fourier Optics*, Roberts & Company, Englewood, CO, 2005.

[8] Hovanessian, S.A., *Radar System Design and Analysis*, Artech House, Boston, MA, 1984.

[9] Jacobs, S.P., and J.A. O'Sullivan, "High Range Resolution Radar Models for Joint Tracking and Recognition," *IEEE National Radar Conference*, 1997.

[10] Jacobs, Steven P., and Joseph A. O'Sullivan, "Automatic Target Recognition Using Sequences of High Range Resolution Radar Range-Profiles," *IEEE Transactions on Aerospace and Electronic Systems*, vol. 36, No. 2, Apr., 2000.

[11] Kay, Steven M., *Fundamentals of Statistical Signal Processing: Detection Theory*, Prentice Hall, Upper Saddle River, NJ, 1998.

[12] Long, Maurice W., *Radar Reflectivity of Land and Sea*, 3rd Ed., Artech House, Boston, MA, 2001.

[13] Miller, L.H., "Table of Percentage of Kolmogorov Statistics," *Journal of the American Statistical Association*, March, 1995.

[14] Mitchell, Richard A., and John J. Westerkamp, "Robust Statistical Feature Based Aircraft Identification," *IEEE Transactions on Aerospace and Electronic Systems*, vol. 35, No. 3, July, 1999.

[15] Montgomery, Douglas C., and George C. Runger, *Applied Statistics and Probability for Engineers*, 2nd Ed., John Wiley and Sons, Inc., New York, NY, 1999.

[16] Papoulis, Athanasios, and S. Unnikrishna Pillai, *Probability, Random Variables and Stochastic Processes*, 4th Ed., McGraw Hill, Burr Ridge, IL, 2002.

[17] Press, William H., Brian P. Flannery, Saul A. Teukolsky, and William T. Vetterling, *Numerical Recipes: The Art of Scientific Computing (FORTRAN Version)*, Cambridge University Press, New York, NY, 1989.

[18] Skolnik, Merrill I., *Introduction to Radar Systems*, 3rd Ed., McGraw-Hill, Burr Ridge, IL, 2002.

[19] Soumekh, Mehrdad, *Synthetic Aperture Radar Signal Processing with MATLAB Algorithms*, John Wiley & Sons, Inc., New York, NY, 1999.

[20] Stimson ,*Introduction to Airborne Radar*, 2nd Ed.

[21] Therrien, Charles W., *Discrete Random Signals and Statistical Signal Processing*, Prentice Hall, Englewood Cliffs, NJ, 1992.

[22] Ulug, Batuhan, Stanley C. Ahalt, and Richard A. Mitchell, "Efficient ATR Using Compression," *IEEE Transactions on Aerospace and Electronic Systems,* vol. 33, No. 4, Oct., 1997.

[23] Welsh, Byron, and Robert Hawley, "Physics-Based Signature Modeling," *TRUMPETS Research Note*, July, 1999.

[24] Williams, Rob, John Westerkamp, Dave Gross, and Adrian Palomino, "Automatic Target Recognition of Time Critical Moving Targets Using 1D High Range Resolution (HRR) Radar," *IEEE AES Systems Magazine*, Apr., 2000.